REFERENCE ONLY

UNIVERSITY OF LONDON THESIS

Degree PhD Year 2005 Name of Author GIANNARELLI, C.M.

COPYRIGHT
This is a thesis accepted for a Higher Degree of the University of London. It is an unpublished typescript and the copyright is held by the author. All persons consulting the thesis must read and abide by the Copyright Declaration below.

COPYRIGHT DECLARATION
I recognise that the copyright of the above-described thesis rests with the author and that no quotation from it or information derived from it may be published without the prior written consent of the author.

LOANS
Theses may not be lent to individuals, but the Senate House Library may lend a copy to approved libraries within the United Kingdom, for consultation solely on the premises of those libraries. Application should be made to: Inter-Library Loans, Senate House Library, Senate House, Malet Street, London WC1E 7HU.

REPRODUCTION
University of London theses may not be reproduced without explicit written permission from the Senate House Library. Enquiries should be addressed to the Theses Section of the Library. Regulations concerning reproduction vary according to the date of acceptance of the thesis and are listed below as guidelines.

A. Before 1962. Permission granted only upon the prior written consent of the author. (The Senate House Library will provide addresses where possible).

B. 1962 - 1974. In many cases the author has agreed to permit copying upon completion of a Copyright Declaration.

C. 1975 - 1988. Most theses may be copied upon completion of a Copyright Declaration.

D. 1989 onwards. Most theses may be copied.

This thesis comes within category D.

☑ This copy has been deposited in the Library of UCL

☐ This copy has been deposited in the Senate House Library, Senate House, Malet Street, London WC1E 7HU.

C:\Documents and Settings\lproctor\Local Settings\Temporary Internet Files\OLK8\Copyright - thesis (2).doc

By
kbind
: 3965
tts.co

Properties of the Earth's deep interior studied using *ab initio* modelling techniques

Ché M. S. Gannarelli

2005

Department of Physics and Astronomy

UNIVERSITY COLLEGE LONDON

Thesis submitted for the degree of doctor of philosophy

Supervisors: M.J. Gillan and D. Alfè

ProQuest LLC
789 East Eisenhower Parkway
P.O. Box 1346
Ann Arbor, MI 48106-1346

Abstract

This thesis describes first-principles simulation work undertaken by the author to understand the thermodynamic and elastic properties of iron at the high temperatures and pressures of the Earth's inner core, and how these properties inform our understanding of the inner core, as observed by seismic measurements. In particular, I address the observation that compressional elastic waves travelling parallel to the polar axis traverse the inner core some 3–4% more quickly than waves travelling in the equatorial plane.

The Earth's inner core is a solid ball of iron, alloyed with small amounts of nickel and light elements. The temperature at the boundary with the liquid outer core is approximately 5600 K, and the pressure 330 GPa. The high-pressure, high-temperature phase digram of iron is complex; however it is widely believed that iron has either a bcc or an hcp structure in the core.

Here I focus on hcp iron. I first investigate and repeat a number of previous calculations of the thermodynamics and elasticity of hcp iron made using density functional theory and an approximate particle-in-cell model. It is concluded that the calculations do not correctly describe the high-pressure, high-temperature elasticity of hcp Fe, and that more rigorous calculations are required to gain an understanding of these properties. I then go on to perform *ab initio* molecular-dynamics and harmonic calculations of the temperature dependence of the axial ratio of hcp iron at inner-core pressures, and using this information, perform similar calculations of the elastic constants at inner-core temperatures and pressures. Using these data, I compute compressional wave velocities and their anisotropy in hcp Fe, and draw conclusions about the polycrystalline texturing of the inner core.

Contents

List of Figures

Acknowledgements

This research has been funded by the Natural Environment Research Council, for whose support I am enormously grateful. The calculations were performed using UCL facilities supported by a JREI grant and by SRIF funding, and also using the CSAR facilities in Manchester, funded by the Mineral Physics consortium.

Thanks are due especially to my supervisors, Mike Gillan and Dario Alfè. Mike has provided insight, direction, and also friendship, for which I will always be grateful. To Dario's exceptional knowledge in the realm of electronic structure calculations, and mastery of the VASP code in particular, I owe more than I can express here. Lidunka Vočadlo and David Price also deserve tremendous thanks for many useful conversations, when my pitiful understanding of geology had threatened me with despair.

Andy Gormanly, and Denise Ottley, whose administration on the one hand of the group's computers, and on the other of the group itself, know exactly what I owe them, and are probably keeping a list. It would be unfair here to prejudice that ongoing work. To everybody else at CMMP, you have made my time here a joy. Thank you all.

To my brother, I owe much. He has been a tremendous support, and without his willingness to drive to the country's best climbing areas at the drop of hat, I'd have probably gone crazy long ago.

Finally, to my parents. Without your support I would not be doing this. To you, I owe everything.

List of Publications

Papers

The particle-in-cell model for *ab initio* thermodynamics: implications for the elastic anisotropy of the Earth's inner core.
C. M. S. Gannarelli, D. Alfè and M. J. Gillan
Physics of the Earth and Planetary Interiors, **139**: 243 (2003).

The axial ratio of hcp iron at the conditions of the Earth's inner core.
C. M. S. Gannarelli, D. Alfè and M. J. Gillan
Physics of the Earth and Planetary Interiors, **152**: 67 (2005).

(We expect also to submit my work on elastic constants to PEPI.)

Conference talks

Invited talks

ECM22 2004, Budapest
"Axial ratio and elastic constants of hcp Fe under Earth's core conditions"
C. M. S. Gannarelli, D. Alfè and M. J. Gillan
Abstract: *Acta Crystallographica*, A**60**: s48 (2004).

Contributed talks

CMD19CMMP 2002, EPS/IOP Conference, Brighton

"*Ab initio* thermodynamics of iron at Earth's core conditions by the 'particle-in-cell' approximation."

C. M. S. Gannarelli, D. Alfè and M. J. Gillan

Abstract: *Europhysics Conference Abstracts*, **26A**:, C24.7.3 (2002).

EGS/AGU/EUG Joint Assembly 2003, Nice

"Elastic anisotropy in the Earth's inner core — an appraisal of *ab initio* calculations."

C. M. S. Gannarelli, D. Alfè and M. J. Gillan

Abstract: *Geophysical Research Abstracts*, **5**: 02632 (2003).

Chapter 1

In Sneffels Joculis craterem
quem delibat / Umbra Scartaris
Julii intra calendas descende, /
Audax viator, et terrestre
centrum attinges.

Jules Verne (1828–1905)

Introduction

The inner core of the Earth is known ([1] and elsewhere) to exhibit seismic anisotropy. That is, it is observed that compressional elastic waves emitted by earthquakes in the Earth's crust traverse the inner core some 3–4% faster along the Earth's rotational axis, than in the equatorial plane. There is presently no clear explanation of this phenomenon; however an understanding of the elasticity of the materials of the inner core is clearly essential to developing such an explanation.

This thesis presents theoretical work undertaken by the author to study the materials properties of the Earth's inner core using a variety of *ab initio* simulation methods, and particularly the high-pressure, high-temperature elastic constants of hexagonal close packed (hcp) iron. I then go on to discuss the geophysical implications my findings. This introduction sets out some of the history of materials simulation, then goes on to discuss some properties of the structure of the Earth's interior, and the computational difficulties inherent in simulating its materials.

1.1 The simulation of materials properties

One of the great successes of twentieth century physics is the development of a wide range of material simulation techniques, which have combined with the ever-increasing power and availability of computational resources to provide important new insights into the properties of materials. From classical atomistic simulation in the harmonic limit [2], through anharmonic cell-models [3] and classical molecular dynamics [4], to the powerful quantum-mechanical simulation techniques of today [5, 6], computational simulation has vastly increased our understanding of materials science.

1.1.1 Molecular dynamics

Molecular dynamics simulation in particular has a long and distinguished history, faithfully reproducing the materials properties of many systems at high temperatures. However, due to the large number of force calculations necessary to compute even a short molecular dynamics trajectory, this technique was long restricted to calculations involving fitted empirical potentials, and the idea of computing forces by on-the-fly *ab initio* electronic structure calculations was considered impractical.

One important challenge in using empirical interatomic potentials is the availability of data for fitting the potentials. If one wishes to perform calculations on a material at temperatures and pressures well outside of the experimentally accessible range, there can be no assurance that potentials constructed on such experiments will be valid. This problem is exacerbated in the case of a metal, where the thermal excitation of electrons may well have a non-negligible effect on properties of interest.

1.1.2 Electronic structure calculations

The efficient calculation of the electronic structure of many-body systems is a long-standing problem in physics, and one which remains generally unsolved. However there do exist a host of approximate methods which have enjoyed success for a wide range systems, one of the most efficient of which is density functional theory [5, 7, 8, 9]. Density functional theory provides a means of calculating the ground-state energy of an interacting electron gas, by expressing the energy as a functional of the charge density, which will be minimized in the ground state. This method requires certain approximations to the form of this functional, as is discussed in detail in Ch. 2. DFT will also allow one to determine the forces on classical ions in an electron-ion system, and therefore to perform *ab initio* molecular dynamics simulations.

Density functional theory has undergone many developments since its introduction, which have been of great importance in widening the range of applicability of the technique. The most important of these for this work are the finite temperature extension [10] of Mermin, the generalized gradient approximation (GGA) [11, 12, 13] to the exchange-correlation potential, and the projector augmented wave (PAW) [14] implementation due to Blöchl. All of these will be discussed in Ch. 2, when I introduce the density functional formalism itself.

These techniques can be extremely expensive, particularly for the large simulation cells used in molecular dynamics, and for a very great time, electronic structure methods in solid-state physics were limited to the calculation of the properties of static regular lattices, and later to harmonic calculations. The first molecular dynamics simulations to use DFT-based electronic structure calculations to compute interatomic forces were due to Car and Parrinello [15], who employed a common timestep to evolve both the electronic basis-state coefficients (given a fictitious mass) and the ionic coordinates. In this work, I do not employ this particular technique; how-

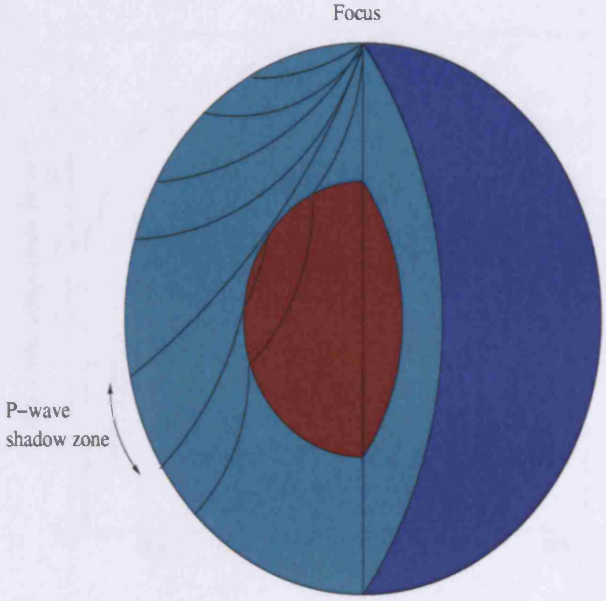

Figure 1.1: The inner structure of the Earth, showing seismic P-wave trajectories.

ever it should be stated that all *ab initio* molecular dynamics owes much to the work of Car and Parrinello.

1.2 The Earth's interior

1.2.1 Seismological investigation

The Earth is a slightly oblate spheroid, with a minor axis radius of 6357 km from pole to pole, a major axis radius of 6378 km across the equator, and has a mass of 5.976×10^{24} kg [16]. The last value may be deduced from the orbit of satellites. A great deal of information about the Earth's interior is available from the study of seismic phenomena: that is, the behaviour of elastic waves generated by earthquakes. Fig. 1.1 shows what happens when an earthquake occurs in Mongolia. Transverse, or S-waves and compressional, or P-waves travel through the Earth's interior — these waves

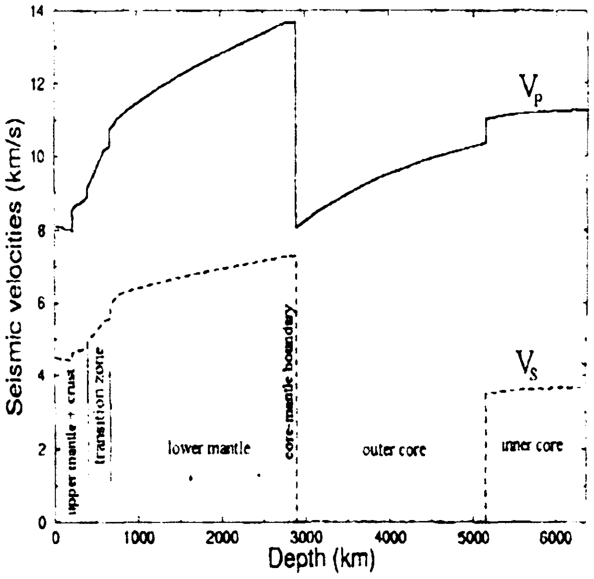

Figure 1.2: S- and P-wave velocities as a function of depth, from [17].

are collectively know as *body waves* — and so-called *surface waves* travel over the surface of the Earth in the crust layer. The travel times of these waves to various detector stations (i.e. that shown in Cairo) can then be measured. This leads directly to a wave-velocity vs. depth profile for the Earth, as shown for S- and P-waves in Fig. 1.2. It is on the basis of the discontinuities in body-wave velocities that the Earth is divided into the layers of crust, mantle, outer core and inner core indicated in Fig. 1.1. The only observation I make at this point is that v_S vanishes completely in the outer core, indicating that the outer core is liquid.

Seismic wave velocities only provide a partial picture of the physics of the Earth's interior. To stand any chance of discovering the materials present, and their properties we need to know much more. The density-depth profile of the Earth is in important piece of information. With it, we can compute the adiabatic bulk and shear moduli in the core, and Poisson's ratio, and stand a much greater chance of determining the properties of deep-Earth

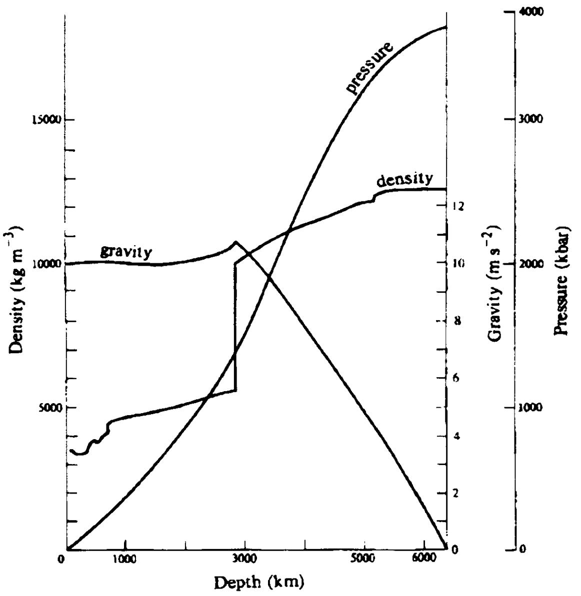

Figure 1.3: The density of the Earth as a function of depth, from [17].

materials.

Deducing the density-depth profile of the Earth is a very complex problem. Certainly body-waves velocities alone do not meaningfully constrain the problem. We do, however, have other information, such as the total mass of the Earth. We also know the Earth's moment of inertia [17]. Because the Earth has a somewhat flattened shape, the gravitational pulls of the Sun and Moon cause a torque on the Earth about an axis lying in the equatorial plane. This results in a precession of the axis of the Earth, from which the moment of inertia can be computed [18]. The moment of inertia of the Earth about its rotational axis is found to be 8.07×10^{37} kg m^2, whereas for a spheroid of the dimensions of the Earth, having uniform density, the expected moment of inertia would be 9.7×10^{37} kg m^2. This indicates a concentration of mass near the centre of the Earth, suggesting that the core may be much more dense than the surrounding mantle.

Another piece of information, which helps to constrain the possible density profile of the Earth, is free-oscillation data. Any earthquake will cause the Earth, like any body, to oscillate at various natural frequencies. The modes of oscillation of a spheroid are complex, and some are given in Brown & Mussett [17]. Employing this wide variety of data, Press [19, 20] used the method of Monte Carlo inversion to test large sets of randomly generated Earth models. This work gave rise to the constrained profile given in Fig. 1.3 (for a more detailed introduction to these ideas see also [17]). As is observed, both the inner and the outer core show a density far in excess of the mantle.

The density gives directly the pressure in the Earth due to gravity, and in conjunction with with body-wave velocities, it is easy to compute the bulk (adiabatic) K and shear μ elastic moduli, and hence Poisson's ratio ν as a function of depth, using the formulae

$$K = \rho v_P^2 , \qquad \mu = \rho v_S^2 , \tag{1.1}$$

$$\nu = \frac{3K - 2\mu}{2(3K + \mu)} . \tag{1.2}$$

Collectively, these data, comprising the body wave velocities, density, Poisson's ratio, and many other properties of the Earth's interior, constitute the so-called *preliminary Earth reference model* (PREM) [21]. Within this model, Poisson's ratio is found to have a constant value within the inner core of 0.44 — much higher than that of the mantle (Fig. 1.4).

1.2.2 Composition

Can one now identify the material or materials in the inner core? We know that there is a material of very high density in the core. Furthermore, it is universally accepted that the Earth's magnetic field is due to electrical currents in the liquid outer core. The inner core therefore must contain a high proportion of a heavy metal.

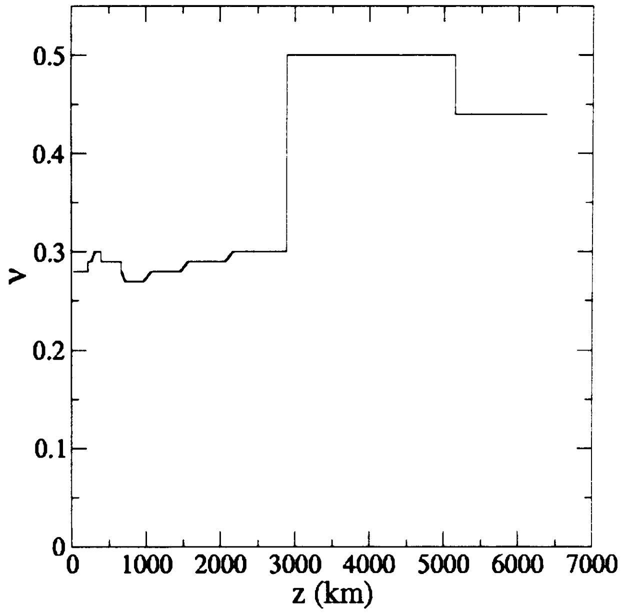

Figure 1.4: Poisson's ratio ν as a function of depth z in PREM [21].

Models of element abundance in the solar system show that iron is by far the most abundant very dense metallic element. Furthermore, the Chondritic Earth Model suggests that the Earth should have a composition similar to chondritic meteorites, which contain approximately 32% O, 25% Fe, 14.5% Si, 12.5% Mg, 8% S and 8% of other trace elements. A detailed discussion of the condritic Earth model lies outside of the scope of this work, and the interested reader is directed to that of [17], Ch. 5. However, by considering the chemistry of these various elements, and the role of gravity in the segregation of materials, it is believed that the composition of the core of the Earth is broadly understood. Furthermore, the first principles calculation of the chemical potentials of light elements dissolved in liquid and solid Fe place still tighter constraints on the possible composition of the inner core [22, 23].

The outer core of the Earth is a liquid alloy of Fe with various light elements, below which is the solid inner core. The inner core grows at the expense of the outer, as the iron cools and freezes. The resultant latent heat of fusion is, along with the radioactive decay of ^{40}K, one of the main sources of heat from the core, responsible for driving convection process, both in the liquid outer core, affecting the Earth's magnetic field, and in the mantle, driving the processes of plate tectonics.

The inner core is a solid sphere of Fe alloy, of density 12 600–13 000 kg m^{-3} at a pressure of around 3.3 Mbar (see Fig. 1.3). Shock-wave experiments at this pressure, however, indicate that this density is too low, and that the Fe is therefore alloyed with some unknown light impurities. The iron in the inner core, has an unknown crystalline structure; one of the principle candidates is hcp.

Finally, what do is known of the temperature of the Earth's core? The inner-core boundary is a phase boundary between alloys of solid and liquid Fe. Therefore the temperature of the core will be at the melting point of the Fe alloy at a pressure of 3.3 Mbar.

1.3 Experimental studies of core materials

Understanding the properties of the deep interior — and the core in particular — is one of the great challenges for geology. There are no samples of core material on the Earth's surface, and even if there were, these would not be in the crystalline phase of the inner core. Beyond the predominance of Fe, and the presence of some light impurities, even the composition of the core has not been accessible to experimental investigation.

Further, experiments performed using diamond anvil cells (DAC [24]) and large-volume multi-anvil presses [25] to create extreme pressures in materials, while able to produce pressures approaching those of the inner core, cannot access simultaneously the great temperatures necessary to melt iron at these pressures. Thus, while these experiments give us much of our understanding of the high-pressure melting curve of Fe [26], they cannot provide this information for the very highest pressures at the inner-core boundary, and so are not able to answer the very fundamental question of the temperature of the core.

Shock-wave experiments [27] have now produced much higher pressures and temperatures on the *Hugoniot* shock equation of state, but present a formidable technical challenge, producing as they do only fleeting high pressures. These have been used to produce points on the high-pressure melting curve (i.e. [28]), but only at the intersection points of the Hugoniot $T-p$ and $p-V$ curves with the melting curve. Additionally, interpreting the temperature in such experiments creates significant challenges itself.

1.4 Simulation of core materials

There is clearly an enormous range of unanswered questions about Earth's core materials: what light elements are present? what is the crystalline phase in the inner core? what is the source of inner core anisotropy? what is the temperature of the inner core. Given these questions, and the extraordinarily challenging nature of experimental investigation, it is clear that there is a significant rôle for simulation in studying the Earth's interior; however the very fact that so little information exists about the properties of inner-core materials, means that the data necessary to fit parameterized empirical potentials does not exist. We therefore turn instead to *ab initio* quantum mechanical simulation.

The earliest such calculations were performed at zero temperature, since the expense of molecular-dynamics calculations was so great. Stixrude *et al.* computed the zero-temperature, high-pressure equation of state of hcp, fcc and bcc Fe [29], and later the zero temperature elastic constants of the fcc and hcp phases. They found that for hcp Fe at 13 Mg $m^{-3}$the elastic constant c_{33} was approximately 3% greater than c_{11}. Thus the seismic anisotropy of the core could be explained if it was composed of hcp crystallites with hexagonal (c) axes totally aligned with the Earth's rotational axis.

Important high-temperature *ab initio* molecular dynamics calculations due to Vočadlo, Alfè and others *et al.* [30, 31, 23, 32, 33, 34] on both liquid and hcp solid Fe provided a wealth of new geophysical information. By calculating the melting curve of Fe [31], Alfè *et al.* were able to estimate the temperature of the inner core boundary. By using thermodynamic integration to compute chemical potentials of various light elements in solution in both solid and liquid iron [23], and equating these across the phase boundary, they placed constraints on the composition of the core, demonstrating in particular that the long-standing hypothesis that the outer core is a very nearly binary Fe-S mixture is incompatible with the low degree of partitioning of S between solid and liquid Fe.

Using the *particle in cell* (PIC) approximation, Steinle-Neumann *et al.* [35] computed the high-temperature elastic constants and axial ratio c/a of hcp Fe (Figs. 1.5 and 1.6). Their results indicated a startling rise in c/a with volume, causing a softening of the c_{33} elastic constant, and a corresponding increase in the c_{11} elastic constant, to the extent that the anisotropy of the inner core could only be explained by a model in which the crystalline c axes lay in the equatorial plane. However, the use of the PIC approximation in this work resulted in some doubt over the accuracy of these results.

1.5 This work

This thesis describes *ab initio* simulation work undertaken by the author to model the elastic properties of hcp Fe at the temperatures and pressures of the inner core. The work falls into three major sections. In Ch. 5 I describe calculations undertaken to test the usefulness of the PIC model. Here I calculate many thermodynamic quantities for hcp Fe, and compare them

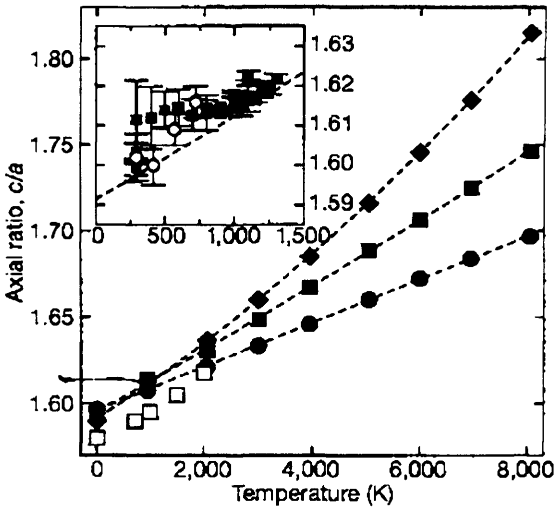

Figure 1.5: PIC calculations of c/a by [35] at 12.52 Mg m^{-3} (filled diamonds), 13.04 Mg m^{-3} (filled squares) and 13.62 Mg m^{-3} (filled circles).

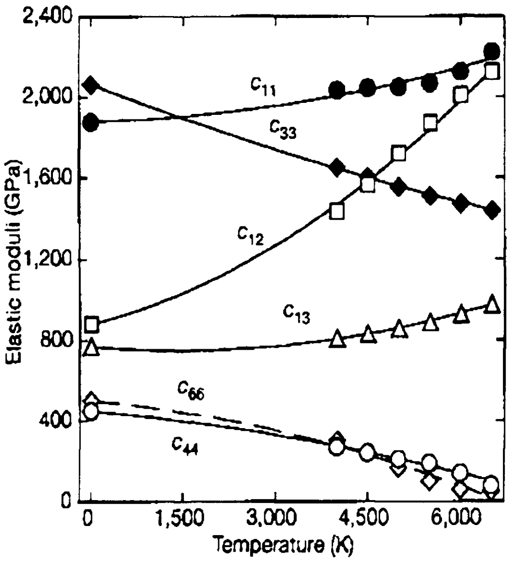

Figure 1.6: PIC calculations of elastic constants by [35] at 13.04 Mg m^{-3}.

with the the earlier PIC results of [35, 36, 37], and with the fully-correlated anharmonic results of [34], so obtain an objective measure of errors incurred by the PIC model. In Ch. 6 I use *ab initio* molecular dynamics and harmonic theory to compute the axial ratio of hcp Fe without making the PIC approximation. It is noted that the strong temperature dependence of [35] is not observed. Finally, in Ch. 7, we calculate the high-temperature elastic constants of Fe, again using both *ab initio* molecular dynamics and harmonic theory. I find no evidence for the Steinle-Neumann *et al.* reinterpretation of the anisotropy.

The other remaining chapters are as follows. In Ch. 2, I set out the theory behind the *ab initio* electronic structure techniques I employ. Ch. 3 discusses statistical mechanical methods used in calculating thermodynamic properties. In Ch. 4 I discuss the theory of elasticity under pressure.

Discussion and conclusions will be given in Ch. 8.

Quis me locus, quae regio, quae
mundi plaga?

Lucius Annaeus Seneca
(3 BC–AD 65)

Chapter 2

Ab initio electronic structure methods

It is my objective is to study the thermodynamic properties of materials as derived using statistical mechanical methods. These methods can be used to go from the *ab initio* Helmholtz free energy $U(\{\mathbf{R}_i\};\{\lambda_j\},T_{\mathrm{el}})$ of the static electron-ion system (the configurational energy), to the free energy F of the vibrating lattice. In the above, the $\mathbf{R}_i$ are the position vectors of all the ions, $\{\lambda_j\}$ is a set of external constraints including atomic volume and strain tensor components. T_{el} is the temperature of the electronic subsystem, which has a physical significance very much dependent on the *ab initio* techniques employed. As I will be treating systems over a very wide temperature range, the thermal excitation of electrons will be of great importance, which requires, as we shall discover, a finite temperature calculation in terms of U.

In this chapter, I introduce the methods used to obtain the configurational energy U. In Ch. 3 I go on to discuss various statistical mechanical approaches to obtaining F, the total free energy of the lattice.

Ab initio electronic structure techniques seek to describe the behaviour of a system of interacting electrons in an external potential $v(\mathbf{r})$, such as that due to the presence of atomic nuclei, or ionic cores. Of course the most direct approach to this problem is the solution of the many-body time-independent Schrödinger equation

$$\hat{H}\Psi = E\Psi \tag{2.1}$$

where $\hat{H}$ is the Hamiltonian operator, Ψ is the many-body wave function and E is the energy of the system.

An exact solution of equation 2.1 is not, in general, possible and whilst perturbative techniques exist, which provide a systematic method of approximating the many-body wave function Ψ, these are exceedingly difficult computational and intellectual problems. For the performance of such extensive calculations as will be necessary for the statistical mechanical treatment of material properties, these methods demand simplification; we will see that *density functional theory* (DFT) provides just such a practical simplification. I begin by introducing the Born-Oppenheimer approximation, which underlies all electronic structure techniques and proceed pedagogically to a description of Kohn-Sham density functional theory. For those theoretical methods I discuss in detail, only a basic grounding in quantum mechanics will be assumed.

2.1 The Born-Oppenheimer approximation

The most general approach to the properties of a system of electrons and nuclei of atomic number Z, is to treat the entire system as quantum mechanical and to seek a solution for the wave function Ψ of the entire system of the many-body Schrödinger equation

$$\left(-\frac{1}{2}\sum_i \nabla^2_{\mathrm{el}_i} - \frac{1}{2}\sum_j \nabla^2_{\mathrm{N}_j} + \sum_{i<i'} \frac{1}{r_{ii'}} + \sum_{j<j'} \frac{Z^2}{R_{jj'}} - \sum_{i,j} \frac{Z}{|\mathbf{r}_i - \mathbf{R}_j|} \right) \times \Psi(\{\mathbf{x}_i\}, \{\mathbf{X}_i\}) = E\Psi(\{\mathbf{x}_i\}, \{\mathbf{X}_i\}) \tag{2.2}$$

for the coupled system of electrons and nuclei, where $r_{ii'} = |\mathbf{r}_i - \mathbf{r}'_i|$, $R_{jj'} = \left|\mathbf{R}_j - \mathbf{R}'_j\right|$ and I have used $\hbar = 4\pi\varepsilon_0 = e = m_\mathrm{e} = 1$; $\mathbf{r}$ and $\mathbf{R}$ represent electronic and nuclear coordinates respectively, and $\mathbf{x}$ and $\mathbf{X}$ correspondingly represent their joint spin and spatial coordinates. To understand why this approach can be avoided, we observe that the great difference in mass between electrons and nuclei will lead to the electrons moving several orders of magnitude more rapidly than the nuclei. Thus, one can approach the problem by first factoring the wave function $\Psi(\{\mathbf{r}_i\}, \{\mathbf{R}_i\})$ of the system into a nuclear part $\Psi_\mathrm{N}(\{\mathbf{R}_i\})$ and an electronic part $\Psi_\mathrm{el}(\{\mathbf{r}_i\}; \{\mathbf{R}_i\})$, depending only parametrically on the nuclear coordinates $\{\mathbf{R}_i\}$. Then the electronic wave function is solved for a static external potential corresponding to the position of the nuclei, and conversely, the nuclear wave function can be solved by assuming that the electronic wave function changes adiabatically with the positions of the nuclei, always in its equilibrium thermodynamic state or, at zero temperature, its ground state. For all but a very few cases (see, for example reference [38]), the nuclear subsystem may now be treated classically and the stationary states of the electronic subsystem are given by

$$\hat{H}_\mathrm{el}\Psi_\mathrm{el} = \left(-\frac{1}{2}\sum_i \nabla_i^2 + \sum_{i<i'} \frac{1}{r_{ii'}} - \sum_{i,j} \frac{Z}{|\mathbf{r}_i - \mathbf{R}_j|} \right) \Psi_\mathrm{el} = E_\mathrm{el}\Psi_\mathrm{el} \, . \tag{2.3}$$

2.2 The variational principle in quantum mechanics

Our task now, is to consider how, given a particular time-independent Hamiltonian $\hat{H}$, we can find the corresponding ground state. The variational principle allows us to place an upper bound on the ground-state energy, and is the common starting point for all attempts to systematically approximate the ground state. It should noted, however, that the variational principle is not limited to finding the ground state of a system, as will be explained later.

According to the principle of superposition, the eigenstates $|\phi_i\rangle$ of $\hat{H}$ form a complete set such that any trial state $|\Phi\rangle$ may be expressed as the sum

$$|\Phi\rangle = \sum_i c_i \, |\phi_i\rangle \tag{2.4}$$

where the $c_i = \langle\phi_i|\Phi\rangle$ are a set of complex coefficients. The expectation value of the energy in such a state is then

$$\begin{aligned} \langle\Phi|\hat{H}|\Phi\rangle &= \sum_{i,i'} c_i^* c_{i'} \, \langle\phi_i|\hat{H}|\phi_{i'}\rangle \\ &= \sum_i |c_i^*|^2 E_n \\ &\geq E_0 \end{aligned} \tag{2.5}$$

since $E_0 \leq E_i$ for all i. Thus, for a parameterized trial wave function, the best approximation to the ground state is obtained for those values of parameters that minimize E_0. A host of techniques exist to set up efficient trial wavefunctions, that can be systematic improved. The specific techniques used in this work will be developed throughout the remainder of this chapter.

2.3 Thomas-Fermi density functional theory

The many-body wave function $\Psi(\mathbf{x}_1, \mathbf{x}_2, \ldots \mathbf{x}_N)$ is an extremely complicated $3N$ dimensional function; however it may be expressed in terms of a set of one-particle spin orbitals $\chi_i(\mathbf{x})$. Each of these may be in turn expressed in a one-particle basis set, to facilitate computational treatment. Since the wavefunction is known to be antisymmetric under particle exchange, its representation in terms of combinations of the χ_i must ensure this. The simplest such combination is the Slater determinant,

$$\Psi(\mathbf{x}_1, \mathbf{x}_2, \ldots \mathbf{x}_N) = \frac{1}{\sqrt{N}} \begin{vmatrix} \chi_1(\mathbf{x}_1) & \chi_1(\mathbf{x}_2) & \cdots \\ \chi_2(\mathbf{x}_1) & \chi_2(\mathbf{x}_2) & \cdots \\ \vdots & \vdots & \ddots \end{vmatrix} . \tag{2.6}$$

The familiar Hartree-Fock theory employs a single Slater determinant, as above, for the many body wavefunction. This yields a theory which completely neglects correlations between electrons. A more general wavefunction consists of many such determinants, and can be used to include correlation effects; however such methods scale poorly with electron number, and are not well-suited for periodic systems of many electrons.

Clearly, therefore, it is desirable to seek a simplified approach. One idea, first developed by Thomas and Fermi [39, 40, 41, 42, 43] was to work in terms of the electron density

$$n(\mathbf{r}) = N \sum_{S_1 \dots S_N} \int \mathrm{d}\mathbf{r}_2 \dots d\mathbf{x}_N \Psi(\mathbf{x}, \mathbf{x}_2, \dots \mathbf{x}_N) \Psi^*(\mathbf{x}, \mathbf{x}_2, \dots \mathbf{x}_N) \,. \tag{2.7}$$

The clear advantage of the number density as a basic variable is that it is a function of only three spatial degrees of freedom. The method proceeds by the expression of total energy as a functional $E[n(\mathbf{r})]$, and minimising this energy over densities $n(\mathbf{r})$. In the formulation of Thomas-Fermi, the total energy functional takes the form

$$E[n(\mathbf{r})] = T[n(\mathbf{r})] + \int \mathrm{d}\mathbf{r} v(\mathbf{r}) n(\mathbf{r}) + \frac{1}{2} \int \mathrm{d}\mathbf{r} \mathrm{d}\mathbf{r}' \frac{n(\mathbf{r}) n(\mathbf{r}')}{|\mathbf{r} - \mathbf{r}'|} \,, \tag{2.8}$$

where $v(\mathbf{r})$ is the ionic potential. The kinetic energy functional is given by

$$T[n(\mathbf{r})] = \frac{3}{10} (3\pi^2)^{2/3} \int \mathrm{d}\mathbf{r} n^{5/3}(\mathbf{r}) \,. \tag{2.9}$$

This expression arises from considering the kinetic energy of a set of ΔN non-interacting electrons in an infinite potential well of volume ΔV at $\mathbf{r}$. Eq. (2.9) arises from taking the limit $\Delta V \rightarrow 0$ such that $\Delta N / \Delta V = n(\mathbf{r})$, and integrating over all space.

2.4 The Hohenberg-Kohn theorems

The use of the electron density as a basic variable was not placed on a sound formal basis until the development two theorems of Hohenberg and Kohn

[7]. A practical method of reducing the problem to a one-particle system was later developed by Kohn and Sham [8], and this provides the basis of modern [5, 9] DFT.

The formal development of density functional theory rests on two theorems of Hohenberg and Kohn [7]. The first shows that there is a one-to-one correspondence between external potential and ground-state number density. These theorems are expressed in reference to a Hamiltonian of the form

$$\hat{H} = -\frac{1}{2}\sum_i \nabla_i^2 + \sum_{i<i'} \frac{1}{r_{ii'}} + v(\mathbf{r}) \tag{2.10}$$

where $v(\mathbf{r})$ is an external potential due, for instance, to the presence of an ionic lattice.

Proposition (Hohenberg-Kohn theorem I). *Within a trivial additive constant there is a one-to-one relationship between the external potential* $v(\mathbf{r})$ *and the ground-state number density* $n(\mathbf{r})$.

Proof. Take $n(\mathbf{r})$ to be the ground-state number density under $v(\mathbf{r})$ and $v'(\mathbf{r})$, two external potential differing by more than a constant. These potentials will yield two different Hamiltonians $\hat{H}$ and $\hat{H}'$, with the same ground-state number density $n(\mathbf{r})$, but corresponding to the different ground-state wave functions, respectively Ψ and Ψ'.

Because of the variational principle, if we take Ψ' to be a trial function for $\hat{H}$ and evaluate the expectation value

$$\begin{aligned}\langle\Psi'|\hat{H}|\Psi'\rangle &= \langle\Psi'|\hat{H}'|\Psi'\rangle + \langle\Psi'|\hat{H} - \hat{H}'|\Psi'\rangle \\ &= E_0' + \int n(\mathbf{r})\left[v(\mathbf{r}) - v'(\mathbf{r})\right] \mathrm{d}\mathbf{r} \\ &< E_0\end{aligned} \tag{2.11}$$

where E_0 and E_0' are the ground-state energies corresponding to $\hat{H}$ and $\hat{H}'$

respectively. Similarly, taking Ψ to be a trial function for $\hat{H}'$, we have

$$\begin{aligned}\langle\Psi|\hat{H}'|\Psi\rangle &= \langle\Psi|\hat{H}|\Psi\rangle + \langle\Psi|\hat{H}' - \hat{H}|\Psi\rangle \\ &= E_0 - \int n(\mathbf{r})\left[v(\mathbf{r}) - v'(\mathbf{r})\right] \mathrm{d}\mathbf{r} \qquad (2.12) \\ &< E_0'\end{aligned}$$

Adding equations (2.11) and (2.12), one obtains

$$E_0 + E_0' < E_0' + E_0 \qquad (2.13)$$

which is a contradiction. □

This means that the ground-state number density $n(\mathbf{r})$ uniquely determines the external potential, and hence all ground-state properties. We now write the total energy in an external potential v as a functional

$$E_v[n] = \int n(\mathbf{r})v(\mathbf{r})\mathrm{d}\mathbf{r} + F[n] \qquad (2.14)$$

of the electron density $n(\mathbf{r})$ (given by (2.7)), where $F[n]$ is the universal functional

$$F[n] = T[n] + V_{ee}[n] \qquad (2.15)$$

for the sum of kinetic and electron electron energies.

Caveat Note that in the above proof we have made use of the idea that any density represents the ground state of a Hamiltonian of type (2.10). This apparent restriction can be lifted however, as will be shown later, by means of the *Levy constrained-search* method.

The second Hohenberg-Kohn Theorem provides an energy variational principle in terms of the electron density $n(\mathbf{r})$.

Proposition (Hohenberg-Kohn theorem II). *For a trial density* $\tilde{n}(\mathbf{r})$, *such that* $\tilde{n}(\mathbf{r}) \geq 0$ *and* $\int \tilde{n}(\mathbf{r})\mathrm{d}\mathbf{r} = N$,

$$E_0 \leq E_v\left[\tilde{n}\right] \qquad (2.16)$$

where $E_v\left[\tilde{n}\right]$ *is the energy functional of* (2.14).

Proof. Let $\tilde{n}(\mathbf{r})$ be a trial wave function for the problem of Hamiltonian $\hat{H}$ with external potential $v(\mathbf{r})$. After Hohenberg-Kohn Theorem I, $\tilde{n}$ may be regarded as the ground-state density corresponding uniquely to a Hamiltonian $\hat{\tilde{H}}$ with ground-state wave function $\tilde{\Psi}$. The expectation value

$$\begin{aligned} \langle\tilde{\Psi}|\hat{H}|\tilde{\Psi}\rangle &= \int \tilde{n}(\mathbf{r})v(\mathbf{r})\mathrm{d}\mathbf{r} + F[\tilde{n}] \\ &= E_v[\tilde{n}] \end{aligned} \tag{2.17}$$

but

$$\langle\tilde{\Psi}|\hat{H}|\tilde{\Psi}\rangle \geq E_v[n] \tag{2.18}$$

by the usual variational principle of (2.5). □

Thus the problem of finding the ground state is reduced to a variational problem in the electron number density $n(\mathbf{r})$. Because of the reliance on theorem I, the same caveat applies. We now discuss the way in which this may be lifted.

2.5 Representability of densities

The first and second theorems of Hohenberg and Kohn describe the one-to-one correspondence of external potentials and ground-state densities, and the existence of a variational principle for the ground-state density. Both, however, are contingent upon the idea that any given density $n(\mathbf{r})$, corresponds to the antisymmetric ground-state density of a Hamiltonian of type (2.10) with some external potential v. A density which satisfies this criterion is described as "v-representable." If a trial density is not v-representable, the variational principle of Hohenberg-Kohn II ceases to apply. This is a highly stringent requirement, by no means satisfied for all reasonable densities; the problem can be circumvented, however by means of the Levy constrained-search formulation.

Consider the minimisation problem for (2.5) again, this time dividing our minimisation procedure into two steps. First we minimize our energy over all wave functions Ψ that produce a density $n(\mathbf{r})$. Then we minimize across all possible densities. That is to say

$$E_0 = \min_n \left\{ \min_{\Psi \to n} \left[\langle \Psi | \hat{T} + \hat{V}_{ee} | \Psi \rangle + \int v(\mathbf{r}) n(\mathbf{r}) \mathrm{d}\mathbf{r} \right] \right\} . \tag{2.19}$$

Now note that the internal minimisation step occurs for fixed $n(\mathbf{r})$, and choice of $\Psi \to n$ does not affect the value of the second term in (2.19). Thus we may write

$$\begin{aligned} E_0 &= \min_n \left\{ \min_{\Psi \to n} \left[\langle \Psi | \hat{T} + \hat{V}_{ee} | \Psi \rangle \right] + \int v(\mathbf{r}) n(\mathbf{r}) \mathrm{d}\mathbf{r} \right\} \\ &= \min_n \left\{ F[n(\mathbf{r})] + \int v(\mathbf{r}) n(\mathbf{r}) \mathrm{d}\mathbf{r} \right\} \end{aligned} \tag{2.20}$$

with F as in (2.15).

The above construction removes the requirement of v-representability altogether. The universal functional $F[n]$ is here defined by a constrained minimisation over wave functions of the Hamiltonian of an electron gas in the absence of an external potential. This is always well defined due to the ordinary variational principle of (2.5). Now no further constraint need be placed upon the minimisation over densities. As a result we have now lifted the requirement that trial densities be v-representable. In fact, trial densities need only be "N-representable" — that is to say, they correspond to some N-body wave function Ψ. The only necessary constraints remaining are the easily imposed conditions of positivity, normalisibility and continuity, which may be expressed:

$$n(\mathbf{r}) \geq 0, \quad \int n(\mathbf{r}) \mathrm{d}\mathbf{r} = N, \quad \text{and} \quad \int \left| \nabla n(\mathbf{r})^{1/2} \right|^2 \mathrm{d}\mathbf{r} < \infty. \tag{2.21}$$

2.6 Kohn-Sham density functional theory

Density functional theory as described above makes no prescription for the universal functional $F[n(\mathbf{r})]$. To approach this problem, Kohn and Sham [8] developed a method in terms of a non-interacting reference model, which, in combination with additional approximations, provides a systematic means of obtaining the ground state.

Let us write the universal functional $F[n]$ in the form

$$F[n] = T[n] + G[n] \tag{2.22}$$

where $T[n]$ is the kinetic energy of a system of non-interacting electrons of density $n(\mathbf{r})$. Then the total energy is given by

$$E[n] = \int \mathrm{d}\mathbf{r} v(\mathbf{r}) n(\mathbf{r}) + T[n] + G[n] \tag{2.23}$$

By Hohenberg-Kohn II, we have a variational principle for the energy which may be written

$$\delta E = \int \mathrm{d}\mathbf{r} \left[v(\mathbf{r}) + \frac{\delta T}{\delta n(\mathbf{r})} + \frac{\delta G}{\delta n(\mathbf{r})} \right] \delta n(\mathbf{r}) = 0 \tag{2.24}$$

at minimum, subject to the constant-number constraint

$$\int \delta n(\mathbf{r}) \mathrm{d}\mathbf{r} = 0 \ . \tag{2.25}$$

This constraint is handled by means of a Lagrange undetermined multiplier μ, yielding

$$\frac{\delta T}{\delta n(\mathbf{r})} + v(\mathbf{r}) + \frac{\delta G}{\delta n(\mathbf{r})} = \mu \tag{2.26}$$

where μ is now identified with the chemical potential. By defining an effective potential $v_{\text{eff}}(\mathbf{r}) = v(\mathbf{r}) + \frac{\delta G}{\delta n(\mathbf{r})}$, equation (2.26) becomes

$$\frac{\delta T}{\delta n(\mathbf{r})} + v_{\text{eff}}(\mathbf{r}) = \mu \ , \tag{2.27}$$

which is the Euler-Lagrange equation for a system of non-interacting electrons in an external potential $v_{\text{eff}}(\mathbf{r})$. This is, of course equivalent to the Schrödinger equation

$$\left[-\frac{1}{2}\nabla^2 + v_{\text{eff}}(\mathbf{r}) - \varepsilon_i \right] \psi_i = 0 \tag{2.28}$$

with

$$n(\mathbf{r}) = 2 \sum_{\varepsilon_i < \mu} |\psi_i(\mathbf{r})|^2 \tag{2.29}$$

for a spin-degenerate system. Equations (2.28) and (2.29) are known as the Kohn-Sham equations, and may be used in conjunction with equation (2.23) to find the ground state density and energy of the interacting system by an iterative solution.

2.7 The exchange-correlation energy

2.7.1 The Local Density Approximation

Up to now, we have avoided discussion of the function $v_{\text{eff}}(\mathbf{r})$; we will deal with this now. By separating out the Hartree energy, we may write

$$G[n] = \frac{1}{2} \int \mathrm{d}\mathbf{r}\mathrm{d}\mathbf{r}' \frac{n(\mathbf{r})n(\mathbf{r}')}{|\mathbf{r} - \mathbf{r}'|} + E_{\text{xc}}[n] \tag{2.30}$$

which gives

$$v_{\text{eff}}(\mathbf{r}) = v(\mathbf{r}) + \int \mathrm{d}\mathbf{r}' \frac{n(\mathbf{r}')}{|\mathbf{r} - \mathbf{r}'|} + v_{\text{xc}}(\mathbf{r}) \ , \tag{2.31}$$

where

$$v_{\text{xc}}(\mathbf{r}) = \frac{\delta E_{\text{xc}}[n(\mathbf{r})]}{\delta n(\mathbf{r})} \ . \tag{2.32}$$

$E_{\text{xc}}[n]$ now contains all parts of the effective potential which result from many-body effects; at the moment, however, there is no known way of calculating these exactly. We find also that there is no known expansion which will allow the functional to systematically approach exactness. Instead of this, we adopt one of several approximate representations of $v_{\text{xc}}(\mathbf{r})$ which have all been very successful. The simplest of these is know as the *Local Density Approximation* (LDA).

Using a combination of diagrammatic perturbation theory and other techniques, such as quantum Monte Carlo, the exchange-correlation energy of the homogeneous electron gas as a function of density $E^{\text{h}}_{\text{xc}}(n)$ has been tabulated and parameterized to a high degree of accuracy [11, 44, 45, 46]. The LDA approximation consists defining

$$E_{\mathrm{xc}}^{\mathrm{LDA}} \equiv \int \mathrm{d}\mathbf{r} n(\mathbf{r}) \varepsilon_{\mathrm{xc}}(n(\mathbf{r})) \ , \tag{2.33}$$

where $\varepsilon_{\mathrm{xc}}(n(\mathbf{r}))$ is the exchange-correlation energy per particle of an homogeneous electron gas with electron density $n(\mathbf{r})$. Equivalently, the exchange-correlation potential is now

$$\begin{aligned} v_{\mathrm{xc}}(\mathbf{r}) &= \frac{\delta E_{\mathrm{xc}}^{\mathrm{LDA}}}{\delta n(\mathbf{r})} \\ &= \varepsilon_{\mathrm{xc}}(n(\mathbf{r})) + n(\mathbf{r}) \left(\frac{\partial \varepsilon_{\mathrm{xc}}(n)}{\partial n} \right)_{n=n(\mathbf{r})} \end{aligned} \tag{2.34}$$

2.7.2 The exchange-correlation hole

The LDA has proved successful for many solids, but many problems remained elusive, particularly in regard to electron bonding. The natural extension would seem to be an expansion in derivatives of the electron density. Such an approach is termed a *Gradient Expansion Approximation* (GEA). It has been shown, however [47], that an expansion of the exchange-correlation energy to first derivative in the density violates certain known properties of E_{xc}. I outline without proof the most important of these properties here. For more details see e.g. [9].

The exchange-correlation energy may be regarded as the electrostatic interaction between an electron at a position $\mathbf{r}$, and an object known as the exchange-correlation hole, n_{xc}:

$$E_{\mathrm{xc}} = \frac{1}{2} \int \mathrm{d}\mathbf{r} n(\mathbf{r}) \int \mathrm{d}\mathbf{r}' \frac{1}{|\mathbf{r} - \mathbf{r}'|} n_{\mathrm{xc}}(\mathbf{r}, \mathbf{r}' - \mathbf{r}) \ . \tag{2.35}$$

The exchange-correlation hole describes the depletion of electronic charge in the neighbourhood of a given electron, due to Coulomb repulsion and Fermi statistics, and may be expressed exactly in terms of a coupling of the electronic structure factor $g(\mathbf{r}, \mathbf{r}', \lambda)$ of the system with density $n(\mathbf{r})$ and interelectron Coulomb interaction λV_{ee}:

$$n_{\rm xc}(\mathbf{r},\mathbf{r}'-\mathbf{r}) = n(\mathbf{r})\int_0^1 {\rm d}\lambda[g(\mathbf{r},\mathbf{r}',\lambda)-1]\,. \tag{2.36}$$

The $\lambda = 0$ value of the exchange-correlation hole is known as the exchange, or Fock hole $n_{\rm x}(\mathbf{r},\mathbf{r}'-\mathbf{r})$.

The exchange hole has the following known properties, which must be satisfied by any proposed representation of the exchange-correlation energy:

$$n_{\rm x}(\mathbf{r},\mathbf{0}) = -n(r)/2\,, \tag{2.37}$$

$$n_{\rm x}(\mathbf{r},\mathbf{r}'-\mathbf{r}) \leq 0\,, \tag{2.38}$$

$$\int {\rm d}\mathbf{r}' n_{\rm x}(\mathbf{r},\mathbf{r}'-\mathbf{r}) = -1\,. \tag{2.39}$$

Notably, the first-order GEA violates conditions (2.38) (negativity) and (2.39) (the sum rule) for the exchange hole.

2.7.3 The Generalized Gradient Approximation

To go beyond the LDA, therefore, clearly requires more than the obvious GEA approach. The one employed in this work, and indeed very widely, is the *Generalized Gradient Approximation* (GGA) of Perdew and Wang, known as PW91 [13]. This technique expresses the exchange-correlation energy as a functional of the spin-polarized electron densities, $n_\uparrow$ and $n_\downarrow$, and their gradients, $\nabla n_\uparrow$ and $\nabla n_\downarrow$ as follows

$$E_{\rm xc}^{\rm GGA}[n_\uparrow,n_\downarrow] = \int {\rm d}\mathbf{r} f(n_\uparrow(\mathbf{r}),n_\downarrow(\mathbf{r}),\nabla n_\uparrow(\mathbf{r}),\nabla n_\downarrow(\mathbf{r}))\,. \tag{2.40}$$

For slowly or moderately varying gradients, the GEA expansion gives a good first-order description at small distances $|\mathbf{r}'-\mathbf{r}|$; however at long range this description breaks down, and the negativity and sum rules are violated. To address this, the PW91 GGA has an analytic form which approaches the GEA for small $|\mathbf{r}'-\mathbf{r}|$, but imposes a sharp real-space cutoff at a radius chosen to ensure negativity and the sum rule for the exchange hole.

The expressions for the PW91 functionals are complicated, and their derivation more so, and they are not replicated here. They can be found in Ref. [13], with the full derivation given in Ref. [48].

2.8 Finite temperature density functional theory

To extend the Kohn-Sham method to finite temperature, we operate most conveniently in the grand canonical ensemble. Thus, the variable to be minimized becomes the grand potential Ω of the electronic subsystem. Before I proceed in this analysis, it is important to restate that electronic structure calculations are taking place in the Born-Oppenheimer approximation. As a result the temperature of the electrons, the precise definition of which will become clear in this section, is defined independently of the temperature of the underlying lattice. In our thermodynamic approach, it will be natural to make an identity between these, although at some points an approximation will be made of constant electronic temperature. In other methods, not employed in this work, the electronic temperature may be used as a parameter to aid the solution of a given problem; this is described as "quasi-zero temperature smearing". Again, the origin of the word "smearing" will become apparent as I proceed.

In order to proceed in a similar way to Sec. 2.6, we require that at a temperature θ, Ω should be a unique functional $\Omega[n]$of the density, and that it will be minimal for the thermal equilibrium number density $n(\mathbf{r})$. First, however, we require a relation analogous to the variational principle (2.5). We work in terms of the grand canonical statistical operator $\hat{\Gamma}$, which represents a statistical mixture of pure states with a *differing* number N of electrons, and follow the method describes in Ch. 2 of [5]. I will not, at this juncture discuss the details of the statistical operator approach to quantum mechanics, but proceed instead to a statement of the variational principle in the grand canonical ensemble. The equilibrium statistical operator is that which maximizes the entropy $S = -k_{\mathrm{B}}\mathrm{Tr}(\hat{\Gamma}\ln\hat{\Gamma})$, subject to the constraints of constant energy and constant particle number

$$\mathrm{Tr}\ (\hat{\Gamma}\hat{H}) = E \quad \text{and} \quad \mathrm{Tr}\ (\hat{\Gamma}\hat{N}) = N\,. \tag{2.41}$$

which yields the expression for the equilibrium statistical operator

$$\hat{\Gamma}^0 = \frac{e^{-\beta(\hat{H}-\mu\hat{N})}}{\mathrm{Tr}\ e^{-\beta(\hat{H}-\mu\hat{N})}}\,. \tag{2.42}$$

where the inverse temperature β, chemical potential μ, and trace in the denominator, result from Lagrange undetermined multipliers associated with the constraints of total energy, total particle number and normalisation respectively. Defining the grand potential by

$$\begin{aligned}\Omega[\hat{\Gamma}] &= E - \theta S - \mu N \\ &= \mathrm{Tr}\ \hat{\Gamma}\left(\frac{1}{\beta}\ln\hat{\Gamma} + \hat{H} - \mu\hat{N}\right)\end{aligned} \tag{2.43}$$

the variational principle in the grand canonical ensemble can be expressed

$$\Omega[\hat{\Gamma}] \geq \Omega[\hat{\Gamma}^0]\,. \tag{2.44}$$

The proof of this principle proceeds by expansion of $\hat{\Gamma}$ in its eigenstates, that is

$$\hat{\Gamma} = \sum_{Ni} p_{Ni}\,|\Psi_{Ni}\rangle\,\langle\Psi_{Ni}| \tag{2.45}$$

whence

$$\Omega[\{p_{Ni},\Psi_{Ni}\}] = \sum_{Ni} p_{Ni}\left(\frac{1}{\beta}\ln p_{Ni} + \langle\Psi_{Ni}|\hat{H}|\Psi_{Ni}\rangle + \mu N\right) \tag{2.46}$$

by (2.43). First we find the minimal statistical ensemble for fixed $\{\Psi_{Ni}\}$ and $\sum_{Ni} p_1 = 1$, ie.

$$\frac{\partial}{\partial p_{Ni}}\left[\Omega[\{p_{Ni},\Psi_{Ni}\}] + \lambda\left(\sum_{Ni} p_{Ni} - 1\right)\right] = 0\,, \tag{2.47}$$

where λ is some Lagrange undetermined multiplier, which preserves normalization. Then solving this for p_{Ni}, we find

$$p^0_{Ni} = \frac{\exp(-\beta\,\langle\Psi_{Ni}|\hat{H} - \mu\hat{N}|\Psi_{Ni}\rangle)}{\sum_{Ni}\exp(-\beta\,\langle\Psi_{Ni}|\hat{H} - \mu\hat{N}|\Psi_{Ni}\rangle)}\,, \tag{2.48}$$

which yields the grand potential

$$\Omega[\{p^0_{Ni},\Psi_{Ni}\}] = -\frac{1}{\beta}\ln\sum_{Ni}\exp(-\beta\,\langle\Psi_{Ni}|\hat{H}-\mu\hat{N}|\Psi_{Ni}\rangle);. \tag{2.49}$$

It remains to show that this is a minimum for fixed $\{\Psi_{Ni}\}$, and to then find the minimising wave functions Ψ_{Ni}. Using (2.48),

$$\begin{aligned}
&\Omega[\{p_{Ni},\Psi_{Ni}\}] - \Omega[\{p^0_{Ni},\Psi_{Ni}\}]\\
&\quad= \sum_{Ni} p_{Ni}\left(\frac{1}{\beta}\ln p_{Ni} + \langle\Psi_{Ni}|\hat{H}-\mu\hat{N}|\Psi_{Ni}\rangle\right)\\
&\quad\quad+\frac{1}{\beta}\ln\sum_{Ni}\exp(-\beta\,\langle\Psi_{Ni}|\hat{H}-\mu\hat{N}|\Psi_{Ni}\rangle)\\
&\quad= \frac{1}{\beta}\sum_{Ni} p_{Ni}(\ln p_{Ni} - \ln p^0_{Ni})\\
&\quad\quad-\frac{1}{\beta}\sum_{Ni} p_{Ni}\ln\sum_{N'i'}\exp(-\beta\,\langle\Psi_{N'i'}|\hat{H}-\mu\hat{N}|\Psi_{N'i'}\rangle)\\
&\quad\quad+\frac{1}{\beta}\ln\sum_{Ni}\exp(-\beta\,\langle\Psi_{Ni}|\hat{H}-\mu\hat{N}|\Psi_{Ni}\rangle)\,.
\end{aligned} \tag{2.50}$$

Since $\sum_{Ni} p_{Ni} = 1$, we see by interchange of indices that the last two terms in this expression cancel, leaving

$$\Omega[\{p_{Ni},\Psi_{Ni}\}] - \Omega[\{p^0_{Ni},\Psi_{Ni}\}] \tag{2.51}$$

$$= \frac{1}{\beta}\sum_{Ni} p_{Ni}(\ln p_{Ni} - \ln p^0_{Ni}) \geq 0\,. \tag{2.52}$$

The inequality shown here is known as the Gibbs inequality (Eqn. B.11 of [5]) and is true for all positive $\{p_\alpha\}$ s.t. $\sum_\alpha p_\alpha = 1$. It now follows that

$$\begin{aligned}
\Omega[\{p^0_{Ni},\Psi_{Ni}\}] &= -\frac{1}{\beta}\ln\sum_{Ni}\exp(-\beta\,\langle\Psi_{N'i'}|\hat{H}-\mu\hat{N}|\Psi_{N'i'}\rangle\\
&\geq -\frac{1}{\beta}\ln\sum_{Ni}\langle\Psi_{Ni}|e^{-\beta(\hat{H}-\mu\hat{N})}|\Psi_{Ni}\rangle\\
&\geq -\frac{1}{\beta}\ln\mathrm{Tr}\ e^{-\beta(\hat{H}-\mu\hat{N})}\\
&\geq \Omega[\{p^0_{Ni},\Psi^0_{Ni}\}]\,.
\end{aligned} \tag{2.53}$$

Where we have used $\left\langle f\left(\hat{O}\right)\right\rangle \geq f\left(\left\langle\hat{O}\right\rangle\right)$ for any convex function f of a Hermitian operator. This final expression is simply the equilibrium statistical operator Γ^0 of (2.42). This proves that the equilibrium statistical operator minimizes the grand potential Ω. It remains for us to provide a similar variational principle in the density $n(\mathbf{r})$, being an analogue of the Hohenberg-Kohn theorems of 2.4, and on that basis to construct a self consistent method similar to the ground state Kohn-Sham formalism.

We proceed by the method of a Levy constrained search. As discussed above (Sec. (2.5)), this removes any issues of representability, and removes the need for an explicit uniqueness theorem after Hohenberg-Kohn theorem I. We have

$$\begin{aligned}\Omega[\hat{\Gamma}^0] &= \min_{\Gamma} \mathrm{Tr}\left[\hat{\Gamma}\left(\hat{H}-\mu\hat{N}+\frac{1}{\beta}\ln\hat{\Gamma}\right)\right] \\ &= \min_{n}\left\{\min_{\Gamma\to n}\mathrm{Tr}\left[\hat{\Gamma}\left(\hat{T}+\hat{U}+\frac{1}{\beta}\ln\hat{\Gamma}\right)\right]+\int(v(\mathbf{r})-\mu)n(\mathbf{r})d\mathbf{r}\right\}\,.\end{aligned} \tag{2.54}$$

Defining the universal functional

$$F[n(\mathbf{r})] = \min_{\Gamma\to n}\mathrm{Tr}\left[\hat{\Gamma}\left(\hat{T}+\hat{U}+\frac{1}{\beta}\ln\hat{\Gamma}\right)\right] \tag{2.55}$$

we obtain

$$\Omega[\Gamma^0] = \min_{n}\Omega[n(\mathbf{r})]\,. \tag{2.56}$$

where

$$\Omega[n(\mathbf{r})] = F[n]+\int(v(\mathbf{r})-\mu)n(\mathbf{r})d\mathbf{r} \tag{2.57}$$

This is the analogue of Hohenberg-Kohn theorems I and II.

The finite temperature Kohn-Sham theory follows from consideration of a non-interacting reference system, with density $n(\mathbf{r})$ at a temperature θ. We define the non-interacting Helmholtz free energy of such a system to be

$$A[n] = T[n]-\theta S[n] \tag{2.58}$$

where T and S are, respectively, the kinetic energy and entropy of the non-interacting system. This gives us

$$\Omega[n] = A[n] + \int n(\mathbf{r})(v(\mathbf{r}) - \mu)\mathrm{d}\mathbf{r} + J[n] + F_{\mathrm{xc}}[n] \tag{2.59}$$

where $J[n]$ is the Hartree functional and $F_{\mathrm{xc}}[n]$ describes the exchange-correlation contribution to the free energy. Therefore the variational principle of (2.56) yields the Euler-Lagrange equation

$$\frac{\delta A[n]}{\delta n(\mathbf{r})} + v(\mathbf{r}) - \mu + \int \frac{n(\mathbf{r})}{|\mathbf{r} - \mathbf{r}'|}\mathrm{d}\mathbf{r}' + \frac{\delta F_{\mathrm{xc}}[n]}{\delta n(\mathbf{r})} = 0 \,. \tag{2.60}$$

Defining

$$v_{\mathrm{eff}}(\mathbf{r}) = v(\mathbf{r}) + \int \frac{n(\mathbf{r})}{|\mathbf{r} - \mathbf{r}'|}\mathrm{d}\mathbf{r}' + \frac{\delta F_{\mathrm{xc}}[n]}{\delta n(\mathbf{r})} \tag{2.61}$$

we have the Euler equation for a set of non-interacting electrons in an external potential $v_{\mathrm{eff}}(\mathbf{r})$. The grand potential for this ensemble is now

$$\Omega[n] = A[n] + \int n(\mathbf{r})(v_{\mathrm{eff}}(\mathbf{r}) - \mu)\mathrm{d}\mathbf{r} \tag{2.62}$$

yielding an equilibrium density operator

$$\hat{\Gamma}^0 = \frac{e^{-\beta(\hat{H}-\mu\hat{N})}}{\mathrm{Tr}\; e^{-\beta(\hat{H}-\mu\hat{N})}} \tag{2.63}$$

with

$$\hat{H} = -\frac{1}{2}\int \mathrm{d}x_1 \hat{\psi}^\dagger(x_1)\nabla^2\hat{\psi}(x_1) + \int \mathrm{d}x_1 \hat{\psi}^\dagger(x_1)\hat{\psi}(x_1)v_{\mathrm{eff}}(\mathbf{r}_1) \,. \tag{2.64}$$

As we are working in the grand canonical ensemble, and consider states across the Fock space of variable particle number, it has been necessary to invoke the notation of second quantisation. We finally obtain the finite temperature Kohn-Sham equations

$$\left[-\frac{1}{2}\nabla^2 + v_{\mathrm{eff}}(\mathbf{r})\right]\phi_i(\mathbf{r}) = \varepsilon_i\phi_i(\mathbf{r}) \,, \tag{2.65}$$

with the electron density given by

$$n(\mathbf{r}) = \sum_i^{\infty} f_i|\phi_i(\mathbf{r})|^2 \,. \tag{2.66}$$

Here f_i is the Fermi-Dirac occupation number of the band ϕ_i, given by

$$f_i = f(\varepsilon_i - \mu) = \frac{1}{1 + e^{-\beta(\varepsilon_i - \mu)}} \,, \tag{2.67}$$

which are the correct occupation numbers for a set of non-interacting electrons with temperature θ. We now see that the implementation of finite temperature Kohn-Sham DFT differs from the ground state formalism, only by the set of occupation numbers f_i, and a prescription for the exchange-correlation *free* energy, F_{xc}. For most practical implementations, one takes $F_{\mathrm{xc}}[n;\theta] = F_{\mathrm{xc}}[n;0]$. Note that this approximation retains the entropy of the non-interacting system in the term $A[n]$.

2.9 Forces — the Hellmann-Feynman theorem

Forces on nuclei are of primary importance in statistical mechanics. In this section, I discuss a theorem of Hellmann and Feynman [49], which provides a simple method for the calculation of nuclear forces, without multiple calculations of the total energy. The Hellmann-Feynman theorem, first for the case of all generalized forces. I comment on the application to nuclear forces, and I discuss the origins and effects of the so-called Pulay forces.

Consider a Hamiltonian $\hat{H}$, which depends upon a parameter λ, and let $\{\psi_i(\lambda)\}$ and $\{E_i(\lambda)\}$ be the normalized eigenstates and eigenvalues of $\hat{H}$. For a general state $\Psi = \sum_i c_i \psi_i$, we may write

$$\begin{aligned} \frac{\mathrm{d}E}{\mathrm{d}\lambda} &= \frac{\partial}{\partial\lambda} \sum_i \langle \psi_i | \hat{H} | \psi_i \rangle \, |c_i|^2 \\ &= \sum_i \left\{ \left\langle \frac{\partial\psi_i}{\partial\lambda} \middle| \hat{H} \middle| \psi_i \right\rangle + \left\langle \psi_i \middle| \frac{\partial\hat{H}}{\partial\lambda} \middle| \psi_i \right\rangle + \left\langle \psi_i \middle| \hat{H} \middle| \frac{\partial\psi_i}{\partial\lambda} \right\rangle \right\} . \end{aligned} \tag{2.68}$$

But

$$\begin{aligned} &\left\langle \frac{\partial\psi_i}{\partial\lambda} \middle| \hat{H} \middle| \psi_i \right\rangle + \left\langle \psi_i \middle| \hat{H} \middle| \frac{\partial\psi_i}{\partial\lambda} \right\rangle \\ &\qquad = E_i(\lambda) \left\langle \frac{\partial\psi_i}{\partial\lambda} \middle| \psi_i \right\rangle + E_i(\lambda) \left\langle \psi_i \middle| \frac{\partial\psi_i}{\partial\lambda} \right\rangle \\ &\qquad = E_i(\lambda) \frac{\partial}{\partial\lambda} \langle \psi_i | \psi_i \rangle = 0 \,, \end{aligned} \tag{2.69}$$

therefore

$$\frac{\mathrm{d}E}{\mathrm{d}\lambda} = \sum_i \left\langle \psi_i \middle| \frac{\partial \hat{H}}{\partial \lambda} \middle| \psi_i \right\rangle . \tag{2.70}$$

In the case $\lambda = R_{i\alpha}$, this yields an expression for the α-component $f_{i\alpha}$ of the force on the i^{th} atom due to the presence of the electrons

$$f_{i\alpha} = -\sum_j \left\langle \psi_j \middle| \frac{\partial \hat{H}}{\partial R_{i\alpha}} \middle| \psi_j \right\rangle . \tag{2.71}$$

For the Kohn-Sham Hamiltonian in Eqn. (2.28), this becomes

$$f_{i\alpha} = -\int \mathrm{d}\mathbf{r} n(\mathbf{r}) \frac{\partial v_{\text{eff}}(\mathbf{r})}{\partial R_{i\alpha}} , \tag{2.72}$$

but here only the electron-nucleus interaction, $v(\mathbf{r})$ depends explicitly on the $R_{i\alpha}$. As a result, the forces on the nuclei are simply the sum of the internuclear forces and the $f_{i\alpha}$, which represent the simple result from classical electrostatics

$$\mathbf{F}_i = \sum_j \frac{Z^2(\mathbf{R}_i - \mathbf{R}_j)}{R_{ij}^3} - \int \mathrm{d}\mathbf{r} \frac{Zn(\mathbf{r})(\mathbf{R}_i - \mathbf{r})}{|\mathbf{r} - \mathbf{R}_i|^3} . \tag{2.73}$$

A warning is necessary here. The Hellmann-Feynman theorem provides correct forces if and only if the ψ_i are the exact eigenstates of the Kohn-Sham Hamiltonian; an error is introduced whenever basis sets are incomplete. This spurious force contribution is known as a Pulay force. To examine this, we expand the ψ_i in a set of basis functions χ_m

$$\begin{aligned} \psi_i &= \sum_{m=1}^{\infty} \chi_m c_{mi} \\ &\approx \phi_i \equiv \sum_{m=1}^{N} \chi_m c_{mi} \end{aligned} \tag{2.74}$$

for $\{c_{mi}\}$ a set of complex numbers. Note the use of a cutoff value N; the $\{\phi_i\}$, which we shall use to approximate $\{\psi_i\}$ are no longer eigenfunctions of $\hat{H}$. We now have an approximation to the ground state energy, which depends not only on the $R_{i\alpha}$, but also on the basis functions and coefficients, that is

$$\begin{aligned} E &= E(\{\chi_m\}, \{c_{mj}\}, \{R_{i\alpha}\}) \,. \\ &= \sum_i \langle\phi_i|\hat{H}|\phi_i\rangle \\ &= \sum_i \varepsilon_i \sum_{l,m} c^*_{li} c_{mi} \, \langle\chi_l|\chi_m\rangle \\ &= \sum_i \varepsilon_i \sum_{l,m} c^*_{li} c_{mi} O_{lm} \,. \end{aligned} \tag{2.75}$$

We now consider the force

$$\begin{aligned} -f_{k\alpha} &= \frac{\mathrm{d}E}{\mathrm{d}R_{k\alpha}} \\ &= \frac{\partial E}{\partial R_{k\alpha}} + \sum_m \int \mathrm{d}^3 r \left[\frac{\delta E}{\delta \chi_m} \frac{\mathrm{d}\chi_m}{\mathrm{d}R_{k\alpha}} + \frac{\delta E}{\delta \chi^*_m} \frac{\mathrm{d}\chi^*_m}{\mathrm{d}R_{k\alpha}} \right] \\ &+ \sum_{im} \left[\frac{\partial E}{\partial c_{mi}} \frac{\mathrm{d}c_{mi}}{\mathrm{d}R_{k\alpha}} + \frac{\partial E}{\partial c^*_{mi}} \frac{\mathrm{d}c^*_{mi}}{\mathrm{d}R_{k\alpha}} \right] \,. \end{aligned} \tag{2.76}$$

From (2.75), we have

$$\frac{\partial E}{\partial c^*_{m}i} = \varepsilon_i \sum_l c_{li} O_{ml} ; \qquad \frac{\partial E}{\partial c_{m}i} = \varepsilon_i \sum_l c^*_{li} O_{lm} \,, \tag{2.77}$$

which gives

$$\begin{aligned} \frac{\mathrm{d}E}{\mathrm{d}R_{k\alpha}} &= \frac{\partial E}{\partial R_{k\alpha}} + \sum_m \int \mathrm{d}^3 r \left[\frac{\delta E}{\delta \chi_m} \frac{\mathrm{d}\chi_m}{\mathrm{d}R_{k\alpha}} + \frac{\delta E}{\delta \chi^*_m} \frac{\mathrm{d}\chi^*_m}{\mathrm{d}R_{k\alpha}} \right] \\ &+ \sum_i \varepsilon_i \sum_{ml} \left[c^*_{li} O_{lm} \frac{\mathrm{d}c_{mi}}{\mathrm{d}R_{k\alpha}} + c_{li} O_{ml} \frac{\mathrm{d}c^*_{mi}}{\mathrm{d}R_{k\alpha}} \right] \,. \end{aligned} \tag{2.78}$$

Now,

$$\langle\phi_i|\phi_i\rangle = 1 = \sum_{lm} c^*_{li} c_{mi} \, \langle\chi_l|\chi_m\rangle = \sum_{lm} c^*_{li} c_{mi} O_{lm} \tag{2.79}$$

whence, differentiating with respect to $R_{k\alpha}$,

$$\sum_{lm} \left[\frac{\mathrm{d}c^*_{li}}{\mathrm{d}R_{k\alpha}} c_{mi} O_{lm} + c^*_{li} \frac{\mathrm{d}c_{mi}}{\mathrm{d}R_{k\alpha}} O_{lm} + c^*_{li} c_{mi} \frac{\mathrm{d}O_{lm}}{\mathrm{d}R_{k\alpha}} \right] = 0 \,. \tag{2.80}$$

Inserting this into (2.78) gives

$$\begin{aligned} \frac{\mathrm{d}E}{\mathrm{d}R_{k\alpha}} &= \frac{\partial E}{\partial R_{k\alpha}} + \sum_m \int \mathrm{d}^3 r \left[\frac{\delta E}{\delta \chi_m} \frac{\mathrm{d}\chi_m}{\mathrm{d}R_{k\alpha}} + \frac{\delta E}{\delta \chi^*_m} \frac{\mathrm{d}\chi^*_m}{\mathrm{d}R_{k\alpha}} \right] \\ &- \sum_i \varepsilon_i \sum_{ml} c^*_{li} c_{mi} \int \mathrm{d}^3 r \left[\frac{\mathrm{d}\chi^*_l}{\mathrm{d}R_{k\alpha}} \chi_m + \chi^*_l \frac{\mathrm{d}\chi_m}{\mathrm{d}R_{k\alpha}} \right] \,. \end{aligned} \tag{2.81}$$

The first term in (2.81) is the force predicted by the Hellmann-Feynman theorem. The additional two terms are referred to as the Pulay force. We see that the Pulay force is non-zero only for basis states which depend explicitly on the ionic positions $\mathbf{R}_k$. So for a plane-wave basis, the Pulay forces are zero. We can consider this as being due to the fact that the completeness of the basis set is independent of ionic positions. For the projector augmented wave approach employed in this work, and discussed in section 2.11, we shall see that the use of atom-centred projector functions means that Pulay forces must be taken into account. At this stage, the analysis of forces need be taken no further.

2.10 Periodic boundary conditions and plane wave basis sets

So far, we have found a way of describing a system of interacting electrons in an external potential, in terms of a system of non-interacting electrons in some effective potential, which is a functional of the real potential and the electron density. Whilst a great simplification, this does not remove the problem of describing a system containing of the order of 10^{23} electrons and nuclei.

In solid state physics, and for crystals in particular, this problem can be addressed by the use of periodic boundary conditions. Bloch's theorem states that in a periodic potential $v(\mathbf{r} + \sum_{i=1}^{3} n_i \mathbf{l}_i) = v(\mathbf{r})$, where the $\mathbf{l}_i$ are lattice vectors, every electronic wave function may be written in the form

$$\psi_i(\mathbf{r}) = \exp[i\mathbf{k}.\mathbf{r}]u_i(\mathbf{r}) \tag{2.82}$$

where $u_i(\mathbf{r})$ is a cell-periodic function, which may be expanded in a plane wave basis

$$u_i(\mathbf{r}) = \sum_{\mathbf{G}} c_{i,\mathbf{G}} \exp[i\mathbf{G}.\mathbf{r}] \, . \tag{2.83}$$

Here the sum extends over all reciprocal lattice vectors $\mathbf{G}$ defined by $\mathbf{G}.\mathbf{l} = 2\pi m$, for all integers m and all $\mathbf{l} \in \{\mathbf{l}_1, \mathbf{l}_2, \mathbf{l}_3\}$. As described by Payne in [49], this changes the problem of calculating an infinite number of electronic wave functions, to that of calculating a finite number of electronic wave functions at an infinite number of points k in reciprocal space. This infinity is more easily addressed, however.

We re-write (2.82), (2.83) as

$$\psi_i(\mathbf{r}) = \sum_{\mathbf{G}} c_{i,\mathbf{k}+\mathbf{G}} \exp[i(\mathbf{k} + \mathbf{G}).\mathbf{r}] \ . \tag{2.84}$$

It is apparent that if $\mathbf{k} \to \mathbf{k} + \mathbf{G}$ then the term $\exp[i(\mathbf{k} + \mathbf{G}).\mathbf{r}]$ is unchanged (that is, the Brillouin zone is homeomorphic to the three-torus $\mathbb{T}^3$). Calculation of the wave function is therefore performed only within the Brillouin zone. The wave function can obviously be calculated at only a finite number of k-points. Monkhorst and Pack [50] suggest a scheme, adopted here, for selecting those k-points at which ψ will be calculated, which has been shown to produce good convergence of energy with increasing k-point-sampling density.

One final observation needs to be made about k-point sampling, which is of great relevance to this work. Many of the techniques I employ, require the use of so called super-cells, which are repetitions of the primitive unit cell of the lattice, containing many atoms. The reasons for this will be discussed in detail when those techniques are introduced. However, note that for super-cells with larger and larger unit vectors $\mathbf{l}$, the length of the reciprocal lattice vectors $\mathbf{G}$ becomes shorter, and the Brillouin zone contracts. To maintain a constant accuracy of sampling at ever larger super-cell sizes, fewer k-points are required than for smaller cells.

2.11 Pseudopotentials and the projector augmented wave approach

The ideas introduced so far in this chapter, provide the theoretical basis for performing electronic structure calculations: we solve the finite-temperature Kohn-Sham equations in a plane-wave basis, by direct minimisation of the electronic free energy U as a function of a set of plane-wave coefficients c_i at a set of k-points in the first Brillouin zone. The density of k-points and the number of plane wave coefficients must be taken to convergence. In practice, the latter is achieved by selecting an energy cutoff E_{cut}, and stipulating that $|\mathbf{k}+\mathbf{G}|^2 \leq E_{\text{cut}}$.

Whilst providing a tractable method in principle, this approach does not, as it stands, provide a practical approach for any but a very few systems. The reason for this is that, while a plane-wave basis has many advantages for periodic systems, it is ill-suited to describing the rapidly oscillating wave function in the vicinity of atomic cores, which require the use of very large basis sets. The various pseudopotential methods [51, 52, 53, 54, 55] exist to address this problem.

Central to the pseudopotential idea is the principle that the important physical properties of solids are determined predominantly by the behaviour of the valence electrons outside some cutoff radius, r_c. It is natural therefore, to make the following approximations. Firstly, one separates wave functions into a set of core states which are not permitted to change, and a set of valence states which are minimized among all states orthogonal to the core states; this is the frozen core approximation. Secondly, one replaces the potential V_{core} due to nuclei and core electrons with a so-called pseudopotential V_{ps}, such that $V_{\text{ps}} = V_{\text{core}}$ for distances greater than r_c from atom centres. Subject to a variety of conditions on V_{ps}, this can be done so that the core-orthogonal solutions of the pseudopotential (the pseudo wave func-

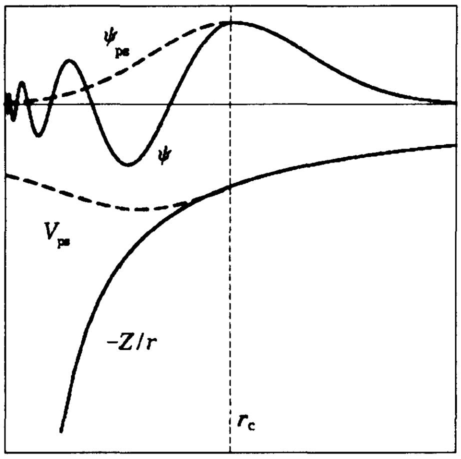

Figure 2.1: Typical smoothing of core wave function by use of pseudopotentials. ψ and $\psi_{\rm ps}$ are the true and pseudized wave functions, corresponding to the $-Z/r$ Coulomb potential, and $V_{\rm ps}$ pseudopotential respectively.

tions $\tilde{\psi}$) are equal to the valence wave functions ψ outside of the atom cores. The idea of the pseudopotential approximation is to do this in such a way that the pseudo wave function is smooth within the core region, permitting improved convergence behaviour with plane-wave cutoff. Fig. 2.1, after [49], illustrates this this behaviour.

The fundamental requirements of pseudopotentials are that they reproduce correctly the scattering properties of the true wave functions; that they be as *transferable* as possible; and that $\tilde{\psi}$ is as smooth as possible. In respect of the first of these, the phase shift produced by the ionic core is different for each angular momentum component of the valence wave function. In order that the pseudopotential correctly reproduces scattering outside the core region, we require in general that our pseudopotential be angular momentum dependent, that is

$$V_{\rm ps} = \sum_{lm} |lm\rangle \, V_l \, \langle lm| \ . \tag{2.85}$$

In respect of the requirements of transferability and smoothness, it is clear that the smaller the core radius, the better the transferability of the pseudopotential. However, for a norm-conserving pseudopotential [51, 52, 53, 54], for which $\int_{r<r_\mathrm{c}} \mathrm{d}x \, \langle x| \, (|\psi\rangle \, \langle\psi| - |\tilde{\psi}\rangle \, \langle\tilde{\psi}| \, |x\rangle = 0$, a small core radius can lead to pseudo wave functions that are no smoother than the true core wave function. The first effective pseudopotential method to relax the norm-conservation requirement was that of Vanderbilt [55], but I will discuss here the related *projector augmented wave* (PAW) approach of Blöchl [14], which is used in all my calculations.

The PAW method seeks to improve upon the pseudopotential approach by defining an invertible linear operate τ between true and pseudo wave functions, such that

$$\psi = \tau\tilde{\psi} \, . \tag{2.86}$$

This allows one to calculate the true expectation values of dynamical variables, rather than their pseudopotential approximations, by defining the pseudized dynamical variables $\tilde{A} = \tau^\dagger A \tau$ such that

$$\begin{aligned} \langle A \rangle &= \langle \psi | A | \psi \rangle \\ &= \langle \psi | \tau\tau^\dagger A \tau\tau^\dagger | \psi \rangle \\ &= \langle \tilde{\psi} | \tilde{A} | \tilde{\psi} \rangle \; . \end{aligned} \tag{2.87}$$

I will describe in brief the form of the operator τ, in order to paint a picture of the PAW method, and make a few observations, but as it has not been the goal of the work to implement the PAW method, I will not discuss these matters in detail.

I adopt Blöchl's own notation [14] here, so let Ω, the augmentation region, be a sphere of radius r_c about each ionic core. We then have $\tilde{\psi} = \psi$ outside Ω, so we write

$$\tau = 1 + \sum_R \tau_R \, , \tag{2.88}$$

where each τ_R is a local, atom-centred contribution, acting solely in the region Ω_R. The sum goes over all atom centres labelled R. We expand the real and pseudo valence wave functions within each Ω_R in a set of real and pseudo *partial waves* $|\phi\rangle$ and $|\tilde{\phi}\rangle$, with $|\phi\rangle = (1 + \tau_R)\,|\tilde{\phi}\rangle$. We then have

$$\begin{aligned} |\tilde{\psi}\rangle &= \sum_i c_i\,|\tilde{\phi}_i\rangle \\ |\psi\rangle &= \sum_i c_i\,|\phi_i\rangle \end{aligned} \tag{2.89}$$

within Ω_R. Since $|\phi\rangle = |\tilde{\phi}\rangle$ outside all the Ω_R, we can express the valence wave function as

$$|\psi\rangle = |\tilde{\psi}\rangle - \sum_i |\tilde{\phi}_i\rangle\, c_i + \sum_i |\phi_i\rangle\, c_i\ . \tag{2.90}$$

The coefficients are obtained in terms of a set of projector functions $|\tilde{p}_i\rangle$:

$$c_i = \langle \tilde{p}_i | \tilde{\psi} \rangle\ , \tag{2.91}$$

which are dual to the partial waves, i.e.

$$\langle \tilde{p}_i | \tilde{\phi}_j \rangle = \delta_{ij}\ . \tag{2.92}$$

We now have a linear transformation

$$\tau = 1 + \sum_i (|\phi_i\rangle - |\tilde{\phi}_i\rangle)\,\langle \tilde{p}| \tag{2.93}$$

between our real and pseudo valence wave function, such that

$$|\psi\rangle = |\tilde{\psi}\rangle + \sum_i (|\phi_i\rangle - |\tilde{\phi}_i\rangle\,\langle \tilde{p}_i | \tilde{\psi}\rangle\ . \tag{2.94}$$

One is free to choose the form of the $\{\tilde{p}_i\}$ to maximize smoothing of the pseudo wave function, and transferability of the parameterisation (the set of projectors).

One further note should be made here. It was mentioned in sec. 2.10, that there are no Pulay forces in a plane wave basis set. However, when we use the PAW method, the locality of the projectors means that Pulay forces must be accounted for. Similar corrections will occur in the calculation of stresses.

$S = k \ln \Omega$

Ludwig Boltzmann (1844–1906)

Chapter 3

From statistical mechanics to thermodynamics

This chapter will consider a variety of approaches, of varying rigour and varying difficulty, to the thermodynamics of a system. Each begins with the total configurational energy of the system $U(\{\mathbf{R}_i\}; \{\lambda_j\}, T_{el})$ and proceeds to a calculation of the free energy of the vibrating lattice.

First of all, in sec. 3.1, I introduce and discuss important thermodynamic quantities, and their relation to statistical mechanics. Sec. 3.2 describes the theory of the harmonic lattice. This permits one to calculate the free energy of a system in the approximation of an interatomic potential quadratic in atomic displacements. From this free energy, one can proceed to the calculation of other thermodynamic averages.

Sec. 3.3 describes molecular dynamics. This is a general approach to the fully anharmonic calculation of thermodynamic averages (the term anharmonic will be defined more clearly later). I also discuss here thermodynamic integration, a method which permits one to calculate free energies from molecular dynamics trajectories.

Finally, sec 3.4 introduces the particle-in-cell (PIC) model of the lattice, which purports to approximate the anharmonic free energy of a lattice in a highly efficient way.

3.1 Thermodynamics background

Here I discuss important background concepts in thermodynamics, list some of the more important thermodynamic functions of state, explain how they relate to a microscopic description, and derive a variety of important relations between them. While many of these will be familiar to the reader, certain of these relations will be of great importance in discussing thermoelasticity in Ch. 4, and they are introduced here to help provide a continuous development of the theory.

3.1.1 Ensembles of systems

In this work, I consider the statistical mechanics of systems of constant particle number N, at a constant volume V and temperature T. To understand how this is achieved in molecular dynamics (see sec. 3.3), it is important to understand the statistical mechanics of both the canonical (constant N, V, T) and microcanonical (constant N, V, E) ensembles.

In the canonical ensemble, a system in thermodynamic equilibrium is found to be in a state j of energy E_j with probability

$$P_j = \frac{1}{Z(N,V,T)} e^{-\beta E_j} \tag{3.1}$$

where $\beta = 1/k_{\mathrm{B}}T$. The partition function $Z(N,V,T)$ is given by

$$Z(N,V,T) = \sum_j e^{-\beta E_j} \tag{3.2}$$

The measured value of a macroscopic observable at equilibrium is given by

$$\begin{aligned} A(N,V,T) &= \langle A \rangle \\ &= \sum_j A_j P_j \end{aligned} \tag{3.3}$$

where A_j is the value of the observable when the system is in state j.

The Helmholtz free energy is defined as $F = E - TS$, and is a minimum for a system in the canonical ensemble at thermal equilibrium. From the first law of thermodynamics, $\mathrm{d}E = T\mathrm{d}S - p\mathrm{d}V$, we can write

$$\mathrm{d}F = -S\mathrm{d}T - p\mathrm{d}V \,. \tag{3.4}$$

By using the definition of entropy in the canonical ensemble, we have

$$\begin{aligned} S &= -k_\mathrm{B} \sum_j P_j \ln P_j \\ &= -k_\mathrm{B} \left\langle \ln \left\{ Z^{-1} e^{-\beta E_j} \right\} \right\rangle \\ &= -k_\mathrm{B} \left\langle \frac{E}{T} - \ln Z \right\rangle \\ \Rightarrow \quad F &= E - TS = -k_\mathrm{B} T \ln Z \,. \end{aligned} \tag{3.5}$$

3.1.2 Thermodynamic Functions

We can use the Helmholtz free energy as a starting point to determine all the thermodynamic functions we wish, in the canonical ensemble. The goal of all the methods described in this section is the calculation of thermodynamic functions of state as derivatives of the Helmholtz free energy. I introduce some of these functions now. Most of these can be found in a standard thermodynamics text, i.e. [56]. From the differential relation (3.4) we have,

$$p = -\left(\frac{\partial F}{\partial V}\right)_T \,, \tag{3.6}$$

from which we can calculate quantities such as the isothermal and adiabatic (isentropic) bulk moduli

$$K_{T,S} \equiv -V \left(\frac{\partial p}{\partial V}\right)_{T,S} \,. \tag{3.7}$$

The total energy of the system is given by

$$\begin{aligned} E &= \frac{1}{Z}\sum_j E_j e^{-\beta E_j} \\ &= -\frac{1}{Z}\frac{\partial Z}{\partial \beta} = \frac{1}{Z}k_{\mathrm{B}}T^2\frac{\partial Z}{\partial T} \\ &= k_{\mathrm{B}}T^2\left(\frac{\partial \ln Z}{\partial T}\right)_V , \end{aligned} \tag{3.8}$$

i.e.

$$E = F - T\left(\frac{\partial F}{\partial T}\right)_V , \tag{3.9}$$

which will allow us to calculate quantities such as the heat capacities at constant pressure or constant volume

$$C_{V,p} \equiv T\left(\frac{\partial S}{\partial T}\right)_{V,p} . \tag{3.10}$$

Several other thermodynamic functions will be of interest, and I introduce them now, and derive relations that will permit them to be calculated. The thermal volumetric expansivity is defined by

$$\alpha K_T \equiv \left(\frac{\partial p}{\partial T}\right)_V . \tag{3.11}$$

Linear expansivities in inhomogeneous solids will be discussed in the next section.

How can we relate the heat capacities at constant volume and temperature? Beginning from the first law, $\mathrm{d}q = \mathrm{d}E + p\mathrm{d}V$, one has

$$\begin{aligned} C_V &\equiv \left(\frac{\partial q}{\partial T}\right)_V = \left(\frac{\partial E}{\partial T}\right)_V \\ \text{and} \quad C_p &\equiv \left(\frac{\partial q}{\partial T}\right)_p \\ &= \left(\frac{\partial E}{\partial T}\right)_p + p\left(\frac{\partial V}{\partial T}\right)_p . \end{aligned} \tag{3.12}$$

Comparing this with the chain rule result:

$$\left(\frac{\partial E}{\partial T}\right)_p = \left(\frac{\partial E}{\partial T}\right)_V + \left(\frac{\partial E}{\partial V}\right)_T\left(\frac{\partial V}{\partial T}\right)_p \tag{3.13}$$

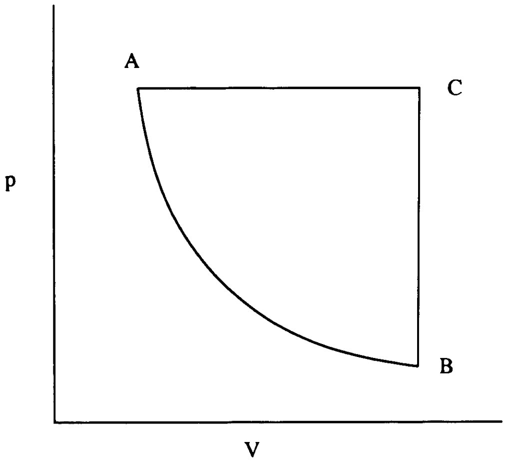

Figure 3.1: Heat cycle.

gives

$$C_p = \left(\frac{\partial E}{\partial T}\right)_V + \left[p + \left(\frac{\partial E}{\partial V}\right)_T\right]\left(\frac{\partial V}{\partial T}\right)_p . \tag{3.14}$$

Using again the first law, $\mathrm{d}E = T\mathrm{d}S - p\mathrm{d}V$, we have

$$\begin{aligned}\left(\frac{\partial E}{\partial V}\right)_T &= T\left(\frac{\partial S}{\partial V}\right)_T - p \\ &= T\left(\frac{\partial p}{\partial T}\right)_V - p\end{aligned} \tag{3.15}$$

where the Maxwell relation $(\partial S/\partial_V)_T = (\partial p/\partial_T)_V$ follows from taking second derivatives of (3.4). Finally we have

$$\begin{aligned}C_p - C_V &= T\left(\frac{\partial p}{\partial T}\right)_V\left(\frac{\partial V}{\partial T}\right)_p \\ &= TV\alpha^2 K_T .\end{aligned} \tag{3.16}$$

I can now relate the isothermal and adiabatic heat capacities. Consider the cycle shown in fig. 3.1. Along the adiabat AB

$$\mathrm{d}U = -p\mathrm{d}V ; \tag{3.17}$$

along AC

$$\begin{aligned}\mathrm{d}U &= \mathrm{d}q - p\mathrm{d}V \\ &= C_V\mathrm{d}T_1 - p\mathrm{d}V ;\end{aligned} \tag{3.18}$$

and along CB

$$\begin{aligned} \mathrm{d}U &= \mathrm{d}q \\ &= C_p \mathrm{d}T_2 \,. \end{aligned} \tag{3.19}$$

We find that

$$C_V \mathrm{d}T_1 + C_p \mathrm{d}T_2 = 0 \,. \tag{3.20}$$

Now, as AC occurs at constant pressure and CB at constant volume, we have,

$$\mathrm{d}T_1 = \left(\frac{\partial T}{\partial V}\right)_p \mathrm{d}p \tag{3.21}$$

and

$$\mathrm{d}T_2 = \left(\frac{\partial T}{\partial p}\right)_V \mathrm{d}V \,, \tag{3.22}$$

whence

$$C_p \left(\frac{\partial T}{\partial V}\right)_p \mathrm{d}V + C_V \left(\frac{\partial T}{\partial p}\right)_V \mathrm{d}p = 0 \,. \tag{3.23}$$

Now, recall that $\mathrm{d}p$ and $\mathrm{d}V$ here relate to an adiabatic change. Thus

$$\begin{aligned} C_V \left(\frac{\partial p}{\partial V}\right)_S &= -C_p \frac{(\partial T/\partial V)_p}{(\partial T/\partial p)_V} \\ &= C_p \left(\frac{\partial p}{\partial V}\right)_T \end{aligned} \tag{3.24}$$

or

$$\frac{K_S}{K_T} = \frac{C_p}{C_V} \,. \tag{3.25}$$

The only important quantity remaining to be introduced is the so-called (first) Grüneisen parameter, defined

$$\begin{aligned} \gamma &\equiv \frac{V}{C_V} \left(\frac{\partial p}{\partial T}\right)_V \\ &= \frac{V \alpha K_T}{C_V} = \frac{V \alpha K_S}{C_p} \,. \end{aligned} \tag{3.26}$$

We can use this to write down the ratio of specific heats,

$$\Gamma \equiv \frac{C_p}{C_V} = \frac{K_S}{K_T} = (1 + \alpha \gamma T) \,. \tag{3.27}$$

3.1.3 Classical systems

Having defined the Helmholtz free energy and demonstrated how to extract thermodynamic functions of interest, we now observe how such quantities are calculated for a classical system of N indistinguishable, interacting particles. The microstates of such a system are labelled by the $6N$ coordinates and momenta of the system, and have energy

$$E(\mathbf{p}_1 \ldots \mathbf{p}_N, \mathbf{R}_1 \ldots \mathbf{R}_N) = \sum_i \frac{p_i^2}{2M} + U(\mathbf{R}_1, \ldots \mathbf{R}_N) \, . \tag{3.28}$$

In the case of *ab initio* simulation at finite temperature, the potential U refers to the free-energy of the electron-ion system, with all nuclei static on their equilibrium sites. It thus depends on the temperature of the system through electronic excitations. Equations (3.2) and (3.28) appear to offer a prescription for obtaining the partition function. Before we can do this however, we need to decide how many microstates exist in a volume $\mathrm{d}\Gamma = \mathrm{d}^{3N}\mathbf{R}\mathrm{d}^{3N}\mathbf{p}$ of phase space. From investigating the crossover between quantum mechanical and classical systems, one finds that there are

$$\mathrm{d}n = \frac{\mathrm{d}\Gamma}{h^{3N}N!} = \frac{\mathrm{d}^{3N}\mathbf{R}\mathrm{d}^{3N}\mathbf{p}}{h^{3N}N!} \tag{3.29}$$

microstates in an element $\mathrm{d}\Gamma$ of phase space, where the N! accounts for the fact that the two states generated by permuting two particles are not distinct. This gives a classical partition function

$$\begin{aligned} Z(N,V,T) &= \frac{1}{h^{3N}N!} \int \mathrm{d}^{3N}\mathbf{R} \int \mathrm{d}^{3N}\mathbf{p} e^{-\beta E(\mathbf{p}_1 \ldots \mathbf{p}_N, \mathbf{R}_1 \ldots \mathbf{R}_N)} \\ &= \frac{1}{\Lambda^{3N}N!} \int \mathrm{d}^{3N}\mathbf{R} e^{-\beta U(\mathbf{R}_1, \ldots \mathbf{R}_N)} \, , \end{aligned} \tag{3.30}$$

where $\Lambda = h/(2\pi M k_\mathrm{B} T)^{1/2}$ is the thermal wavelength. Using (3.5), the Helmholtz free energy is then

$$F = -k_\mathrm{B} T \ln \left\{ \frac{1}{\Lambda^{3N}N!} \int \mathrm{d}^{3N}\mathbf{R} e^{-\beta U(\mathbf{R}_1, \ldots \mathbf{R}_N)} \right\} \, . \tag{3.31}$$

It is now useful to separate the free energy into components $F = F_\mathrm{perf} + F_\mathrm{vib}$, where $F_\mathrm{perf} = U(\mathbf{R}_1^0 \ldots \mathbf{R}_N^0)$ is the free energy of the static lattice. We similarly separate U into $U(\mathbf{R}_1 \ldots \mathbf{R}_N) = F_{\text{perf}} + \Phi(\mathbf{R}_1 \ldots \mathbf{R}_N)$. From this point we treat each atom as being distinguishable by lattice site, and thus drop the factor of N! from the following expressions. We have

$$\begin{aligned} F &= F_{\text{perf}} + F_{\text{vib}} \\ &= -k_{\text{B}}T \ln \left\{ \frac{1}{\Lambda^{3N}} e^{-\beta F_{\text{perf}}} \int \mathrm{d}^{3N}\mathbf{R} e^{-\beta\Phi(\mathbf{R}_1 \ldots \mathbf{R}_N)} \right\} \qquad (3.32) \\ &= F_{\text{perf}} - k_{\text{B}}T \ln \left\{ \frac{1}{\Lambda^{3N}} \int \mathrm{d}^{3N}\mathbf{R} e^{-\beta\Phi(\mathbf{R}_1 \ldots \mathbf{R}_N)} \right\} . \end{aligned}$$

Our final separation of components, is between harmonic and anharmonic contributions, and is the subject of Sec. 3.2. In Sec. 3.2.6 I will describe departures from the classical description of the lattice.

3.1.4 Shock experiments — the Hugoniot

An important relation in describing shock-wave experiments is the Rankine-Hugoniot equation (see [57] pp. 96–100). This expression allows one to compute the pressure-volume and temperature-pressure relations on the so-called Hugoniot equation of state: the locus of possible $p, V, T)$ outcomes of a shock-wave experiment for given initial conditions p_0, V_0, T_0.

In a shock experiment [27], a planar wave front is passed through a material, and the volume, pressure and (sometimes) temperature behind the wavefront are measured. The Rankine-Hugoniot equations describe this process, by assuming that the shock-wave consists of a very short rise-time, over which the density of the sample increases sharply, and a very long tail, over which the system returns to ambient ambient temperature and pressure. It is assumed that behind the shock front, the sample is in equilibrium at the higher temperature and pressure. The whole process is taken to be adiabatic.

Consider a cylindrical sample of unit cross-section. A shock front passing from left to right with velocity U_{s} imparts a left-to-right velocity u_{p} to the material behind the front. We make use of conservation of mass, momentum and energy to obtain the Rankine-Hugoniot equations.

Consider the sample now in the rest frame of the shock front. We imagine matter passing from right to left through the shock front, where it slows from a velocity of U_s to a velocity of $U_\mathrm{s} - u_\mathrm{p}$. By conservation of mass

$$U_\mathrm{s}\rho_0 = (U_\mathrm{s} - u_\mathrm{p})\rho = \mu \,, \tag{3.33}$$

where ρ_0 and ρ are the densities to the right and left of the shock front respectively, and μ is the rate of flow of mass through the shock front.

The rate of momentum increase of the matter passing through the shock front is equal to the difference in force across the shock front. Therefore

$$p - p_0 = \mu u_\mathrm{p} = U_\mathrm{s} u_\mathrm{p} \rho_0 . \tag{3.34}$$

Finally, per unit time, the increase in internal energy, plus the kinetic energy imparted to the material must equal the work done by the force across the shock front:

$$p_0 U_\mathrm{s} - p(U_\mathrm{s} - u_\mathrm{p}) = \mu \left[E - E_0 + \frac{1}{2}(U_\mathrm{s} - u_\mathrm{p})^2 - \frac{1}{2}U_\mathrm{s}^2 \right] \,, \tag{3.35}$$

where E_0 and E are the internal energy per unit mass in front of and behind the wave front. This yields

$$U_\mathrm{s}^2 = (p = p_0) \left[\frac{\rho}{\rho_0}(\rho - \rho_0) \right] \,. \tag{3.36}$$

Writing the specific volume $V = 1/\rho$, this is equivalent to

$$U_\mathrm{s} = V_0 \left(\frac{p - p_0}{V_0 - V} \right)^{1/2} \,. \tag{3.37}$$

And using (3.34), we arrive at the Rankine-Hugoniot equation:

$$E - E_0 = \frac{1}{2}(p + p_0)(V_0 - V) \,. \tag{3.38}$$

A theoretical equation of state for a material can be solved self-consistently with the Rankine-Hugoniot equation to eliminate either the temperature or volume, and so obtain the pressure-volume and temperature-pressure relations on the Hugoniot, which can be directly compared with shock-wave experiments.

3.2 Theory of the harmonic lattice

3.2.1 Thermodynamic motivation

I now proceed to a discussion of the use of the harmonic approximation to calculate Helmholtz free energies. See for example [2]. As a first step, suppose that the free energy of a classical system may be written as a homogeneous, diagonal quadratic function of some $3N$ generalized coordinates q_i, that is:

$$\Phi = \sum_i M \frac{1}{2} \omega_i^2 q_i^2 \,. \tag{3.39}$$

Then from (3.32),

$$\begin{aligned} F_{\text{vib}} &= -k_{\text{B}}T \ln \left\{ \frac{1}{\Lambda^{3N}} \prod_{i=1}^{3N} \int \mathrm{d}q_i \exp\left[-\beta M \omega_i^2 q_i^2/2\right] \right\} \\ &= -k_{\text{B}}T \sum_{i=1}^{3N} \ln \left\{ \frac{1}{\Lambda} \left(\frac{2\pi k_{\text{B}}T}{M\omega_i^2} \right)^{1/2} \right\} \\ &= k_{\text{B}}T \sum_{i=1}^{3N} \ln \frac{\hbar\omega_i}{k_{\text{B}}T} \\ &= 3Nk_{\text{B}}T \ln \frac{\hbar\bar{\omega}}{k_{\text{B}}T} \,, \end{aligned} \tag{3.40}$$

where we have defined

$$\ln \bar{\omega} \equiv \frac{1}{3N} \sum_{i=1}^{3N} \ln \omega_i \,. \tag{3.41}$$

In other words, if we can find a set of generalized coordinates in which the potential takes, or is approximated by the form (3.39), we can calculate the free energy directly by means of (3.40). This section deals with how how to find these coordinates.

3.2.2 Equations of motion

Consider a lattice having some origin, O, and lattice vectors $\mathbf{a}_1$, $\mathbf{a}_2$ and $\mathbf{a}_3$. It is comprised of an infinite number of unit cells, which we label $\mathbf{l} = (l_1, l_2, l_3)$, $\mathbf{l} \in \mathbb{Z}^3$, having origins at $\mathbf{R}_{\mathbf{l}}^0 = \sum_{i=1}^{3} l_i \mathbf{a}_i$. Each unit cell contains n atoms with equilibrium positions $\mathbf{R}_s$, $s \in \{1, 2, \dots, n\}$ relative to $\mathbf{R}^0_{\mathbf{l}}$. The position relative to O of any equilibrium atomic site in the lattice may then be written $\mathbf{R}^0_{\mathbf{l}s} = \mathbf{R}^0_{\mathbf{l}} + \mathbf{R}_s$. If we then displace each atom by a vector $\mathbf{u}_{\mathbf{l}s}$, the position of each atom under such displacements is $\mathbf{R}_{\mathbf{l}s} = \mathbf{R}^0_{\mathbf{l}s} + \mathbf{u}_{\mathbf{l}s}$.

For small displacements of the atoms, the potential energy of the system may be written as a Taylor expansion in the $\mathbf{u}_{lk}$ thus:

$$\Phi = \Phi_0 + \sum_{\mathbf{l}s\mu} \Phi_{\mathbf{l}s\mu} u_{\mathbf{l}s\mu} + \frac{1}{2!} \sum_{\mathbf{l}s\mu\mathbf{l}'s'\nu} \Phi_{\mathbf{l}s\mu,\mathbf{l}'s'\nu} u_{\mathbf{l}s\mu} u_{\mathbf{l}'s'\nu} + \dots \tag{3.42}$$

where μ, ν label the Cartesian coordinate axes. The constant Φ_0 and the tensors

$$\Phi_{\mathbf{l}s\mu} = \left(\frac{\partial \Phi}{\partial u_{\mathbf{l}s\mu}} \right)_0 \tag{3.43}$$

and

$$\Phi_{\mathbf{l}s\mu,\mathbf{l}'s'\nu} = \left(\frac{\partial^2 \Phi}{\partial u_{\mathbf{l}s\mu} \partial u_{\mathbf{l}'s'\nu}} \right)_0 , \tag{3.44}$$

(here the subscript 0 indicates evaluation at $\mathbf{u}_{\mathbf{l}s} = 0$), are defined for a particular lattice, and are functions of strain. It is clear that $\Phi_{\mathbf{l}s\mu,\mathbf{l}'s'\nu}$ depends on the cell index $\mathbf{l}$ only through $\mathbf{l} - \mathbf{l}'$, and we will make use of the notation $\Phi^{\mathbf{l}-\mathbf{l}'}_{k\mu,k'\nu} \equiv \Phi_{\mathbf{l}s\mu,\mathbf{l}'s'\nu}$.

The zeroth-order term in (3.42) can be absorbed into the perfect lattice term F_{perf} of (3.32), and taken to be zero, while the first-order terms are the negatives of the forces on the atoms in their equilibrium positions, and are therefore all zero. The harmonic approximation consists in ignoring all terms of order $\mathbf{u}^3_{\mathbf{l}s}$ or higher and yields, as we shall see, an analytically solvable description for many properties of the lattice; therefore our concern is with the second-order terms of (3.42).

The second-order terms are defined only for $(\mathbf{l}, s) \neq (\mathbf{l}', s')$. To define the on-diagonal, or self-interaction terms, we perform a rigid translation of the crystal, $u_{\mathbf{l}s\mu} = v_\nu \; \forall \, \mathbf{l}, s$. Clearly the resulting forces must be zero:

$$m_s \ddot{u}_{\mathbf{l}s\mu} = - \sum_{\nu} v_\nu \sum_{\mathbf{l}'s'} \Phi_{\mathbf{l}s\mu,\mathbf{l}'s'\nu} = 0 \; . \tag{3.45}$$

and so

$$\Phi_{\mathbf{l}s\mu,\mathbf{l}s\nu} = -\sum_{(\mathbf{l}',s')\neq(\mathbf{l},s)} \Phi_{\mathbf{l}s\mu,\mathbf{l}'s'\nu} \; . \tag{3.46}$$

The second-order coefficients are now well defined, and we have the equations of motion,

$$m_s \ddot{u}_{\mathbf{l}s\mu} = -\sum_{\mathbf{l}'s'\nu} \Phi_{\mathbf{l}s\mu,\mathbf{l}'s'\nu} u_{\mathbf{l}'s'\nu} \; . \tag{3.47}$$

We seek solutions of the form

$$u_{\mathbf{l}s\mu} \sim A_{s\mu}(\mathbf{k}) e^{i\mathbf{k}.\mathbf{l}} e^{i\omega t} \tag{3.48}$$

for wavevector k.

3.2.3 Dynamical matrix

Substitution of the trial solution (3.48) into the equation of motion (3.47) yields

$$-\omega^2 m_s A_{s\mu}(\mathbf{k}) + \sum_{\mathbf{l}'s'\nu} \Phi^{\mathbf{l}-\mathbf{l}'}_{s\mu,s'\nu} e^{-i\mathbf{k}.(\mathbf{l}-\mathbf{l}')} A_{s'\nu}(\mathbf{k}) = 0 \; . \tag{3.49}$$

The sum over lattice vectors may be performed in terms of $\mathbf{L} = \mathbf{l} - \mathbf{l}'$. Writing

$$\Phi_{s\mu,s'\nu}(\mathbf{k}) = \sum_{\mathbf{L}} \Phi^{\mathbf{L}}_{s\mu,s'\nu}(\mathbf{k}) e^{-i\mathbf{k}.\mathbf{L}} \tag{3.50}$$

we have the equation in matrix form

$$\mathbf{\Phi}_{\mathbf{k}} \mathbf{A}_{\mathbf{k}} = \omega^2 \mathbf{M} \mathbf{A}_{\mathbf{k}} \tag{3.51}$$

where $\mathbf{M} = \text{diag}(m_1, m_1, m_1, m_2, \ldots)$, and $\mathbf{\Phi}_{\mathbf{k}}$ and $\mathbf{A}_{\mathbf{k}}$ are the similarly constructed $3n \times 3n$ matrices with elements $\Phi_{s\mu,s'\nu}(\mathbf{k})$ and $A_{s\mu,s'\nu}(\mathbf{k})$ respectively. By writing $\mathbf{e}_{\mathbf{k}} = \mathbf{M}^{1/2}\mathbf{A}_{\mathbf{k}}$ and $\mathbf{D}_{\mathbf{k}} = \mathbf{M}^{-1/2}\mathbf{\Phi}_{\mathbf{k}}\mathbf{M}^{-1/2}$, we have the eigenvalue equation

$$\mathbf{D}_{\mathbf{k}} \mathbf{e}_{\mathbf{k}} = \omega^2 \mathbf{e}_{\mathbf{k}} \; . \tag{3.52}$$

$\mathbf{D}_{\mathbf{k}}$ is called the *dynamical matrix*, and has elements

$$D_{s\mu,s'\nu}(\mathbf{k}) = \frac{1}{\sqrt{m_s m_{s'}}} \sum_{\mathbf{L}} \Phi^{\mathbf{L}}_{s\mu,s'\nu}(\mathbf{k}) e^{-i\mathbf{k}.\mathbf{L}} \; . \tag{3.53}$$

$\mathbf{D}_\mathbf{k}$ is clearly Hermitian; therefore the eigenvectors $\mathbf{e}^{(j)}_\mathbf{k}$ form an orthonormal set. We also note that

$$\mathbf{D}_\mathbf{k} = \mathbf{D}^*_{-\mathbf{k}} \,, \tag{3.54}$$

so that the complex conjugate of (3.52) is

$$\left(\mathbf{D}^*_\mathbf{k} - \mathbf{1}.\omega^2_{\mathbf{k},j}\right)\mathbf{e}^{(j)*}_\mathbf{k} = \left(\mathbf{D}_{-\mathbf{k}} - \mathbf{1}.\omega^2_{\mathbf{k},j}\right)\mathbf{e}^{(j)*}_\mathbf{k} = 0 \,, \tag{3.55}$$

where j runs over eigenvalues and eigenvectors for a given k, i.e. over branches. Further,

$$\left(\mathbf{D}_{-\mathbf{k}} - \mathbf{1}.\omega^2_{-\mathbf{k},j}\right)\mathbf{e}^{(j)}_{-\mathbf{k}} = 0 \,, \tag{3.56}$$

whence

$$\begin{aligned} \omega_{-\mathbf{k},j} &= \omega_{\mathbf{k},j} \\ \mathbf{e}^{(j)}_{-\mathbf{k}} &= \mathbf{e}^{(j)*}_\mathbf{k} \,. \end{aligned} \tag{3.57}$$

The general solution of the equations of motion, written as a linear combination of elementary solutions (3.48) is

$$u_{\mathbf{l}s\mu}(t) = \sum_{\mathbf{k}j}\left(C_{\mathbf{k}j}\frac{e^{(j)}_{s\mu}(\mathbf{k})}{\sqrt{m_s}}e^{i\mathbf{k}.\mathbf{l}}e^{i\omega_{\mathbf{k}j}t} + C^*_{\mathbf{k}j}\frac{e^{(j)}_{s\mu}(\mathbf{k})^*}{\sqrt{m_s}}e^{-i\mathbf{k}.\mathbf{l}}e^{-i\omega_{\mathbf{k}j}t}\right) \,. \tag{3.58}$$

3.2.4 Fourier transform on a lattice

Before we can introduce normal coordinates, we must first define what is meant by a the Fourier transform of a function defined over a lattice. A function on an n-dimensional lattice is a map $f : \mathbb{Z}^n \to \mathbb{R} : \mathbf{l} \mapsto f_\mathbf{l} = F_{l_1,l_2,\ldots,l_3}$ where $\mathbf{l} = (l_1, l_2, \ldots, l_n)$ for $l_1, l_2, \ldots, l_n \in \mathbb{Z}$. Consider first a function f with period N on a one-dimensional lattice.

Proposition 1. *f_l may be written in terms of the discrete Fourier transform*

$$f_l = \frac{1}{\sqrt{N}}\sum_{j=1}^{N}\tilde{f}_j e^{i.2\pi jl/N} \tag{3.59}$$

with inverse

$$\tilde{f}_j = \frac{1}{\sqrt{N}}\sum_{l=1}^{N} f_l e^{-i.2\pi jl/N} \,. \tag{3.60}$$

Proof. Establish first that f has the correct periodicity.

$$\begin{aligned} f_{l+N} &= \frac{1}{\sqrt{N}} \sum_{j=1}^{N} \tilde{f}_j e^{i.2\pi j(l+N)/N} \\ &= \frac{1}{\sqrt{N}} \sum_{j=1}^{N} \tilde{f}_j e^{i.2\pi jl/N} e^{i.2\pi j} \\ &= \frac{1}{\sqrt{N}} \sum_{j=1}^{N} \tilde{f}_j e^{i.2\pi jl/N} = f_l \,. \end{aligned} \tag{3.61}$$

Next we check that the inverse transform of $\tilde{f}$ gives f.

$$\frac{1}{\sqrt{N}} \sum_{j=1}^{N} \tilde{f}_j e^{i.2\pi jl/N} = \sum_{l'=1}^{N} f_{l'} \left[\frac{1}{N} \sum_{j=1}^{N} e^{i.2\pi j(l-l')/N} \right] \,. \tag{3.62}$$

Write $\lambda = \exp[i.2\pi(l-l')/N]$. If $l = l'$ $\lambda = 1$. Now we consider $l \neq l'$; then

$$\frac{1}{N} \sum_{j=1}^{N} e^{i.2\pi j(l-l')/N} = \frac{1}{N} \sum_{j=1}^{N} \lambda^j = \frac{1}{N} \frac{\lambda(1-\lambda^N)}{1-\lambda} \tag{3.63}$$

for the sum of a geometric series. since $\lambda^N = \exp[i.2\pi(l-l') = 0$, we have

$$\frac{1}{N} \sum_{j=1}^{N} e^{i.2\pi j(l-l')/N} = \delta_{ll'} \tag{3.64}$$

and thus

$$\frac{1}{\sqrt{N}} \sum_{j=1}^{N} \tilde{f}_j e^{i.2\pi jl/N} = f_l \,. \tag{3.65}$$

□

Now we extend to a three-dimensional lattice. We consider a periodic function $F_{l_1+N_1,l_2,l_3} = F_{l_1,l_2,l_3} = f_{\mathbf{l}}$, taking $N = N_1 N_2 N_3$ values.

Proposition 2. *$f_{\mathbf{l}}$ may be written in terms of the discrete Fourier transform*

$$f_{\mathbf{l}} = \frac{1}{\sqrt{N}} \sum_{\forall \mathbf{k} \in BZ} \tilde{f}_{\mathbf{k}} e^{i\mathbf{k}.\mathbf{l}} \tag{3.66}$$

with inverse

$$\tilde{f}_{\mathbf{k}} = \frac{1}{\sqrt{N}} \sum_{\mathbf{l}} f_{\mathbf{l}} e^{-i\mathbf{k}.\mathbf{l}} \,. \tag{3.67}$$

Here BZ denotes the set of all points in the first Brillouin zone.

Proof. By performing discrete Fourier transforms with respect to the variables l_1, l_2 and l_3, one can write

$$f_{\mathbf{l}} = F_{l_1,l_2,l_3}$$
$$= \frac{1}{\sqrt{N_1 N_2 N_3}} \sum_{g_1=1}^{N_1} \sum_{g_2=1}^{N_2} \sum_{g_3=1}^{N_3} \tilde{F}_{g_1 g_2 g_3} e^{i.2\pi(g_1 l_1/N_1 + g_2 l_2/N_2 + g_3 l_3/N_3)} . \tag{3.68}$$

Now, for $\mathbf{k} \in BZ$

$$\mathbf{k}.\mathbf{l} = 2\pi(\frac{g_1}{N_1}, \frac{g_2}{N_2}, \frac{g_3}{N_3}).(l_1, l_2, l_3)$$
$$= 2\pi(g_1 l_1/N_1 + g_2 l_2/N_2 + g_3 l_3/N_3) , \tag{3.69}$$

therefore

$$f_{\mathbf{l}} \frac{1}{\sqrt{N}} \sum_{\forall \mathbf{k} \in BZ} \tilde{f}_{\mathbf{k}} e^{i\mathbf{k}.\mathbf{l}} \tag{3.70}$$

where $\tilde{f}_{\mathbf{k}} \equiv \tilde{F}_{g_1 g_2 g_3}$. The inverse transform can be similarly derived by considering one-dimensional inverse transforms of $\tilde{F}_{g_1 g_2 g_3}$ w.r.t. g_1, g_2 and g_3. □

3.2.5 Normal coordinates

The sum in equation (3.58) goes over all pairs of wavevectors $\mathbf{k}$, $-\mathbf{k}$, therefore we may express the second term as a sum over $\mathbf{k}' = -\mathbf{k}$. Then, introducing the complex normal coordinates

$$q_{\mathbf{k}j}(t) = \sqrt{N} \left(C_{\mathbf{k}j} e^{i\omega_{\mathbf{k}j} t} + C^*_{-\mathbf{k}j} e^{-i\omega_{\mathbf{k}j} t} \right) , \tag{3.71}$$

we have

$$u_{\mathbf{l}s\mu}(t) = \frac{1}{\sqrt{N m_s}} \sum_{\mathbf{k}j} q_{\mathbf{k}j}(t) e^{(j)}_{s\mu}(\mathbf{k}) e^{i\mathbf{k}.\mathbf{l}} . \tag{3.72}$$

Since the $q_{\mathbf{k}j}$ are complex, there appear to be $6N$ independent, real normal coordinates. From (3.71), however, we have

$$q_{-\mathbf{k}j} = q^*_{\mathbf{k}j} , \tag{3.73}$$

giving us the expected $3N$ real coordinates.

We recognize the sum in (3.72) as a discrete Fourier transform, and so applying the inverse, we have

$$\begin{aligned} \frac{1}{\sqrt{N}}\sum_{\mathbf{l}} u_{\mathbf{l}s\mu} e^{-i\mathbf{k}.\mathbf{l}} &= \frac{1}{\sqrt{n_s}}\sum_{j} q_{\mathbf{k}j}(t) e^{(j)}_{s\mu}(\mathbf{k}) \\ \Rightarrow \qquad \sum_{\mathbf{l}s\mu}\sqrt{\frac{m_s}{N}}\, u_{\mathbf{l}s\mu} e^{(j')*}_{s\mu} e^{-i\mathbf{k}.\mathbf{l}} &= \sum_{j} q_{\mathbf{k}j}(t) \sum_{s\mu} e^{(j)}_{s\mu} e^{(j')*}_{s\mu} \qquad (3.74) \\ &= q_{\mathbf{k}j'}(t)\ , \end{aligned}$$

by the orthogonality of the eigenvectors.

The expression (3.71) clearly shows that the $q_{\mathbf{k}j}$ satisfy the equations of motion for a set of independent harmonic oscillators

$$\ddot{q}_{\mathbf{k}j} + \omega^2_{\mathbf{k}j} q_{\mathbf{k}j} = 0\ . \qquad (3.75)$$

As discussed in sec. 3.2.1, the $\omega_{\mathbf{k}j}$ lead directly to the free energy by

$$F_{\text{vib}} = k_{\text{B}}T\sum_{\mathbf{k}j}\ln\frac{\hbar\omega_{\mathbf{k}j}}{k_{\text{B}}T}\ . \qquad (3.76)$$

To calculate the free energy in a harmonic lattice, it is therefore necessary first to calculate the elements of $\Phi_{\mathbf{l}s\mu,\mathbf{l}'s'\nu}$, secondly to calculate the dynamical matrix by a discrete Fourier transform, and finally to find the eigenvalues $\omega_{\mathbf{k}j}$. A discussion of how this has been achieved in practice will take place in ch. 6.

3.2.6 Quantum lattice corrections

If the physics of the ionic lattice cannot be described successfully using classical mechanics, one must adopt a quantum mechanical approach. Using PREM data [21], the Debye temperature of solid Fe at the inner core boundery is 620 K, which is well-below inner-core temperatures; hence non-classical lattice effects will not be relevant to inner-core physics. However, I report elastic results at a wide range of temperatures, down to zero. Whenever I do this, I will examine the possible size of quantum lattice corrections in the following way.

Quantum lattice corrections are most significant at low temperature. By demonstrating that a given set of measurements are unaffected by quantum lattice effects at zero temperature, I demonstrate that a classical description will be in general correctly describe those measurements. The zero temperature quantum lattice corrections to the energy are simply the energy of the zero-point vibrations of the lattice:

$$F_{\mathrm{ZP}} = \frac{1}{2} \sum_{\mathbf{k}j} \hbar\omega_{\mathbf{k}j}. \tag{3.77}$$

If at zero temperature the effect of making this correction to the energy of the lattice is small, then quantum lattice corrections can safely be regarded as negligible.

3.3 Molecular dynamics simulation

3.3.1 Thermodynamic motivation

Molecular dynamics (MD) is a powerful and general method of calculating thermodynamics functions for a system, while fully including the effect of anharmonic terms in the interatomic potential. It is also useful in cases such as fluids, where a Taylor expansion (3.42) of the potential is not meaningful. Whilst MD is therefore a very powerful and general technique in principle, it is comparatively expensive in terms of computational resources, compared with harmonic theory.

The idea of molecular dynamics, is that the properties of a system of atoms in correlated motion, are simulated by numerically integrating the equations of motion of the atoms. If these trajectories densely cover the constant-energy surface (an assumption known as the ergodic hypothesis), then in the limit of very long simulations, the time-averaged values of thermodynamic variables such as the pressure will equal their ensemble-averaged values.

3.3.2 Equations of motion

Given a Hamiltonian function $H(\mathbf{R}_1 \ldots \mathbf{R}_N, \mathbf{p}_1 \ldots \mathbf{p}_N)$, we have the equations of motion

$$\begin{aligned} \frac{\partial \mathbf{p}_i}{\partial t} &= -\frac{\partial H}{\partial \mathbf{R}_i} \\ \frac{\partial \mathbf{R}_i}{\partial t} &= \frac{\partial H}{\partial \mathbf{p}_i} \,. \end{aligned} \tag{3.78}$$

By specifying initial values of the $\mathbf{R}_i$ and $\mathbf{p}_i$, one can numerically integrate (3.78) to give a phase-space trajectory $\Gamma(t)$. A popular method, and one employed throughout these MD calculations is the *velocity Verlet algorithm* (VVA) [4].

We begin by performing a Taylor expansion of the positions $\mathbf{r}$ about a time t:

$$\begin{aligned} \mathbf{r}(t+\delta t) &= \mathbf{r}(t) + \mathbf{v}(t)\delta t + \frac{1}{2}\mathbf{a}(t)\delta t^2 \\ \mathbf{r}(t-\delta t) &= \mathbf{r}(t) - \mathbf{v}(t)\delta t + \frac{1}{2}\mathbf{a}(t)\delta t^2 \,. \end{aligned} \tag{3.79}$$

Eliminating $\mathbf{v}(t)$, we have

$$\mathbf{r}(t+\delta t) = 2\mathbf{r}(t) + \mathbf{a}(t)\delta t^2 - \mathbf{r}(t-\delta t). \tag{3.80}$$

This is the standard Verlet algorithm (VA). The velocities are not required to calculate the trajectories, but they can be calculated using

$$\mathbf{v}(t) = \frac{\mathbf{r}(t+\delta t) - \mathbf{r}(t-\delta t)}{2\delta t} \,. \tag{3.81}$$

Equation (3.80) is correct except for errors of order δt^4; however the velocities of (3.81) contain errors of order δt^2. An approach which produces identical trajectories, is the velocity Verlet algorithm, used in this work:

$$\mathbf{r}(t+\delta t) = \mathbf{r}(t) + \delta t\mathbf{v}(t) + \frac{1}{2}\delta t^2\mathbf{a}(t) \tag{3.82}$$

$$\mathbf{v}(t+\delta t) = \mathbf{v}(t) + \frac{1}{2}\delta t[\mathbf{a}(t) + \mathbf{a}(t+\delta t)] \,. \tag{3.83}$$

By forming the corresponding expressions for $r(t)$ and $v(t)$, and substituting them into (3.82), it is straightforward to see that the VVA and the VA produce identical trajectories.

3.3.3 Instantaneous variables

To calculate a particular time average, it is necessary to define an instantaneous thermodynamic variable, which we can then average over the length of the trajectory. Here we consider the pressure. The first law of thermodynamics states that

$$\mathrm{d}U = T\mathrm{d}S - p\mathrm{d}V \,, \tag{3.84}$$

Writing the Helmholtz free energy as $F = U - TS$, we have

$$\begin{aligned} \mathrm{d}F &= \mathrm{d}U - T\mathrm{d}S - S\mathrm{d}T \\ &= -p\mathrm{d}V - S\mathrm{d}T \,, \end{aligned} \tag{3.85}$$

whence

$$p = -\left(\frac{\partial F}{\partial V}\right)_T \,. \tag{3.86}$$

Consider now a cubic cell of side L. The free energy F is given by

$$F = -k_\mathrm{B} T \ln\left\{\frac{1}{\Lambda^{3N}} \int \mathrm{d}^{3N}\mathbf{R} e^{-\beta U(\mathbf{R}_1 \ldots \mathbf{R}_N)}\right\} \,. \tag{3.87}$$

Making a change of variables $\mathbf{R} = L\mathbf{X}$, we have

$$F = -k_\mathrm{B} T \ln\left\{\frac{V^N}{\Lambda^{3N}} \int \mathrm{d}^{3N}\mathbf{X} e^{-\beta U(L\mathbf{X}_1 \ldots L\mathbf{X}_N)}\right\} \,; \tag{3.88}$$

therefore

$$\begin{aligned} p &= -\left(\frac{\partial F}{\partial V}\right)_T \\ &= k_\mathrm{B} T \left\{\left(\frac{V}{\Lambda^3}\right)^N \int \mathrm{d}^{3N}\mathbf{X} e^{-\beta U}\right\}^{-1} \times \ldots \\ &\quad \left(\frac{V}{\Lambda^3}\right)^N \int \left\{\frac{N}{V} + (-\beta)\left(\frac{\partial U}{\partial V}\right)_T\right\} e^{-\beta U} \mathrm{d}^{3N}\mathbf{X} \\ &= \frac{N k_\mathrm{B} T}{V} - \left\langle \left(\frac{\partial U}{\partial V}\right)_T \right\rangle \,. \end{aligned} \tag{3.89}$$

We now have the pressure p expressed as an ensemble average of the derivative of the potential energy U. Using the Hellmann-Feynman theorem (and Pulay corrections where necessary) in *ab initio* techniques, or expressions for the derivatives of an empirical potential in classical techniques, it is possible to compute $\partial U/\partial V$ for a given atomic configuration. We can therefore define an instantaneous pressure,

$$\mathcal{P}(\mathbf{R}_1 \ldots \mathbf{R}_N) \equiv \frac{Nk_\mathrm{B}T}{V} - \frac{\partial}{\partial V}U(\mathbf{R}_1 \ldots \mathbf{R}_N) \; , \tag{3.90}$$

such that the true pressure is given by the ensemble average

$$p = \langle \mathcal{P} \rangle \; . \tag{3.91}$$

In density functional theory, for example, the quantity $\partial U/\partial V$ can be computed by an analogue of the Hellmann-Feynman theorem (see Ch. 2 for a discussion of the Hellmann-Feynman theorem for forces), which tells us that

$$\frac{\partial}{\partial V} \langle \Psi \,|\, H \,|\, \Psi \rangle = \left\langle \Psi \left| \frac{\partial H}{\partial V} \right| \Psi \right\rangle \; . \tag{3.92}$$

In analogy with the Hellmann-Feynman theorem for forces, there will be Pulay-like corrections in a finite basis which depends explicitly on V, such as plane waves.

3.3.4 The ergodic hypothesis

As stated already, molecular dynamics does not permit us directly to perform an ensemble average of thermodynamic functions; however Liouville's theorem guarantees that under certain conditions (ergodic), time-averaging and ensemble averaging will be equivalent [58]. The ergodic hypothesis itself consists in asserting that a given phase-space trajectory of a system densely covers the constant-energy surface in phase space. While this is true for a very wide range of systems, it is instructive to note the effect of the ergodic hypothesis not holding.

In the harmonic approximation, normal modes obey an equation of motion

$$\ddot{q}_{\mathbf{k}j} + \omega_{\mathbf{k}j}^2 q_{\mathbf{k}j} = 0 \; . \tag{3.93}$$

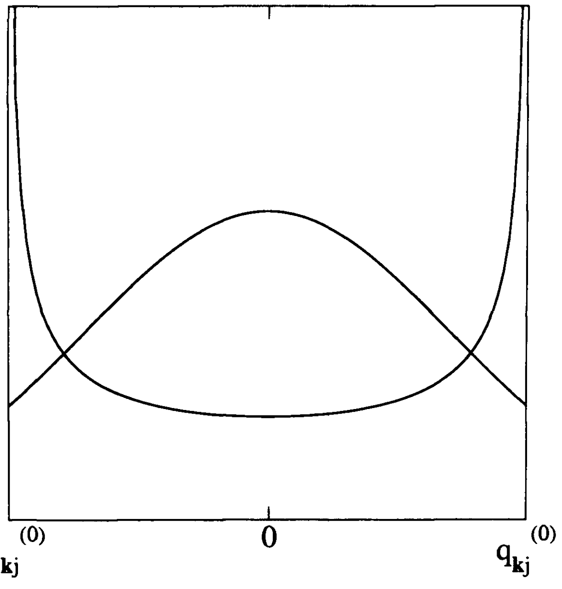

Figure 3.2: Probability distribution for a normal mode in a harmonic lattice. The bimodal curve represents time averaging, while the bell curve represents ensemble averaging.

It is immediately apparent, that energy cannot be transferred between normal modes of a harmonic lattice, and that therefore the constant-energy surface in phase space at a given total energy H is not densely covered. What effect does this have on the difference between time and ensemble averaging? If we were to perform an MD simulation of a crystal, and study the probability distribution of a normal mode such as $q_{\mathbf{k}j}$, we find that

$$\begin{aligned} P(q_{\mathbf{k}j}) &\propto \left|\frac{1}{\dot{q}_{\mathbf{k}j}}\right| \\ &\propto \frac{1}{\omega\sqrt{\left(q_{\mathbf{k}j}^{(0)}\right)^2 - q_{\mathbf{k}j}^2}}\,, \end{aligned} \qquad (3.94)$$

which has the bimodal form shown in fig. 3.2. If however, one applies a Boltzmann distribution to the possible values of $q_{\mathbf{k}j}$, the result is very different.

$$\begin{aligned} P(q_{\mathbf{k}j}) &\propto \exp\left[-\beta U(q_{\mathbf{k}j})\right] \\ &\propto \exp\left[-\frac{1}{2}\beta m\omega^2 q_{\mathbf{k}j}^2\right] . \end{aligned} \tag{3.95}$$

This bell curve is also shown in fig. 3.2. We see that the probability distribution for a normal mode of a harmonic system is very differently predicted by time and ensemble averaging, because of the non-ergodicity of the harmonic lattice.

A system of particles with an anharmonic potential coupling is not describable in terms of completely separable components. This means that one cannot in general describe a normal coordinate, which will conserve energy, and be thus restricted to a particular region of phase-space in the sense described above; therefore in an anharmonic system there is no such barrier to a trajectory densely covering phase space and therefore violating the ergodic hypothesis.

3.3.5 Ensembles

Accepting the ergodic hypothesis, then, the time-averaged values of instantaneous thermodynamic variables in a constant energy simulation, should correctly predict the same thermodynamic variables in a microcanonical ensemble average. Frequently, however, we are interested in a system at constant temperature, free to exchange energy with its environment. We therefore require a way of allowing energy to enter and leave our simulation. A *thermostat* is a mechanism designed to do this; there are a number practical thermostats available, and the one described here is due to Andersen.

Andersen [59] proves that under quite general conditions, it is possible to produce (N, V, T) ensemble averages from the time-averaged quantities in a molecular dynamics simulation using the following method, based on stochastic collisions. Firstly, two parameters are chosen: a temperature T, and a collision rate, ν. For every particle in the system, a set of collision times is generated in advance, using the following distribution of time intervals t

$$P(t) = \nu \exp[-\nu t] \,. \tag{3.96}$$

At each collision time, the particle is given a momentum chosen at random from a Boltzmann distribution at temperature T:

$$P(\mathbf{p}) \propto \exp[-p^2/2mk_\mathrm{B}T] \,. \tag{3.97}$$

The collision rate ν will not affect the ultimate value of thermodynamic variables calculated in this way, but should be viewed as a parameter affecting optimization; a statistically meaningful average requires that ν^{-1} be small with respect to the length of simulation.

3.3.6 Thermodynamic integration and free energy

Throughout Ch. 5, comparisons are made between my results and the *ab initio* calculations of many thermodynamic quantities of inner-core iron made by [34], and these results are regarded as being accurate, anharmonic *ab initio* results, free from uncontrolled errors. The results in question are based on free energy calculations, and given their importance to this work, it is appropriate here to discuss the theory behind these calculations.

The free energy is a difficult quantity to calculate in molecular dynamics, as there is no corresponding instantaneous variable to be averaged. Given a reference system of known free energy F_0, however, the free energy F_1 of an *ab initio* system can be calculated using the method of *thermodynamic integration* [58].

Suppose the many-body potential energy functions of our reference and *ab initio* systems are $U_0(\mathbf{R}_1, \ldots, \mathbf{R}_N)$ and $U_1(\mathbf{R}_1, \ldots, \mathbf{R}_N)$ respectively. We may define the λ-family of systems having potential energy functions

$$U_\lambda(\mathbf{R}_1, \ldots, \mathbf{R}_N) \equiv (1-\lambda)U_0(\mathbf{R}_1, \ldots, \mathbf{R}_N) + \lambda U_1(\mathbf{R}_1, \ldots, \mathbf{R}_N) \,. \tag{3.98}$$

Each such system having a partition function

$$Z_\lambda(N,V,T) = \frac{1}{N!\Lambda^{3N}} \int \mathrm{d}^{3N}\mathbf{R} e^{-\beta U_\lambda(\mathbf{R}_1,\ldots,\mathbf{R}_N)} \tag{3.99}$$

and a free energy

$$F_\lambda(N,V,T) = -k_\mathrm{B}T \ln\left[\frac{1}{N!\Lambda^{3N}} \int \mathrm{d}^{3N}\mathbf{R} e^{-\beta U_\lambda(\mathbf{R}_1,\ldots,\mathbf{R}_N)}\right] . \tag{3.100}$$

Using this family of systems, one can define the derivative

$$\begin{aligned}
\left(\frac{\partial F_\lambda}{\partial \lambda}\right)_{N,V,T} &= -k_\mathrm{B}T \frac{1}{Z_\lambda(N,V,T)} \left(\frac{\partial Z_\lambda(N,V,T)}{\partial \lambda}\right)_{N,V,T} \\
&= \frac{\int \mathrm{d}^{3N}\mathbf{R}(\partial U_\lambda(\mathbf{R}_1,\ldots,\mathbf{R}_N)/\partial\lambda)\exp[-\beta U_\lambda(\mathbf{R}_1,\ldots,\mathbf{R}_N)]}{\int \mathrm{d}^{3N}\mathbf{R}\exp[-\beta U_\lambda(\mathbf{R}_1,\ldots,\mathbf{R}_N)]} \\
&= \left\langle \frac{\partial U_\lambda(N,V,T)}{\partial \lambda} \right\rangle_\lambda \\
&= \langle U_1(N,V,T) - U_0(N,V,T)\rangle_\lambda \ ,
\end{aligned} \tag{3.101}$$

where $\langle\rangle_\lambda$ denotes an average in the λ ensemble. As this is a thermodynamic average, it can be directly calculated using molecular dynamics, where the force on the i^{th} atom in the λ ensemble in a given configuration is

$$f^{(i)}_\lambda(\mathbf{R}_1,\ldots,\mathbf{R}_N) = (1-\lambda) f^{(i)}_0(\mathbf{R}_1,\ldots,\mathbf{R}_N) - \lambda f^{(i)}_1(\mathbf{R}_1,\ldots,\mathbf{R}_N) \ . \tag{3.102}$$

The free energy of the *ab initio* system is then (independently of the reference system)

$$\begin{aligned}
F_1(N,V,T) &= F_0(N,V,T) + \int_0^1 \mathrm{d}\lambda \left(\frac{\partial F_\lambda}{\partial \lambda}\right)_{N,V,T} \\
&= F_0(N,V,T) + \int_0^1 \mathrm{d}\lambda \, \langle U_1(N,V,T) - U_0(N,V,T)\rangle_\lambda \ .
\end{aligned} \tag{3.103}$$

Therefore, given a known $F_0(N,V,T)$, one may perform a set of molecular dynamics simulations for different values of the parameter λ (that is, trajectories evolved by the forces $\{f^{(i)}_\lambda\}$), and form the integral (3.103).

3.4 The particle-in-cell approximation

3.4.1 Principles

The particle-in-cell (PIC) approximation [3, 60, 61, 62, 63, 64] is one of any number of methods which seek to include the effects of anharmonicity in a less computationally intensive framework than molecular dynamics. It is a mean field method, and we begin our consideration with the partition function of a classical system of distinguishable particles in thermal contact with its environment

$$\begin{aligned} Z(N,V,T) &= \frac{1}{\Lambda^{3N}} \int \mathrm{d}^{3N}\mathbf{R} e^{-\beta U(\mathbf{R}_1,\ldots,\mathbf{R}_N)} \\ &= \frac{1}{\Lambda^{3N}} e^{-\beta F_{\text{perf}}} \int \mathrm{d}^{3N}\mathbf{R} e^{-\beta \Phi(\mathbf{R}_1,\ldots,\mathbf{R}_N)} , \end{aligned} \tag{3.104}$$

where $U(\mathbf{R}_1,\ldots,\mathbf{R}_N) = F_{\text{perf}} + \Phi(\mathbf{R}_1,\ldots,\mathbf{R}_N)$ is the potential energy of the particles, including the perfect lattice term $F_{\text{perf}} = U(\mathbf{R}_1^0,\ldots,\mathbf{R}_N^0)$. Denote

$$Z_{\text{perf}}(N,V,T) = \frac{1}{\Lambda^{3N}} e^{-\beta F_{\text{perf}}} \tag{3.105}$$

and

$$Z_{\text{vib}}(N,V,T) = \int \mathrm{d}^{3N}\mathbf{R} e^{-\beta \Phi(\mathbf{R}_1,\ldots,\mathbf{R}_N)} . \tag{3.106}$$

An integral such as (3.106), in 3N variables, cannot be calculated directly by numerical quadrature, which is why there exist such indirect methods as molecular dynamics and Monte Carlo simulation, and the harmonic approximation, which renders an analytic solution to an approximation of the problem.

An alternative to the above techniques, however, is to make approximations which will allow (3.106) to be evaluated more easily. The essential purpose of mean field techniques, is to reduce the effective dimensionality of the integral, and the PIC method is such a technique. The PIC method proceeds by eliminating the effects of interatomic correlations. There is no particular argument to support the assumption that such correlations are negligible, so no attempt will be made to support this further, except to refer the reader to the several studies which have shown empirical support for the PIC model in certain systems [60, 61, 62, 63].

We neglect correlation by assuming that the potential Φ can be separated into terms for each atom

$$\Phi(\mathbf{R}_1, \ldots, \mathbf{R}_N) = \phi_1(\mathbf{R}_1) + \ldots + \phi_N(\mathbf{R}_N) \, . \tag{3.107}$$

There is clearly no one way to decide upon the form of the functions $\phi_i(\mathbf{R}_\mathrm{i})$, but the PIC model defines

$$\phi_i(\mathbf{R}_i) \equiv \Phi(\mathbf{R}_1^0, \ldots, \mathbf{R}_i, \ldots, \mathbf{R}_N^0) \, , \tag{3.108}$$

where $\mathbf{R}_i$ is restricted to the Wigner-Sietz cell containing atom i. In the h.c.p. structure, all atoms are equivalent under the point symmetry operations of the lattice; therefore all ϕs are equal, and the result is

$$\begin{aligned} Z_{\mathrm{vib}}^{\mathrm{PIC}}(N, V, T) &= \int \mathrm{d}^{3N}\mathbf{R} e^{-\beta\Phi(\mathbf{R}_1, \ldots, \mathbf{R}_N)} \\ &= \int \mathrm{d}^{3N}\mathbf{R} e^{-\beta[\phi(\mathbf{R}_1) + \ldots + \phi(\mathbf{R}_N)]} \\ &= \left[\int \mathrm{d}^3\mathbf{R} e^{-\beta\phi(\mathbf{R})} \right]^N \, . \end{aligned} \tag{3.109}$$

Here all integrals go over the Wigner-Sietz cell of the atom in question. This gives a free energy of

$$\begin{aligned} F_{\mathrm{vib}}^{\mathrm{PIC}} &= -k_{\mathrm{B}} T \ln Z_{\mathrm{vib}} \\ &= -N k_{\mathrm{B}} T \ln \int \mathrm{d}^3\mathbf{R} e^{-\beta\phi(\mathbf{R})} \\ &= N f_{\mathrm{vib}}^{\mathrm{PIC}} \, , \end{aligned} \tag{3.110}$$

where $f_{\mathrm{vib}}^{\mathrm{PIC}}$ is the vibrational contribution per atom to the free energy in the PIC model.

In principle, therefore, $F_{\mathrm{vib}}^{\mathrm{PIC}}$ is calculated by forming a parameterized potential $\phi(\mathbf{R})$ over the Wigner-Sietz cell of an "wanderer" atom, being the increased energy of the lattice when the wanderer is at $\mathbf{R}$, and the

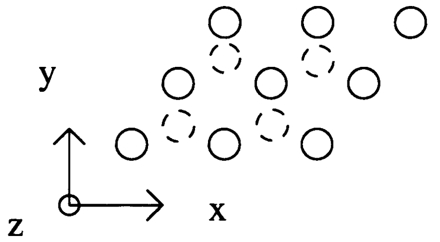

Figure 3.3: hcp lattice showing x, y and z axes.

remaining atoms are on their equilibrium lattice sites. In practice, we must use a supercell geometry, and systematically increase the periodicity of the superlattice until $\phi(\mathbf{r})$ becomes consistent. For an $l \times m \times n$ supercell,

$$\phi_{lmn}(\mathbf{r}) = U_{lmn}(\mathbf{R}_1^0, \ldots, \mathbf{R}_i, \ldots, \mathbf{R}_N^0) - U_{lmn}(\mathbf{R}_1^0, \ldots, \mathbf{R}_i^0, \ldots, \mathbf{R}_N^0)\ . \tag{3.111}$$

and $\phi(\mathbf{r}) = \lim_{l,m,n\to\infty} \phi_{lmn}\{(\mathbf{r})\}$.

This leaves the question of the representation of $\phi(\mathbf{R})$. Since $\phi(\mathbf{R})$ is a short-ranged function, I write it as a Taylor expansion. Note that $Z_{\text{vib}}^{\text{PIC}}$ is dominated by the small-ϕ centre of the Wigner-Sietz cell. By definition, $\phi(0) = 0$, and the forces disappear at equilibrium meaning $\phi'(0) = 0$. This means I require a polynomial in $\mathbf{R}$, zeroth- and first-order terms zero. The principal simplifying observation I use is that $\phi(\mathbf{R})$ must satisfy the point-group symmetries of the lattice.

3.4.2 The particle in cell model for the h.c.p. lattice

I now consider the particular form of the cell potential for the hcp lattice, as I will be particularly concerned with hcp Fe here. This section represents original work by the author. The hcp lattice, with the x, y and z axes labelled, is shown in Fig. 3.3 The generators of the h.c.p. symmetries are: reflection in the x-y plane, reflection in the y-z plane, and rotation of $2\pi/3$ about the z-axis. These operations can be represented by, respectively, matrices $M_{x\text{-}y}$, $M_{y\text{-}z}$ and $M_{2\pi/3}$ s.t. $\mathbf{R} \mapsto \mathbf{R}' = M\mathbf{R}$. These matrices may be written:

$$
\begin{aligned}
M_{x\text{-}y} &= \begin{pmatrix} 1 & 0 & 0 \\ 0 & 1 & 0 \\ 0 & 0 & -1 \end{pmatrix} , \\
M_{y\text{-}z} &= \begin{pmatrix} -1 & 0 & 0 \\ 0 & 1 & 0 \\ 0 & 0 & 1 \end{pmatrix} , \\
M_{2\pi/3} &= \begin{pmatrix} -\frac{1}{2} & \frac{\sqrt{3}}{2} & 0 \\ -\frac{\sqrt{3}}{2} & -\frac{1}{2} & 0 \\ 0 & 0 & 1 \end{pmatrix} .
\end{aligned}
\qquad (3.112)
$$

For a function $\phi(\mathbf{R})$ to be said to be invariant under a group of symmetries, it is sufficient that $\phi(\mathbf{R})$ be invariant under the action of all the generators $M : \phi(\mathbf{R}) \mapsto \phi'(\mathbf{R}) = \phi(M^{-1}\mathbf{R})$. Obviously, $M^{-1}_{x\text{-}y} = M_{x\text{-}y}$ and $M^{-1}_{y\text{-}z} = M_{y\text{-}z}$, while

$$
M_{2\pi/3} = M^2_{2\pi/3} = \begin{pmatrix} -\frac{1}{2} & -\frac{\sqrt{3}}{2} & 0 \\ \frac{\sqrt{3}}{2} & -\frac{1}{2} & 0 \\ 0 & 0 & 1 \end{pmatrix} . \qquad (3.113)
$$

I represent $\phi(\mathbf{R})$ by a polynomial expansion. Taking each order in turn, I calculate and equate $\phi(\mathbf{R})$ and $\phi'(\mathbf{R})$. By equating corresponding coefficients, we are able to express $\phi(\mathbf{R})$ quite generally using a few invariant terms. This is done here explicitly for all orders $n \leq 4$. To facilitate this I adopt the following notation:

$$
\phi(\mathbf{R}) = C_\alpha r_\alpha + C_{\alpha\beta} r_\alpha r_\beta + C_{\alpha\beta\gamma} r_\alpha r_\beta r_\gamma + C_{\alpha\beta\gamma\delta} r_\alpha r_\beta r_\gamma r_\delta + \cdots , \qquad (3.114)
$$

where $\alpha \leq \beta \leq \gamma \leq \delta$ are summed where repeated, over the three Cartesian coordinates axes.

First order. No terms of first order are symmetric under the three M matrices. That terms in x and z vanish is obvious:

$$C_x x = C_x x' = -C_x x \tag{3.115}$$

$$\Rightarrow C_x = 0 \tag{3.116}$$

and similarly for C_z. For C_y, we need $M_{2\pi/3}$:

$$\begin{aligned} C_x x + C_y y &= C_x x' + C_y y' \\ &= \frac{1}{2}\left[-C_x\,(x+\sqrt{3}y) + C_y\,(\sqrt{3}x - y)\right] , \\ \text{thus}\quad C_x &= -\frac{1}{2}(C_x - \sqrt{3}C_y) \qquad \Rightarrow \qquad C_y = \sqrt{3}C_x \\ \text{and}\quad C_y &= -\frac{1}{2}(\sqrt{3}C_x + C_y) \qquad \Rightarrow \qquad C_x = -\sqrt{3}C_y \\ \text{and so}\quad C_y &= -C_y = 0 \, . \end{aligned} \tag{3.117}$$

Before going further, we note that only the *whole* function $\phi(\mathbf{R})$ is invariant under the cell symmetries. In the preceding, I treated the action of $M_{x\text{-}y}$ on $C_z z$ and $M_{y\text{-}z}$ on $C_x x$ separately, but treated the behaviour of $M_{2\pi/3}$ on the sum $C_x x + C_y y$. In general, I can treat separately any variable or group of variables which is not mixed with any others under the action of the matrix in question. It is also perfectly permissible to treat separately terms of different order.

Second order. All cross terms (terms in xy, xz or yz) vanish, as they contain only single powers of y. The z^2 term is not mixed with any other under the action of any matrix, so exists independently. We consider sum of the remaining terms under the action of $M_{2\pi/3}$:

$$\begin{aligned}
C_{x^2}x^2 + C_{y^2}y^2 &= C_{x^2}x'^2 + C_{y^2}y'^2 && (3.118)\\
&= \frac{1}{4}[C_{x^2}(x+\sqrt{3}y)^2 + C_{y^2}(\sqrt{3}x-y)^2] && (3.119)\\
&= \frac{1}{4}[x^2(C_{x^2}+3C_{y^2}) + 2\sqrt{3}xy(C_{x^2}+3C_{y^2}) && (3.120)\\
&\quad +y^2(3C_{x^2}+C_{y^2})] && (3.121)\\
\Rightarrow \quad C_{x^2} &= C_{y^2}\ . && (3.122)
\end{aligned}$$

Third order. Terms not eliminated by $M_{x\text{-}y}$ and $M_{y\text{-}z}$ are those in x^2y, y^3 and yz^2. $C_{yz^2} = 0$ by the argument of (3.117). Under the action of $M_{2\pi/3}$

$$\begin{aligned}
C_{x^2y}x^2y + C_{y^3}y^3 &= C_{x^2y}x'^2y' + C_{y^3}y'^3\\
&= \tfrac{1}{8}[\sqrt{3}x^3(C_{x^2y}\\
&\quad +3C_{y^3}) + x^2y(5C_{x^2y} - 9C_{y^3})\\
&\quad +\sqrt{3}xy^2(C_{x^2y}+3C_{y^3})\\
&\quad +y^3(-3Cx^2y - Cy^3)]\\
\Rightarrow \quad C_{x^2y} &= -3C_{y^3}\ .
\end{aligned} \qquad (3.123)$$

Fourth order. Terms not eliminated by $M_{x\text{-}y}$ and $M_{y\text{-}z}$ are those in x^4, y^4, z^4, x^2y^2, x^2z^2 and y^2z^2. z^4 is independent. As z is not mixed with x and y under the action of $M_{2\pi/3}$, we first consider

$$\begin{aligned}
C_{x^4}x^4 + C_{x^2y^2}x^2y^2 + C_{y^4}y^4 &= C_{x^4}x'^4 + C_{x^2y^2}x'^2y'^2 + C_{y^4}y'^4\\
&= \tfrac{1}{16}[C_{x^4}(x+\sqrt{3}y)^4\\
&\quad +C_{x^2y^2}(x+\sqrt{3}y)^2(\sqrt{3}x-y)^2\\
&\quad +Cy^4(\sqrt{3}x-y)^4]\\
&= \tfrac{1}{16}[x^4(C_{x^4}+3C_{x^2y^2}+9C_{y^4})\\
&\quad +y^4(9C_{x^4}+3C_{x^2y^2}+C_{y^4})\\
&\quad +\text{ other terms}]\\
\text{thus} \quad 16C_{x^4} &= C_{x^4}+3C_{x^2y^2}+9C_{y^4}\\
\text{and} \quad 16C_{y^4} &= 9C_{x^4}+3C_{x^2y^2}+C_{y^4}\\
\Rightarrow \quad C_{x^2y^2} &= 2C_{x^4} = 2C_{y^4}\ .
\end{aligned} \qquad (3.124)$$

Lastly, it should be clear from our second-order analysis, that $C_{x^2z^2} = C_{y^2z^2}$.

To fourth order, therefore, our potential looks like

$$\begin{aligned}\phi(\mathbf{R}) =& K_a^{(2)}(x^2+y^2) + K_b^{(2)}z^2 + K^{(3)}(y^3 - 3x^2y) \\ &+ K_a^{(4)}(x^2+y^2)^2 + K_b^{(4)}(x^2+y^2)z^2 + K_c^{(4)}z^4 \,.\end{aligned} \tag{3.125}$$

3.4.3 The harmonic limit in PIC

It will become important later to study the separate contributions to the free energy of the harmonic and anharmonic components of this potential. We define the harmonic potential

$$\begin{aligned}\phi_{\mathrm{h}}(\mathbf{R}) &\equiv K_a^{(2)}(x^2+y^2) + K_b^{(2)}z^2 \\ &\equiv \frac{1}{2}M\omega_a^2(x^2+y^2) + \frac{1}{2}M\omega_b^2 z^2 \,,\end{aligned} \tag{3.126}$$

and the anharmonic potential

$$\begin{aligned}\phi_{\mathrm{ah}}(\mathbf{R}) &\equiv \phi(\mathbf{R}) - \phi_{\mathrm{h}}(\mathbf{R}) \\ &= K^{(3)}(y^3 - 3x^2y) + K_a^{(4)}(x^2+y^2)^2 + K_b^{(4)}(x^2+y^2)z^2 + K_c^{(4)}z^4\end{aligned} \tag{3.127}$$

to fourth order. With these definitions, the PIC free energy per atom in the harmonic limit is given by

$$\begin{aligned}f_{\mathrm{h}}^{\mathrm{PIC}} &\equiv -k_{\mathrm{B}}T\ln\left\{\int \mathrm{d}^3\mathbf{R}e^{-\beta\phi_{\mathrm{h}}(\mathbf{R})}\right\} \\ &= k_{\mathrm{B}}T\left[2\ln\frac{\hbar\omega_a}{k_{\mathrm{B}}T} + \ln\frac{\hbar\omega_b}{k_{\mathrm{B}}T}\right] \\ &= 3k_{\mathrm{B}}T\ln\frac{\hbar\bar{\omega}}{k_{\mathrm{B}}T} \,,\end{aligned} \tag{3.128}$$

where we have defined the logarithmic mean frequency

$$\ln\bar{\omega} = \frac{1}{3}(2\ln\omega_a + \ln\omega_b) \tag{3.129}$$

or

$$\bar{\omega} = \left(\omega_a^2\omega_b\right)^{1/3} \,. \tag{3.130}$$

3.4.4 Anharmonicity

The anharmonic free energy is defined to be

$$\begin{aligned} f_{\mathrm{ah}}^{\mathrm{PIC}} &\equiv f_{\mathrm{vib}}^{\mathrm{PIC}} - f_{\mathrm{h}}^{\mathrm{PIC}} \\ &= -k_{\mathrm{B}}T \ln \left\{ \frac{\int \mathrm{d}^3\mathbf{R} e^{-\beta\phi_{\mathrm{h}}(\mathbf{R})} e^{-\beta\phi_{\mathrm{ah}}(\mathbf{R})}}{\int \mathrm{d}^3\mathbf{R} e^{-\beta\phi_{\mathrm{h}}(\mathbf{R})}} \right\} \\ &= -k_{\mathrm{B}}T \ln \left\langle e^{-\beta\phi_{\mathrm{ah}}(\mathbf{R})} \right\rangle_{\mathrm{h}} \end{aligned} \tag{3.131}$$

where $\langle\rangle_{\mathrm{h}}$ denotes an expectation value in the ensemble described by $\phi_{\mathrm{h}}(\mathbf{R})$. We can expand both the logarithm and the exponential here in powers of temperature. In order to get the order of expansion under control, we first evaluate the terms $\langle\phi_{\mathrm{ah}}^n\rangle_{\mathrm{h}}$. In what follows, we plan to keep only terms of order T^2. A general result, obtained by parametric differentiation of the Gaussian integral

$$\int_{-\infty}^{\infty} e^{-\alpha x^2} \mathrm{d}x = \sqrt{\frac{\pi}{\alpha}} \tag{3.132}$$

is

$$\int_{-\infty}^{\infty} x^{2n} e^{-\alpha x^2} \mathrm{d}x = \left(n - \frac{1}{2}\right)\left(n - \frac{3}{2}\right) \cdots \frac{3}{2}\frac{1}{2}\sqrt{\frac{\pi}{\alpha^{2n+1}}}\,, \tag{3.133}$$

while

$$\int_{-\infty}^{\infty} x^{2n+1} e^{-\alpha x^2} \mathrm{d}x = 0\,. \tag{3.134}$$

We need terms of the following form, where we for generality write ω_x, ω_y and ω_z in place of ω_a and ω_b:

$$\begin{aligned} \langle x^4 \rangle_{\mathrm{h}} &= \left[\int \mathrm{d}^3\mathbf{R} x^4 e^{-\beta\phi_{\mathrm{h}}(\mathbf{R})}\right] \left[\int \mathrm{d}^3\mathbf{R} e^{-\beta\phi_{\mathrm{h}}(\mathbf{R})}\right]^{-1} \\ &= \frac{3}{\beta^2 M^2 \omega_x^4}\,; \end{aligned} \tag{3.135}$$

$$\langle x^2 y^2 \rangle_{\mathrm{h}} = \frac{1}{\beta^2 M^2 \omega_x^2 \omega_y^2}\,; \tag{3.136}$$

$$\langle x^6 \rangle_{\mathrm{h}} = \frac{3}{\beta^3 M^3 \omega_x^2 \omega_y^4}\,; \tag{3.137}$$

$$\langle x^2 y^4 \rangle_{\mathrm{h}} = \frac{15}{\beta^3 M^3 \omega_y^6}\,. \tag{3.138}$$

Using these results, we obtain

$$\begin{aligned}\langle\phi_{\text{ah}}\rangle_{\text{h}} &= K_a^{(4)}\left\langle x^4+y^4+2x^2y^2\right\rangle \\ &\quad + K_b^{(4)}\left\langle x^2z^2+y^2z^2\right\rangle + K_c^{(4)}\left\langle z^4\right\rangle \\ &= \frac{1}{\beta^2M^2}\left[\frac{12K_a^{(4)}}{\omega_a^4}+\frac{K_b^{(4)}}{\omega_a^2\omega_b^2}+\frac{3K_c^{(4)}}{\omega_b^4}\right] .\end{aligned} \tag{3.139}$$

For terms in $\left\langle\phi^2\right\rangle$, we need only consider the cubic term

$$\begin{aligned}\left(K^{(3)}\right)^2\left\langle\left(y^3-3x^2y\right)^2\right\rangle &= \left(K^{(3)}\right)^2\left\langle y^6-6x^2y^4+9x^4y^2\right\rangle \\ &= \frac{24\left(K^{(3)}\right)^2}{\beta^3M^3\omega_a^6} .\end{aligned} \tag{3.140}$$

Thus, we have a term in $T^{7/2}$, and a term in $T^{9/2}$. Now we perform our expansion. Firstly, we have

$$f_{\text{ah}}^{\text{PIC}} = -k_{\text{B}}T\ln\left\{1-\beta\left\langle\phi_{\text{ah}}\right\rangle+\frac{1}{2!}\beta^2\left\langle\phi^2\right\rangle-+\cdots\right\} . \tag{3.141}$$

Using the expansion

$$\ln(1+x) = x-\frac{1}{2}x^2+\frac{1}{3}x^4-+\cdots \tag{3.142}$$

we obtain

$$\begin{aligned}f_{\text{ah}}^{\text{PIC}} &= \left\langle\phi_{\text{ah}}\right\rangle-\frac{\beta}{2}\left\langle\phi_{\text{ah}}^2\right\rangle+O\left(T^3\right) \\ &= \frac{k_{\text{B}}^2T^2}{M^2}\left[\frac{12K_a^{(4)}}{\omega_a^4}+\frac{K_b^{(4)}}{\omega_a^2\omega_b^2}+\frac{3K_c^{(4)}}{\omega_b^4}-\frac{12\left(K^{(3)}\right)^2}{M\omega_a^6}\right]+O\left(T^3\right) \\ &= dT^2+O\left(T^3\right) .\end{aligned} \tag{3.143}$$

So, I find that the anharmonic free energy may be expressed as a power series in T. In my calculations, I shall be able to compare the explicit power-series representation given here, with the results of a numerical evaluation of the integral in (3.110) of Sec. 3.4.1.

Reality is the leading cause of
stress for those in touch with it.

Jane Wagner (1935–)

Chapter 4

The theory of elasticity under stress

4.1 Introduction

As described in Ch. 1, one of the chief aims of this work is to understand the observed seismic anisotropy of the inner core, by computing the elastic constants of hcp iron at inner-core conditions of pressure and temperature, and relating this to the anisotropy of elastic-wave velocity. Here I set out the very involved theory of elasticity of materials under stress. I then discuss the relation between the isothermal elastic constants I calculate and the adiabatic constants relevant to elastic wave propagation, and the elastic properties of inhomogeneous media.

When an inhomogeneous crystal is squeezed along any of its axes, it deforms in all directions. The theory of elasticity describes the stress-strain relationships between the various, inequivalent axes of anisotropic crystals. To do this, it is necessary to adopt a tensor notation. I use an indicial notation, where Greek indices are used to denote Cartesian components of a tensor. I also use the summation notation, whereby any Greek index appearing twice in a term is to be summed over all possible values. I frequently refer to a tensor by some general component, i.e. a_α. After discussing the derivation of the elastic moduli in a crystal, I discuss the propagation of sound in inhomogeneous media, and the elastic properties of polycrystals.

4.2 Elastic Theory

This discussion follows principally the arguments of [65] and [66]; however the notation differs.

4.2.1 Strain

A homogeneous deformation of a crystal is a rank-two tensor $u_{\alpha\beta}$ which maps a point in space r_α onto a point $r'_\alpha = (\delta_{\alpha\beta} + u_{\alpha\beta})r_\beta$. If we decompose $u_{\alpha\beta}$ into symmetric and antisymmetric contributions

$$\varepsilon_{\alpha\beta} \equiv \frac{1}{2}(u_{\alpha\beta} + u_{\beta\alpha}) \quad \text{and} \quad \omega_{\alpha\beta} \equiv \frac{1}{2}(u_{\alpha\beta} - u_{\beta\alpha}) \,, \tag{4.1}$$

then $\varepsilon_{\alpha\beta}$ is called the strain. A comment should be made about this choice, as it is not the only possible definition of strain. A purely rotational deformation results in no change of elastic energy in the crystal. An irrotational deformation is one which contains no rotational component. The above definition of strain is irrotational to first order; that is, the energy change associated with $\omega_{\alpha\beta}$ is second order in $\omega_{\alpha\beta}$. It is possible to define a purely irrotational strain (the so-called Lagrangian strain, denoted $\eta_{\alpha\beta}$), which is, perhaps, a more natural definition; however it is more mathematically awkward to work with, so I do not use this.

To summarize: for our purposes, a strain $\varepsilon_{\alpha\beta}$ on a lattice L is a symmetric tensor $\varepsilon_{\alpha\beta} : L \to L,\ r_\alpha \mapsto (\delta_{\alpha\beta} + \varepsilon_{\alpha\beta})r_\beta$.

4.2.2 Stress

For any given configuration (label it A) of a lattice, the stress can be defined. Applying an infinitesimal deformation $\mathrm{d}u_{\alpha\beta} = \mathrm{d}\varepsilon_{\alpha\beta} + \mathrm{d}\omega_{\alpha\beta}$ yields a change dW in the internal energy per primitive cell of the crystal. The stress *in the initial configuration* A is given by

$$\sigma^A_{\alpha\beta} \equiv \frac{1}{V^A} \lim_{u_{\alpha\beta}\to 0} \left\{ \frac{\partial W}{\partial u_{\alpha\beta}} \right\} = \frac{1}{V^A} \lim_{\varepsilon_{\alpha\beta}\to 0} \left\{ \frac{\partial W}{\partial \varepsilon_{\alpha\beta}} \right\} , \tag{4.2}$$

where V^A is the volume of the primitive cell in the configuration A. Note that under this choice of sign convention, the pressure $p \equiv -\sigma_{\alpha\beta}\delta_{\alpha\beta}/3$. The negative of the stress tensor is sometimes called the *pressure tensor* $p_{\alpha\beta} \equiv -\sigma_{\alpha\beta}$.

4.2.3 Elastic constants from free energy

The stress tensor in a given lattice may be calculated analytically for an empirical potential, or by a generalisation of the Hellman-Feynman formula, for *ab initio* techniques. Some techniques, however, such as harmonic theory, or the particle-in-cell model, calculate only free energies, and it is necessary to determine how to relate the stress-strain and energy-strain characteristics of a lattice. Here the strains can be taken to be applied at either constant temperature or constant entropy. The relationship between the two sets of constants — isothermal and adiabatic — is the the subject of sec. 4.5.

We define a reference configuration A and a final configuration B, connected by a deformation tensor $u_{\alpha\beta}$. About B we make a further deformation $v_{\alpha\beta}$, which carries the lattice to a configuration C. The total deformation relative to A is

$$\begin{aligned} w_{\alpha\beta} &= v_{\alpha\beta} \circ u_{\alpha\beta} \\ \Rightarrow \delta_{\alpha\beta} + w_{\alpha\beta} &= (\delta_{\alpha\gamma} + v_{\alpha\gamma})(\delta_{\gamma\beta} + u_{\gamma\beta}) \\ \Rightarrow w_{\alpha\beta} &= u_{\alpha\beta} + v_{\alpha\beta} + v_{\alpha\gamma}u_{\gamma\beta} \end{aligned} \tag{4.3}$$

The free energy difference can be Taylor expanded

$$\frac{W^C - W^A}{V^A} = \sigma^A_{\alpha\beta} w_{\alpha\beta} + \frac{1}{2} S^A_{\alpha\beta\sigma\tau} w_{\alpha\beta} w_{\sigma\tau} + \cdots , \tag{4.4}$$

$$= \sigma^A_{\alpha\beta} w_{\alpha\beta} + \frac{1}{2} S^A_{\alpha\beta\sigma\tau} w_{\alpha\beta} w_{\sigma\tau} + \cdot$$

where $S^A_{\alpha\beta\sigma\tau} = S^A_{\sigma\tau\alpha\beta}$. The stress in configuration B is given by

$$\begin{aligned}
\sigma^B_{\alpha\beta} &= \frac{1}{V^B} \lim_{v_{\alpha\beta}\to 0} \left\{ \frac{\partial W^C}{\partial v_{\alpha\beta}} \right\} \\
&= (1 + \delta_{\kappa\lambda} u_{\kappa\lambda})^{-1} \frac{1}{V^A} \lim_{v_{\alpha\beta}\to 0} \left\{ \frac{\partial W^C}{\partial v_{\alpha\beta}} \right\} \\
&= (1 - \delta_{\kappa\lambda} u_{\kappa\lambda}) \lim_{v_{\alpha\beta}\to 0} \frac{\partial}{\partial v_{\alpha\beta}} \Big[\sigma^A_{\mu\nu} (u_{\mu\nu} + v_{\mu\nu} + v_{\mu\gamma} u_{\gamma\nu}) \cdots \qquad (4.5) \\
&\quad + \frac{1}{2} S^A_{\mu\nu\sigma\tau} (u_{\mu\nu} + v_{\mu\nu} + v_{\mu\gamma} u_{\gamma\nu})(u_{\sigma\tau} + v_{\sigma\tau} + v_{\sigma\rho} u_{\rho\tau}) \Big] \\
&= (1 - \delta_{\kappa\lambda} u_{\kappa\lambda}) \left[\sigma^A_{\alpha\beta} + (S^A_{\alpha\beta\sigma\tau} + \sigma^A_{\alpha\tau} \delta_{\beta\sigma}) u_{\sigma\tau} \right]
\end{aligned}$$

$$\Rightarrow \qquad \sigma^B_{\alpha\beta} = \sigma^A_{\alpha\beta} + (S^A_{\alpha\beta\sigma\tau} - \sigma^A_{\alpha\beta} \delta_{\sigma\tau} + \sigma^A_{\alpha\tau} \delta_{\beta\sigma}) u_{\sigma\tau} \ . \qquad (4.6)$$

In the above, we have neglected terms of order u^2 and higher, and have employed the symmetry $S_{\alpha\beta\sigma\tau} = S_{\sigma\tau\alpha\beta}$.

Before continuing, it is necessary to derive some basic properties of the $S_{\alpha\beta\sigma\tau}$. We consider a system in a state A subjected to an arbitrary strain $u_{\alpha\beta}$, and an infinitesimal rotation $\omega_{\alpha\beta}$. Recalling that $\omega_{\alpha\beta} = -\omega_{\beta\alpha}$, the change in the free energy may be written

$$\begin{aligned}
\frac{1}{V^A}(W - W^A) &= \sigma^A_{\alpha\beta} (u_{\alpha\beta} + \omega_{\alpha\beta} + \omega_{\alpha\gamma} u_{\gamma\beta}) \cdots \\
&\quad + \frac{1}{2} S^A_{\alpha\beta\sigma\tau} (u_{\alpha\beta} + \omega_{\alpha\beta})(u_{\sigma\tau} + \omega_{\sigma\tau}) + \cdots \ ,
\end{aligned} \qquad (4.7)$$

and, by permutation of indices,

$$\begin{aligned}
\frac{1}{V^A}(W - W^A) &= \sigma^A_{\alpha\beta} (u_{\alpha\beta} - \omega_{\beta\alpha} - \omega_{\gamma\alpha} u_{\gamma\beta}) \cdots \\
&\quad + \frac{1}{2} S^A_{\alpha\beta\sigma\tau} (u_{\alpha\beta} - \omega_{\beta\alpha})(u_{\sigma\tau} - \omega_{\tau\sigma}) + \cdots \ .
\end{aligned} \qquad (4.8)$$

Rotational invariance means that that (4.7) and (4.8) are independent of $\omega_{\alpha\beta}$ to first order. Differentiating both expressions and adding, one obtains (with some relabelling of indices)

$$\sigma^A_{\alpha\beta} - \sigma^A_{\beta\alpha} + \left[\sigma^A_{\alpha\tau} \delta_{\beta\sigma} - \sigma^A_{\beta\tau} \delta_{\alpha\sigma} + S^A_{\alpha\beta\sigma\tau} - S^A_{\beta\alpha\tau\sigma} \right] u_{\sigma\tau} + O(u^2) = 0 \ . \qquad (4.9)$$

This expression holds for arbitrary $u_{\alpha\beta}$, therefore (dropping the label A)

$$\sigma_{\alpha\beta} = \sigma_{\beta\alpha} \qquad (4.10)$$

$$\sigma^A_{\alpha\tau} \delta_{\beta\sigma} - \sigma^A_{\beta\tau} \delta_{\alpha\sigma} + S^A_{\alpha\beta\sigma\tau} - S^A_{\beta\alpha\tau\sigma} = 0 \ . \qquad (4.11)$$

We now wish to write (4.6) in terms of the strain, and so we make the substitution $u_{\alpha\beta} = \varepsilon_{\alpha\beta} + \omega_{\alpha\beta}$. Recalling that $\omega_{\alpha\beta}$ is antisymmetric,

$$\sigma^B_{\alpha\beta} = \sigma^A_{\alpha\beta} + S^A_{\alpha\beta\sigma\tau}(\varepsilon_{\sigma\tau} + \omega_{\sigma\tau}) - \sigma^A_{\alpha\beta}\delta_{\sigma\tau}\varepsilon_{\sigma\tau} + \sigma^A_{\alpha\tau}\delta_{\beta\sigma}(\varepsilon_{\sigma\tau} + \omega_{\sigma\tau}) \ . \tag{4.12}$$

Treating the terms in $\omega_{\alpha\beta}$ first, we have

$$\begin{aligned} S^A_{\alpha\beta\sigma\tau}\omega_{\sigma\tau} &= -S^A_{\alpha\beta\sigma\tau}\omega_{\tau\sigma} \\ &= -S^A_{\alpha\beta\tau\sigma}\omega_{\sigma\tau} \\ \Rightarrow \quad S^A_{\alpha\beta\sigma\tau}\omega_{\sigma\tau} &= \frac{1}{2}(S^A_{\alpha\beta\sigma\tau} - S^A_{\alpha\beta\tau\sigma})\omega_{\sigma\tau} \\ &= \sigma^A_{\beta\tau}\omega_{\alpha\tau} \ , \end{aligned} \tag{4.13}$$

where we have used (4.10) and (4.11) in the last step, and some relabelling of indices. This gives

$$\sigma^B_{\alpha\beta} = \sigma^A_{\alpha\beta} + c^A_{\alpha\beta\sigma\tau}\varepsilon_{\sigma\tau} + (\sigma^A_{\beta\tau}\delta_{\alpha\sigma} + \sigma^A_{\alpha\tau}\delta_{\beta\sigma})\omega_{\sigma\tau} \tag{4.14}$$

where

$$c^A_{\alpha\beta\sigma\tau} = S^A_{\alpha\beta\sigma\tau} - \sigma^A_{\alpha\beta}\delta_{\sigma\tau} + \sigma^A_{\alpha\tau}\delta_{\beta\sigma} \tag{4.15}$$

The above equation (4.15) defines the elastic constants $c^A_{\alpha\beta\sigma\tau}$ for deformations about a configuration A which is subject to arbitrary initial stress. It must be noted that due to the directional (specifically tensorial) nature of the stress, $c^A_{\alpha\beta\sigma\tau}$ is a first-order function of the rotation tensor $\omega_{\alpha\beta}$. In this form, the elastic constants have the full Voigt symmetry (not exhibited by the $S_{\alpha\beta\sigma\tau}$:

$$c_{\alpha\beta\sigma\tau} = c_{\alpha\beta\tau\sigma} \ , c_{\alpha\beta\sigma\tau} = c_{\beta\alpha\sigma\tau} \ , c_{\alpha\beta\sigma\tau} = c_{\sigma\tau\alpha\beta} \ . \tag{4.16}$$

Our goal is to show how to calculate elastic constants from free energy – strain curves. We therefore substitute the definition (4.15) into the expression (4.4) for the free energy density. This gives us

$$\begin{aligned} \frac{W - W^A}{V^A} = \sigma^A_{\alpha\beta}(\varepsilon_{\alpha\beta} + \omega_{\alpha\beta}) + \frac{1}{2}[(c^A_{\alpha\beta\sigma\tau} \cdots + \\ \sigma^A_{\alpha\beta}\delta_{\sigma\tau} - \sigma^A_{\alpha\tau}\delta_{\beta\sigma})\varepsilon_{\alpha\beta}\varepsilon_{\sigma\tau} + S^A_{\alpha\beta\sigma\tau}(\varepsilon_{\alpha\beta}\omega_{\sigma\tau} + \omega_{\alpha\beta}\varepsilon_{\sigma\tau} + \omega_{\alpha\beta}\omega_{\sigma\tau})] \ . \end{aligned} \tag{4.17}$$

Since $\sigma^A_{\alpha\beta} = \sigma^A_{\beta\alpha}$, we have

$$\sigma^A_{\alpha\beta}\omega_{\alpha\beta} = \sigma^A_{\beta\alpha}\omega_{\alpha\beta} = -\sigma^A_{\beta\alpha}\omega_{\beta\alpha} = -\sigma^A_{\alpha\beta}\omega_{\alpha\beta} = 0 \, . \tag{4.18}$$

Next,

$$\begin{aligned}
&\frac{1}{2}S^A_{\alpha\beta\sigma\tau}(\varepsilon_{\alpha\beta}\omega_{\sigma\tau} + \varepsilon_{\sigma\tau}\omega_{\alpha\beta} + \omega_{\alpha\beta}\omega_{\sigma\tau}) \\
&\qquad =\frac{1}{2}S^A_{\alpha\beta\sigma\tau}(2\varepsilon_{\alpha\beta} + \omega_{\alpha\beta})\omega_{\sigma\tau} \\
&\qquad =\frac{1}{4}(S^A_{\alpha\beta\sigma\tau} - S^A_{\alpha\beta\tau\sigma})(2\varepsilon_{\alpha\beta} + \omega_{\alpha\beta})\omega_{\sigma\tau} \\
&\qquad =\frac{1}{4}(\sigma^A_{\beta\tau}\delta_{\alpha\sigma} - \sigma^A_{\beta\sigma}\delta_{\alpha\tau})(2\varepsilon_{\alpha\beta} + \omega_{\alpha\beta})\omega_{\sigma\tau} \\
&\qquad =\frac{1}{2}\sigma^A_{\beta\tau}(2\varepsilon_{\alpha\beta} + \omega_{\alpha\beta})\omega_{\sigma\tau} \\
&\qquad =\frac{1}{2}\sigma^A_{\alpha\beta}(-2\varepsilon_{\alpha\sigma} + \omega_{\alpha\sigma})\omega_{\beta\sigma} \, .
\end{aligned} \tag{4.19}$$

Finally

$$(\sigma_{\alpha\beta}\delta_{\sigma\tau} - \sigma_{\alpha\tau}\delta_{\beta\sigma})\varepsilon_{\alpha\beta}\varepsilon_{\sigma\tau} = \sigma_{\alpha\beta}(\varepsilon_{\alpha\beta}\varepsilon_{\sigma\sigma} - \varepsilon_{\alpha\sigma}\varepsilon_{\sigma\beta}) \, . \tag{4.20}$$

Substituting these results into (4.17), we have

$$\begin{aligned}
\frac{W - W^A}{V^A} =& \sigma^A_{\alpha\beta}\varepsilon_{\alpha\beta} + \frac{1}{2}c^A_{\alpha\beta\sigma\tau}\varepsilon_{\alpha\beta}\varepsilon_{\sigma\tau} \\
&+ \frac{1}{2}\sigma^A_{\alpha\beta}(\varepsilon_{\alpha\beta}\varepsilon_{\sigma\sigma} - \varepsilon_{\alpha\sigma}\varepsilon_{\beta\sigma} - 2\varepsilon_{\alpha\sigma}\omega_{\beta\sigma} + \omega_{\alpha\sigma}\omega_{\beta\sigma}) \, .
\end{aligned} \tag{4.21}$$

This is the principal equation used in calculating elastic constants under strain from free energy.

4.2.4 Isotropic initial stress

An important special case occurs when the initial stress (configuration A) is isotropic, i.e. $\sigma^A_{\alpha\beta} = -p\delta_{\alpha\beta}$, where p is the pressure. Under these conditions, (4.21) reduces to

$$\begin{aligned}
\frac{W - W^A}{V^A} =& -p\varepsilon_{\alpha\alpha} + \frac{1}{2}\Big\{ c^A_{\alpha\beta\sigma\tau} - \frac{1}{2}p(2\delta_{\alpha\beta}\delta_{\sigma\tau} \cdots \\
&- \delta_{\alpha\tau}\delta_{\beta\sigma} - \delta_{\beta\tau}\delta_{\alpha\sigma})\Big\}\varepsilon_{\alpha\beta}\varepsilon_{\sigma\tau} - \frac{1}{2}p\omega_{\alpha\sigma}\omega_{\alpha\sigma} \, .
\end{aligned} \tag{4.22}$$

Equations (4.21) and (4.22) are used heavily in my work on the high-pressure elasticity of iron.

4.3 Sound propagation in anisotropic media

The continuum wave equation in anisotropic media is

$$c_{\alpha\beta\sigma\tau} \frac{\partial^2}{\partial r_\beta \partial r_\tau} u_\sigma = \rho \frac{\partial^2}{\partial t^2} u_\alpha \ . \tag{4.23}$$

By substituting a plane-wave solution of the form

$$\mathbf{u} = \mathbf{e} e^{i(\omega t - \mathbf{k}.\mathbf{r})} \tag{4.24}$$

we have

$$c_{\alpha\beta\sigma\tau} k_\beta k_\sigma e_\tau = \rho \omega^2 e_\alpha \ . \tag{4.25}$$

The wave velocity is given by

$$v^2 = \frac{\omega^2}{k_\lambda k_\lambda} \ ; \tag{4.26}$$

by writing the wavevectors in terms of direction cosines n_α, such that $k_\alpha = k n_\alpha$, we obtain the *Christoffel equation*

$$(c_{\alpha\beta\sigma\tau} n_\beta n_\tau - \rho v^2 \delta_{\alpha\sigma}) e_\sigma = 0 \ . \tag{4.27}$$

4.4 Symmetries of the hcp lattice

As I will be considering the elasticity of hcp Fe in the Earth's inner core, I discuss here elastic constants in hcp symmetry. In the hcp lattice, there are five independent elastic constants. Labelling the three-fold axis as coordinate direction 3, these are c_{1111} c_{3333}, c_{1122}, c_{1133} and c_{2323}. The shear constant c_{1212} is given by $c_{1212} = (c_{1111} - c_{1122})/2$. In the Voigt notation, these are denoted

$$c_{11} \equiv c_{1111} \ , \qquad c_{33} \equiv c_{3333} \ , \tag{4.28}$$

$$c_{12} \equiv c_{1122} \ , \qquad c_{13} \equiv c_{1133} \ , \tag{4.29}$$

$$c_{44} \equiv c_{2323} \ , \qquad c_{66} \equiv c_{1212} = \frac{1}{2}(c_{11} - c_{12}) \ . \tag{4.30}$$

We can also use the symmetries of the lattice to simplify the Christoffel equation. The polarization vector $\mathbf{e}$ has unit length, therefore

$$\begin{aligned} c_{\alpha\beta\sigma\tau} e_\alpha n_\beta e_\sigma n_\tau &= \rho v^2 \delta_{\alpha\sigma} e_\alpha e_\sigma \\ &= \rho v^2 \ . \end{aligned} \tag{4.31}$$

We consider the velocities of compressional and transverse waves as a function of direction in the crystal, for $\mathbf{n} = (\sin\theta, 0, \cos\theta)$, $0 \le \theta \le \pi/2$. For compressional (p-) polarization, we have $\mathbf{e} = \mathbf{n}$, therefore:

$$\begin{aligned} \rho v_p^2 &= c_{1111} \sin^4\theta + 2c_{1133} \sin^2\theta \cos^2\theta + c_{3333} \cos^4\theta \\ &\quad + 4c_{1313} \sin\theta\cos\theta\sin\theta\cos\theta \\ &= c_{11} + 2(c_{13} - c_{11} + 2c_{44}) \cos^2\theta \\ &\quad + (c_{11} - 2c_{13} + c_{33} - 4c_{44}) \cos^4\theta \ . \end{aligned} \tag{4.32}$$

We consider transverse- or s-polarized waves which oscillate in the planes containing the vectors $(0,1,0)$ and $(0,0,1)$. In each case, the polarization vector is perpendicular to this vector, and to the direction $\mathbf{n}$ of propagation. In the case of s-waves oscillating in-plane with the vector $(0,0,1)$, the polarization vector is

$$\mathbf{e} = \mathbf{n}_\wedge(0,0,1) / \left|\mathbf{n}_\wedge(0,0,1)\right| = (0,1,0) \ , \tag{4.33}$$

and

$$\begin{aligned} \rho v_p^2 &= c_{2121} \sin^2\theta + c_{2323} \cos^2\theta \\ &= c_{66} + (c_{44} - c_{66} \cos^2\theta) \ . \end{aligned} \tag{4.34}$$

In the case of s-waves oscillating in-plane with the vector $(0,1,0)$, the polarization vector is

$$\mathbf{e} = \mathbf{n}_\wedge(0,1,0) / \left|\mathbf{n}_\wedge(0,1,0)\right| = (-\cos\theta, 0, \sin\theta) \ , \tag{4.35}$$

and

$$\begin{aligned} \rho v_p^2 &= c_{44} + (c_{11} - 2c_{13} + c_{33} - 4c_{44}) \cos^2\theta \\ &\quad + (4c_{44} - c_{11} + 2c_{13} - c_{33}) \cos^4\theta \ . \end{aligned} \tag{4.36}$$

4.5 Thermoelasticity

So far I have said nothing about the thermodynamic conditions under which the strains $\varepsilon_{\alpha\beta}$ are applied. In the various statistical mechanical methods I employ, it is natural to perform constant temperature calculations. The elastic constants calculated in this way are the *isothermal* elastic constants, which I shall now label $c^T_{\alpha\beta\sigma\tau}$. When I consider elastic waves, however, I require the *adiabatic* elastic constants $c^S_{\alpha\beta\sigma\tau}$, and I describe here the relation between the two. This discussion is based predominantly on [67], and I follow the author in assuming a unit volume.

The first law of thermodynamics may be written

$$\mathrm{d}U = \sigma_{\alpha\beta}\mathrm{d}\varepsilon_{\alpha\beta} + T\mathrm{d}S\,. \tag{4.37}$$

We go over to the Gibbs free energy for non-hydrostatic conditions

$$G = U - \sigma_{\alpha\beta}\varepsilon_{\alpha\beta} - TS\,. \tag{4.38}$$

Differentiating

$$\mathrm{d}G = -\varepsilon_{\alpha\beta}\mathrm{d}\sigma_{\alpha\beta} - S\mathrm{d}T\,. \tag{4.39}$$

If follows immediately that

$$\left(\frac{\partial G}{\partial \sigma_{\alpha\beta}}\right)_T = -\varepsilon_{\alpha\beta}\,, \qquad \left(\frac{\partial G}{\partial T}\right)_\sigma = -S\,, \tag{4.40}$$

from which we have the Maxwell relation

$$\left(\frac{\partial \varepsilon_{\alpha\beta}}{\partial T}\right)_\sigma = -\frac{\partial^2 G}{\partial \sigma_{\alpha\beta}\partial T} = \left(\frac{\partial S}{\partial \sigma_{\alpha\beta}}\right)_T\,. \tag{4.41}$$

We write down the following chain rules:

$$\mathrm{d}\varepsilon_{\alpha\beta} = \left(\frac{\partial \varepsilon_{\alpha\beta}}{\partial \sigma_{\sigma\tau}}\right)_T \mathrm{d}\sigma_{\sigma\tau} + \left(\frac{\partial \varepsilon_{\alpha\beta}}{\partial T}\right)_\sigma \mathrm{d}T \tag{4.42}$$

and

$$\mathrm{d}S = \left(\frac{\partial S}{\partial \sigma_{\sigma\tau}}\right)_T \mathrm{d}\sigma_{\sigma\tau} + \left(\frac{\partial S}{\partial T}\right)_\sigma \mathrm{d}T\,. \tag{4.43}$$

Eliminating $\mathrm{d}T$ and putting $\mathrm{d}S = 0$ we obtain

$$\mathrm{d}\varepsilon_{\alpha\beta} = \left(\frac{\partial \varepsilon_{\alpha\beta}}{\partial \sigma_{\sigma\tau}}\right)_T \mathrm{d}\sigma_{\sigma\tau} + \left(\frac{\partial \varepsilon_{\alpha\beta}}{\partial T}\right)_\sigma \left(\frac{\partial S}{\partial \sigma_{\sigma\tau}}\right)_T \mathrm{d}\sigma_{\sigma\tau} \Big/ \left(\frac{\partial S}{\partial T}\right)_\sigma , \tag{4.44}$$

And dividing by $\mathrm{d}\sigma_{\sigma\tau}$ and using the above Maxwell relation,

$$\left(\frac{\partial \varepsilon_{\alpha\beta}}{\partial \sigma_{\sigma\tau}}\right)_S - \left(\frac{\partial \varepsilon_{\alpha\beta}}{\partial \sigma_{\sigma\tau}}\right)_T = -\left(\frac{\partial \varepsilon_{\alpha\beta}}{\partial T}\right)_\sigma \left(\frac{\partial \varepsilon_{\sigma\tau}}{\partial T}\right)_\sigma \left(\frac{\partial T}{\partial S}\right)_\sigma . \tag{4.45}$$

And so

$$(c^S_{\alpha\beta\sigma\tau})^{-1} - (c^T_{\alpha\beta\sigma\tau})^{-1} = -\left(\frac{\partial \varepsilon_{\alpha\beta}}{\partial T}\right)_\sigma \left(\frac{\partial \varepsilon_{\sigma\tau}}{\partial T}\right)_\sigma \left(\frac{\partial T}{\partial S}\right)_\sigma . \tag{4.46}$$

Recalling that the heat capacity $C = T(\mathrm{d}S/\mathrm{d}T)$, this yields

$$(c^S_{\alpha\beta\sigma\tau})^{-1} - (c^T_{\alpha\beta\sigma\tau})^{-1} = -\alpha_{\alpha\beta}\alpha_{\sigma\tau}VT/C_\sigma \tag{4.47}$$

where C_σ is defined for constant volume deformation, and we have introduced the linear expansivities $\alpha_{\alpha\beta} = (\partial\varepsilon_{\alpha\beta}/\partial T)_\sigma$. In the last expression we have reintroduced the volume. This is that volume having heat capacity C_σ, conventionally an atom, simulation cell, or mole.

In the case of an h.c.p. lattice with axial ratio $q = c/a$, volume per atom $V = \sqrt{3}a^2c/4$, there are two independent linear expansivities, $\alpha_{11} = \alpha_{22}$, and α_{33}. Because the crystal does not spontaneously shear under hydrostatic stress, the off-diagonal expansivities are zero. Now,

$$a = \left(\frac{4V}{q\sqrt{3}}\right)^{1/3}, \qquad c = \left(\frac{4Vq^2}{\sqrt{3}}\right)^{1/3} \tag{4.48}$$

and we have

$$\begin{aligned} \alpha_{11} = \alpha_{22} &= \left(\frac{\partial \varepsilon_{11}}{\partial V}\right)_\sigma \left(\frac{\partial V}{\partial T}\right)_\sigma + \left(\frac{\partial \varepsilon_{11}}{\partial q}\right)_\sigma \left(\frac{\partial q}{\partial T}\right)_\sigma \\ &= \frac{\alpha_V}{3} - \frac{\alpha_q}{3} , \end{aligned} \tag{4.49}$$

and

$$\begin{aligned} \alpha_{33} &= \left(\frac{\partial \varepsilon_{33}}{\partial V}\right)_\sigma \left(\frac{\partial V}{\partial T}\right)_\sigma + \left(\frac{\partial \varepsilon_{33}}{\partial q}\right)_\sigma \left(\frac{\partial q}{\partial T}\right)_\sigma \\ &= \frac{\alpha_V}{3} + \frac{2\alpha_q}{3} . \end{aligned} \tag{4.50}$$

In the above, α_V in the usual volumetric expansivity, and we define $\alpha_q = (\partial q/\partial T)_\sigma/q$. With the above results we are able to use thermodynamic derivatives to transform between isothermal and adiabatic elastic moduli.

4.6 Elastic properties of polycrystalline aggregates

The Earth's core is not comprised of a single, massive crystal of Fe, but a polycrystalline aggregate of Fe crystallites. How can we understand the elasticity of such a system?

Voigt [68] proposed a scheme in which the strain is considered to be uniform throughout a sample of material. In this scheme, the formulae for the bulk and shear moduli are

$$K_{\mathrm{V}} = \frac{1}{3}(A + 2B) \quad \text{and} \quad \mu_{\mathrm{V}} = \frac{1}{5}(A - B + 3C) \tag{4.51}$$

respectively, where

$$A = \frac{1}{3}(c_{11} + c_{22} + c_{33}) \tag{4.52}$$

$$B = \frac{1}{3}(c_{12} + c_{23} + c_{31}) \tag{4.53}$$

$$C = \frac{1}{3}(c_{44} + c_{55} + c_{66}) \tag{4.54}$$

respectively.

Reuss [69] proposed an alternative scheme in which the it is the strain which is considered to be uniform. The Reuss scheme gives

$$\frac{1}{K_{\mathrm{G}}} = 3(D + 2E) \quad \text{and} \quad \mu = \frac{1}{5}(4D - 4E + 3F) \tag{4.55}$$

where

$$D = \frac{1}{3}\left(\frac{1}{c_{11}} + \frac{1}{c_{22}} + \frac{1}{c_{33}}\right) \tag{4.56}$$

$$E = \frac{1}{3}\left(\frac{1}{c_{12}} + \frac{1}{c_{23}} + \frac{1}{c_{31}}\right) \tag{4.57}$$

$$F = \frac{1}{3}\left(\frac{1}{c_{44}} + \frac{1}{c_{55}} + \frac{1}{c_{66}}\right) . \tag{4.58}$$

Hill [70] has shown that the Voigt and Reuss average comprise an upper and lower bound respectively for the aggregate moduli, allowing us to attribute a precision to our estimation.

With these values, one can calculate the usual Poisson's Ratio

$$\nu = \frac{3K - 2\mu}{2(3K + \mu)} \,. \tag{4.59}$$

Poisson's ratio for the Earth's core is well known from seismic studies, therefore its determination will be an important test of my calculations.

> ... mi ritrovai per una selva
> oscura, chè la diritta via era
> smarrita.
>
> Dante Alighieri (1265–1321)

Chapter 5

An evaluation of the "particle-in-cell" model

5.1 Introduction

The "particle-in-cell" (PIC) model as described in Sec. 3.4 has been used successfully to describe the thermodynamic properties of many materials; however, as has been discussed, the approximation is not well-founded, in the sense that there is no systematic method of estimating the size of errors introduced, nor does the non-correlated dynamics of the PIC model correspond to any well-defined limit, such as that of small vibrations (c.f. sec 3.2 on the harmonic approximation). For these reasons there is a difficult question of justification, as it is difficult to see, *a priori*, under what circumstances the PIC model is, or is not, justified.

The use of the PIC model in this chapter, is to understand the significant discrepancies between *ab initio* -based molecular dynamics calculations by Alfè *et al.* [34] on the one hand, and earlier PIC calculations due to Wasserman *et al.* [36] and Stixrude *et al.* [37] on the other. The comparison would comprise the calculation of a variety of thermodynamic functions using the PIC model, employing electronic structure methods identical with those of

Alfè *et al.* [34]. The calculations obtained were compared with the results of references [36], [37] and [34], thereby permitting us to study in isolation the effects of the PIC approximation. Having established the effects of the PIC approximation on the various thermodynamics quantities, I went on to examine the temperature dependence of the c/a equilibrium axial ratio of hcp Fe, which is compared with earlier PIC calculations due to Steinle-Neumann *et.al* [35].

The remainder of this chapter is organized as follows: in Sec. 5.2, I discuss the previous calculation of [36], [37], [35] and [34], contrast their methodologies, and highlight discrepancies in results; in Sec. 5.3 I describe the electronic structure calculations employed, and practical considerations arising in their use. I then present results on the perfect lattice contribution to the free energy. In Sec. 5.4 I describe in detail my implementation of the PIC method and calculations of harmonic and anharmonic vibrational free energies. In Sec. 5.5 I present new PIC calculation of the c/a equilibrium aspect ratio of hcp Fe, contrasted with the results of [35]. In Sec. 5.6 I present new calculations of various thermodynamic functions in the PIC model, contrasted with the results of [36], [37] and [35], and in Sec. 5.7 I discuss the implications of these results for the reliability of PIC calculations for hcp Fe. The results obtained in this chapter have been published in Gannarelli *et al.* [71].

5.2 Previous calculations

The various calculations of thermodynamic quantities described in this chapter all arise from determinations of the free energy. In the calculations of Alfè *et al.* [34], the free energy is obtained from *ab initio* molecular dynamics simulations, by thermodynamic integration. In the calculations of Wasserman *et al.* [36], Stixrude *et al.*, [37], Steinle-Neumann *et al.* [35], and in my own calculations, the free energy is obtained using the PIC model.

The first application of the PIC model to Earth's core iron was due to Wasserman *et al* [36], who used the method to calculate a variety of thermoelastic properties, on the basis of a tight-binding total-energy (TBTE) electronic structure scheme. In a very significant paper [37], this group went on to consider the temperature of the inner core, by computing the bulk modulus and density of solid iron, and comparing this with seismic observations. In this work, electronic structure calculations were based on DFT in the linearized augmented plane wave (LAPW) approach [72], and the group used this method to repeat many of the calculations of [36], still working within the PIC approximation.

Laio *et al.* [73] put these results to an early test, by using classical molecular dynamics, parameterized on *ab initio* electronic structure calculations, to compute the melting curve, and the shear and bulk moduli of hcp Fe. The next significant development in the theoretical study of inner core iron was the calculations of Alfè *et al.* [34]. Alfè and coworkers used DFT-based molecular dynamics calculations in the projector augmented wave approach (see Sec. 2.11 and ref. [14]) in conjunction with thermodynamic integration to calculate the fully *ab initio* free energy of iron as a function of temperature and pressure, from which they were able to compute various thermodynamic quantities. These results are significant in that they remove the uncontrolled approximations of PIC model. Whereas the errors introduced by ignoring atomic correlations cannot be readily estimated, the statistical uncertainty introduced by performing molecular dynamics simulations of finite length are easily computed, placing limits on the possible errors in the calculations. Thus, Alfè *et al.* produced the first reliable calculations of the thermodynamics of Earth's core iron.

The most important results of the various papers are reproduced and contrasted in Figs. 5.9–5.18, along with my new calculations. It is observed, for example, that for both the p–V and T–p curves on the Hugoniot (Figs.

5.14 and 5.15), the various calculations are in excellent agreement with one another, and with experiment, whereas for the Grüneisen parameter, for example, the various calculations yield highly divergent results. One of the most striking observations of all, however, is the temperature dependence of the axial ratio $q \equiv c/a$ of [36], which is seen to rise from around 1.575 at zero temperature to in excess of 1.85 at 2000 K and 9.62 Å^3, or from around 0.96 to 1.13 of the ideal value $q_0 = 2\sqrt{2/3} \approx 1.633$, representing an increase of around 18%. This particular result is considered in ch. 6.

In order to discover the source of the discrepancy between the results of [36] and [37] on the one hand, and those of [34] on the other, it was decided to perform new thermodynamic calculations in the PIC approximation, using the PAW techniques of Alfè *et al.* This would permit us to distinguish between the errors introduced by the particle-in-cell model, and any discrepancies that might arise from the different electronic structure methods involved.

5.3 Electronic structure calculations

All calculations of the free energy begin with the calculation of the free energy of the static-ion system, with a finite electronic temperature. This is performed using finite-temperature DFT with a Perdew-Wang (PW91) generalized gradient approximation (GGA) to the exchange-correlation energy [13], and employing the PAW method. The computer code used to achieve this is VASP [74, 75, 76], originally by Georg Kresse and Jürgen Furthmüller. This code was used to calculate both the free energy $F_{\text{perf}}(V, T_{\text{el}})$ of the perfect lattice, and the cell potential $\phi(\mathbf{R}; V, T_{\text{el}})$ of eq. (3.109).

The PAW datasets which define the mapping (2.86) are as described in ref. [76]. These define a core region Ω_R of radius 2.2 a.u. about each ion centre, and a partial wave cutoff energy of 300 eV. VASP provides PAW datasets including either $3d$, $4s$ and $4p$ electrons, or $3p$, $3d$, $4s$ and $4p$.

As discussed in ref. [32] and elsewhere, it is important at high pressures to include the response of $3p$ electrons in my calculations; however for extensive calculations using large cells, this has a serious impact on computational expense. I therefore follow ref. [32] in accounting for the $3p$ response by means of an effective pair potential

$$\phi_{\text{pair}}(r) \equiv \frac{1}{N_{\text{pairs}}} \left[F^{3p}_{\text{perf}}(r) - F^{3\bar{p}}_{\text{perf}}(r) \right] \tag{5.1}$$

where $F^{3p}_{\text{perf}}(r)$ and $F^{3\bar{p}}_{\text{perf}}(r)$ represent the h.c.p. perfect lattice free energies for nearest neighbour separation r, including and excluding $3p$ electron response respectively. The potential is represented in my computations by cubic spline interpolation over a table of values. As discussed in ref. [32], this is observed to yield errors of less than 0.25% in the parameters of the perfect-lattice equation of state, and of around 1–2% in the phonon frequencies.

Before performing any computations, it is necessary to study the effects of various parameters, all of which must be brought to convergence. The most important of these include the density of k-points for Brillouin zone sampling and the plane wave cutoff E_{cut} defined so the sum in eq. (2.84) extends over all reciprocal lattice vectors $\mathbf{G}$ such that $(\mathbf{k}+\mathbf{G})^2/2m \leq E_{\text{cut}}$. This cutoff has a default value for a given pseudopotential, which may be changed, either by choosing high or low precision, or by specifying the value of E_{cut} oneself. In treating the free energy as a function of volume, it is clear that the number of plane wave included, and hence the completeness of the plane wave basis will change as a function of volume, causing discontinuous changes in the energy (this being closely related to the phenomenon of Pulay stresses). As a result of this, an unusually high cutoff may be required for my purposes.

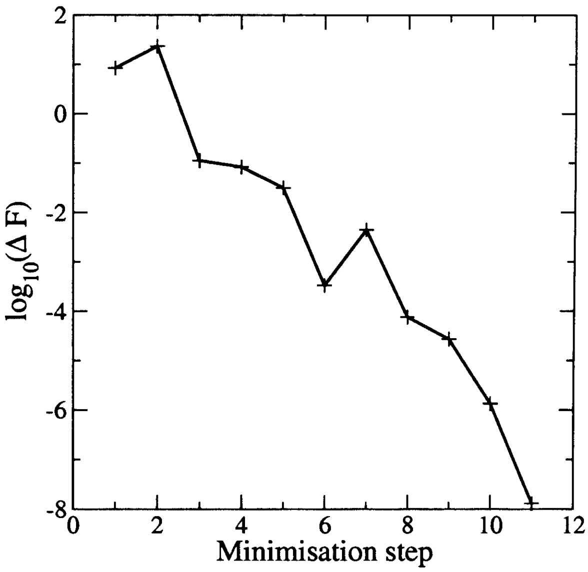

Figure 5.1: Logarithmic change ΔF in free energy at each step of a minimization process using density mixing.

5.3.1 Free energy minimization

For a given cell, with given electronic temperature, k-point sampling and plane-wave cutoff, the free energy is minimized with the help of density mixing. As a result, one does not see a monotonic decrease of energy with minimization step. Fig. 5.1 shows this process for a two-atom cell of hcp Fe, with atomic volume $V = 6.97$ Å^3, $T_{\mathrm{el}} = 6000$ K, a 9×9×7 Monkhorst-Pack k-point sampling, and a plane-wave cutoff of $E_{\mathrm{cut}} = 300$ eV. The figure shows the energy change at each minimization step. I note the spike at around 10^{-3} eV: features like this can occur at all energies; therefore one must anticipate that by establishing as a convergence criterion $\Delta F \leq 10^{-6}$ eV, one may see convergence no better than around $\Delta F \leq 10^{-5}$ eV. Throughout this chapter I use a convergence criterion of $\Delta F \leq 10^{-6}$ eV.

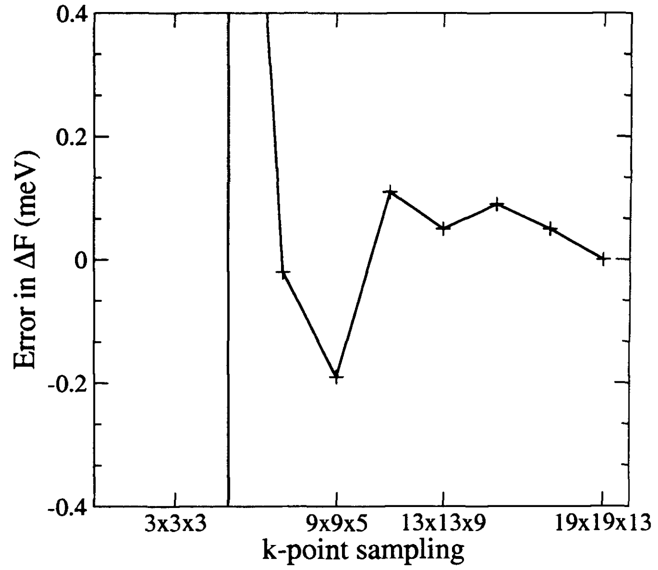

Figure 5.2: Error in the free energy difference ΔF (defined to be zero for the $19 \times 19 \times 13$ grid), for various finenesses of k-point grid.

5.3.2 Convergence of k points

k-point convergence is strongly affected by electronic temperature. This is because at finite temperature the Fermi surface becomes smeared out, with occupancies dropping to zero over in some shell of finite thickness $\mathrm{d}k \approx 2mk_\mathrm{B}T/k_\mathrm{F}$. At zero temperature, then, the occupancy becomes a step in k space, which requires to be sampled on an extremely dense k-point grid. For this reason, it is sufficient to test k-point sampling at the lowest temperatures to be treated. Here I use a temperature of 1000 K.

For the computation of F_perf, I use a two-atom h.c.p. cell. My intention is to bring to convergence the free energy difference $\Delta F = F_\mathrm{perf}(V_1) - F_\mathrm{perf}(V_2)$ between cells at two volumes. My target for convergence is 0.5 meV. Employing a variety of Monkhorst-Pack [50] k-point grids we see (fig. 5.2) that this precision is comfortably achieved for a $9 \times 9 \times 5$ k-point mesh. Here $V_1 = 6.97$ Å^3 per atom, and $V_2 = 7.50$ Å^3 per atom. I in fact use a some-

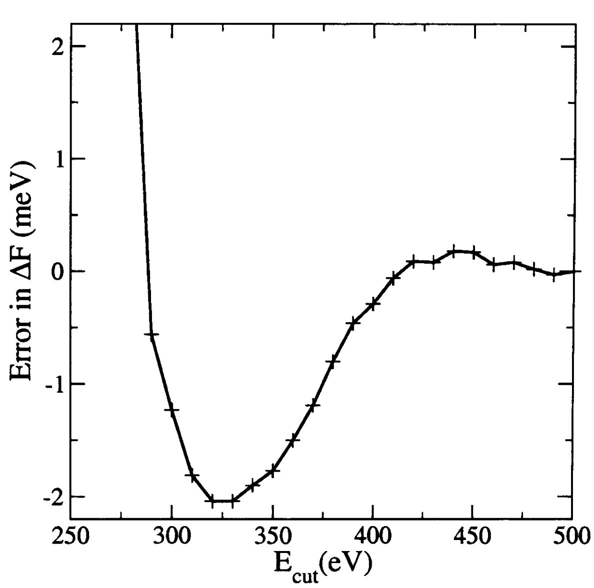

Figure 5.3: Error in the free energy difference ΔF (defined to be zero for a 500 eV cutoff) as a function of plane-wave cutoff E_{cut}.

what higher-density $15 \times 15 \times 9$ grid of k for my perfect-lattice calculations. For supercells, I employ a lower number of k points to ensure identical sampling of the reciprocal space. This will be discussed further when I consider convergence with respect to supercell size.

5.3.3 Convergence of plane-wave cutoff

Taking the same values of V_1 and V_2, I examine the effect on the energy difference $F_{\mathrm{perf}}(V_1) - F_{\mathrm{perf}}(V_2)$ of varying E_{cut}; the results are shown in figure 5.3. We note that the target convergence of 0.5 meV is easily achieved for the a cutoff of 400 eV.

5.3.4 Perfect lattice results

The free energy of the perfect lattice was now computed over a range of electronic temperature 500 K $\leq T_{\mathrm{el}} \leq$ 8000 K and atomic volume 5.5 $\mathrm{\AA}^3 \leq$

$V \leq 10.5\ \text{Å}^3$ for a fixed axial ratio of 1.60. For every value of T_{el}, the results were fitted to a third-order Birch-Murnaghan equation of state [57], the coefficients of which were fitted as fifth-order polynomial functions of T_{el}. These calculations essentially repeated those earlier reported by Alfè *et al.* [34] and are presented below. Additionally, I can allow for relaxation of the c/a ratio by defining the deviation $\Delta F_{\text{perf}}(V, q, T_{\text{el}}) \equiv F_{\text{perf}}(V, q, T_{\text{el}}) - F_{\text{perf}}(V, q_0, T_{\text{el}})$, where $q_0 = 1.60$. For given q, T_{el}, this quantity has the quadratic form

$$\Delta F_{\text{perf}}(q) = \alpha(q - q_0)(q - q_1) \tag{5.2}$$

where α and q_1 are functions of volume and temperature given by

$$\alpha = a + bT_{\text{el}} \qquad q_1 = r + sT_{\text{el}} \tag{5.3}$$

with $a = a^{(0)} + a^{(1)}V$ and similarly for b, r and s.

The Birch-Murnaghan equation is given by

$$\begin{aligned} F_{\text{perf}}(V) = F^{(0)} + \frac{3}{2}V^{(0)}K^{(0)} \Bigg[& \frac{3}{4}(1 + 2\xi)\left(\frac{V^{(0)}}{V}\right)^{4/3} \\ & -\frac{1}{2}\xi\left(\frac{V^{(0)}}{V}\right)^2 - \frac{3}{2}(1 + \xi)\left(\frac{V^{(0)}}{V}\right)^{2/3} + \frac{1}{2}\left(\xi + \frac{1}{2}\right)\Bigg] \end{aligned} \tag{5.4}$$

where the parameters $F^{(0)}$, $V^{(0)}$, $K^{(0)}$ and $\xi = 3(4 - K')/4$ are to be determined by fitting. For example, given $T_{\text{el}} = 6000$ K and $q = 1.60$ I obtain: $V^{(0)} = 10.7674\ \text{Å}^3$, $K^{(0)} = 23.94$ GPa, $K' = 4.4018$ and $F^{(0)} = -8.8747$ eV/atom. This is shown in fig. 5.4. By performing similar fits at a variety of temperatures I obtain the following fifth-order fits. Writing

$$V^{(0)}(T_{\text{el}}) \sum_{n=0}^{5} V_n^{(0)} T_{\text{el}}^n \tag{5.5}$$

and similarly for $K^{(0)}$, K' and $F^{(0)}$, I obtain

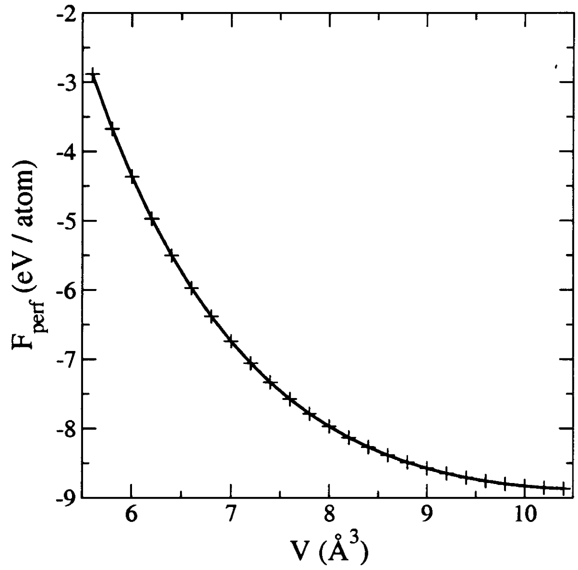

Figure 5.4: Calculated free energy for axial ratio of 1.60 and electronic temperature of 6000 K with Birch-Murnaghan fit. Crosses represent calculated free energy per atom, while the solid curve represents the Birch-Murnaghan fit.

$V_0^{(0)} = 10.2531\ \text{Å}^3 \qquad K_0^{(0)} = 29.12\ \text{GPa}$
$V_1^{(0)} = -1.06 \times 10^{-5}\ \text{Å}^3\ \text{K}^{-1} \qquad K_0^{(1)} = 3.43 \times 10^{-4}\ \text{GPa K}^{-1}$
$V_2^{(0)} = 1.93 \times 10^{-8}\ \text{Å}^3\ \text{K}^{-2} \qquad K_0^{(2)} = -4.46 \times 10^{-7}\ \text{GPa K}^{-2}$
$V_3^{(0)} = 1.05 \times 10^{-12}\ \text{Å}^3\ \text{K}^{-3} \qquad K_0^{(3)} = 3.48 \times 10^{-11}\ \text{GPa K}^{-3}$
$V_4^{(0)} = -1.67 \times 10^{-16}\ \text{Å}^3\ \text{K}^{-4} \qquad K_0^{(4)} = -4.37 \times 10^{-16}\ \text{GPa K}^{-4}$
$V_5^{(0)} = 5.03 \times 10^{-21}\ \text{Å}^3\ \text{K}^{-5} \qquad K_0^{(5)} = -2.37 \times 10^{-20}\ \text{GPa K}^{-5}$
$K_0' = 4.45 \qquad F_0^{(0)} = -8.14\ \text{eV atom}^{-1}$
$K_1' = -2.50 \times 10^{-5}\ \text{K}^{-1} \qquad F_1^{(0)} = -2.94 \times 10^{-7}\ \text{eV atom}^{-1}\ \text{K}^{-1}$
$K_2' = 2.71 \times 10^{-8}\ \text{K}^{-1} \qquad F_2^{(0)} = -1.25 \times 10^{-8}\ \text{eV atom}^{-1}\ \text{K}^{-2}$
$K_3' = -5.20 \times 10^{-12}\ \text{K}^{-1} \qquad F_3^{(0)} = -2.51 \times 10^{-12}\ \text{eV atom}^{-1}\ \text{K}^{-3}$
$K_4' = 4.44 \times 10^{-16}\ \text{K}^{-1} \qquad F_4^{(0)} = 2.49 \times 10^{-16}\ \text{eV atom}^{-1}\ \text{K}^{-4}$
$K_5' = -1.56 \times 10^{-20}\ \text{K}^{-1} \qquad F_5^{(0)} = -7.69 \times 10^{-21}\ \text{eV atom}^{-1}\ \text{K}^{-5}.$

This parameterization completely specifies the perfect lattice free energy as a function of volume and temperature for a fixed axial ratio $q = 1.60$. I now treat axial relaxation. For fixed volume $V = 6.97$ Å^3, $T_{\text{el}} = 6000$ K, I calculate the free energy for $1.55 \leq c/a \leq 1.70$ and compute the quantity ΔF_{perf} of (5.2). This yields the parameters $\alpha = 6.560$ eV and $q_1 = 1.6034$. The fit is shown in fig. 5.5. Repeating this procedure for temperatures 2000 K $\leq T_{\text{el}} \leq$ 8000 K and volumes 5.5 Å^3 $\leq V \leq$ 10.5 Å^3 yields the following parameters for in (5.3):

$a^{(0)} = 18.39\ \text{eV} \qquad a^{(1)} = -1.532\ \text{eV Å}^{-3}$
$b^{(0)} = -3.070 \times 10^{-4}\ \text{eV K}^{-1} \qquad b^{(1)} = 1.64908 \times 10^{-5}\ \text{eV K}^{-1}\ \text{Å}^{-3}$
$r^{(0)} = 1.63 \qquad r^{(1)} = -7.909 \times 10^{-3}\ \text{Å}^{-3}$
$s^{(0)} = -7.902 \times 10^{-6}\ \text{K}^{-1} \qquad s^{(1)} = 1.817 \times 10^{-6}\ \text{K}^{-1}\ \text{Å}^{-3}.$

This set of parameters, together with the parameters for the Birch-Murnaghan equation, suffice to specify $F_{\text{perf}}(V, q, T_{\text{el}})$ for the range of interest. In particular, by defining q_{min} to be that value of q which minimizes $F_{\text{perf}}(V, q, T_{\text{el}})$, we have $q_{\text{min}} = (q_0 + q_1)/2.$, and therefore, for given V, T_{el}

$$\Delta F(q_{\text{min}}) = -\frac{\alpha}{4}\left(q_1 - q_0\right)^2 \ . \tag{5.6}$$

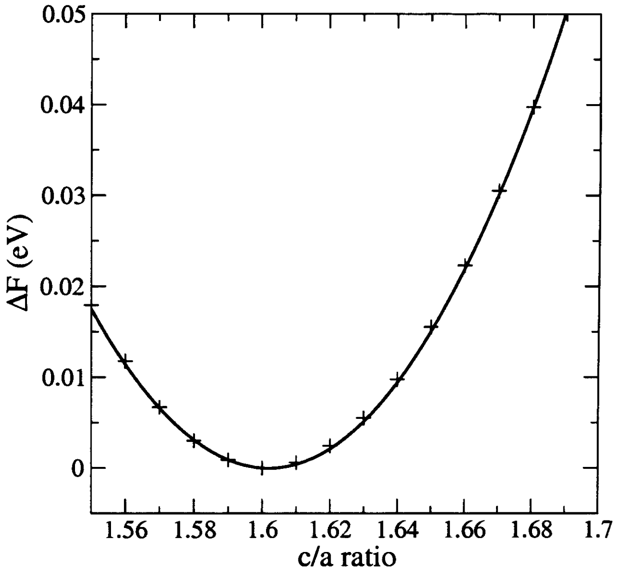

Figure 5.5: F(q)-F(1.60) with second order fit.

So the value of the perfect lattice free energy appropriate for calculating thermodynamic properties will be

$$F_{\text{perf}}(V, q_{\text{min}}, T_{\text{el}}) = F_{\text{perf}}(V, q_0, T_{\text{el}}) + \Delta F(V, q_{\text{min}}, T_{\text{el}}) \, . \qquad (5.7)$$

Substituting expressions (5.4) and (5.6) and differentiating with respect to volume allows us to plot the perfect lattice contribution to the thermodynamic pressure, including axial relaxation. In fig. 5.6 I show the pressure at zero temperature, and the perfect lattice contribution to the pressure at 2000, 4000 and 6000 K. The contribution to the pressure of axial relaxation is shown at zero temperature in fig. 5.7.

5.4 Vibrational free energy calculations

I calculate the contributions to the free energy due to lattice vibrations in the PIC approximation. To do this it is first necessary to find the coefficients of (3.125). These I compute for a variety of volumes at a fixed electronic

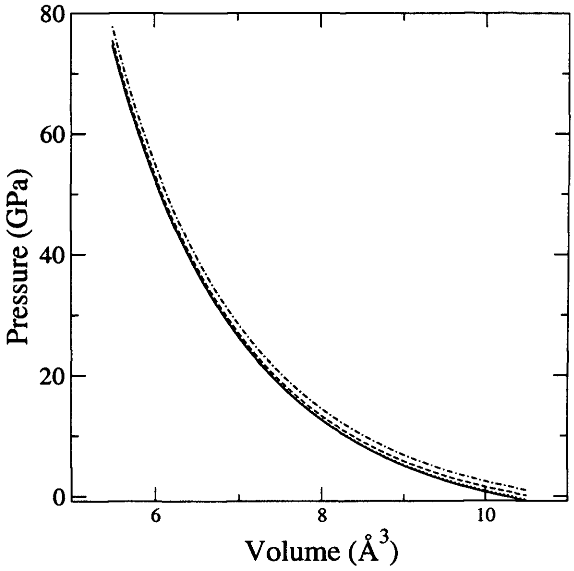

Figure 5.6: Pressure at zero temperature (solid line) and perfect lattice contributions at 2000 K, (dotted) 4000 K (dashed) and 6000 K (dot-dashed).

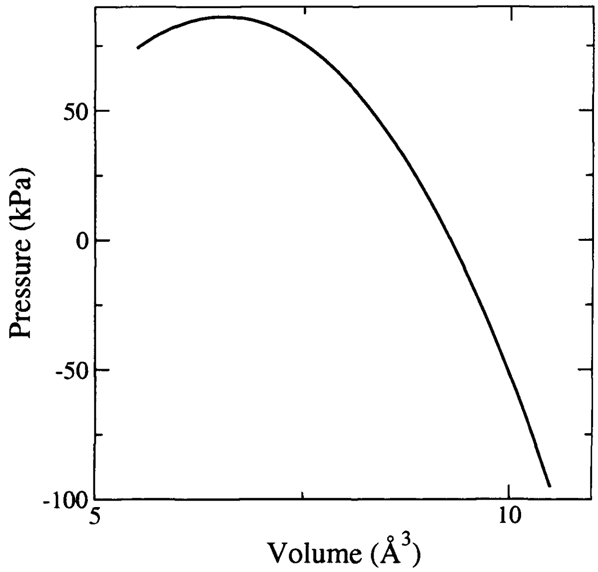

Figure 5.7: Change in pressure at 0 K due to relaxation of constraint $c/a = 1.6$.

temperature of $T_{el} = 6000$ K. I account for relaxation of the axial ratio to harmonic order only, as will be described below.

First it is necessary to define our axes with respect to the h.c.p. lattice. The x and y axes are taken to lie in the hexagonal plane, with the x axis directed towards the nearest neighbour atom, and the y perpendicular. The z axis is the hexagonal axis. Examining eq. (3.125), if a wanderer atom is displaced in the y direction, the potential will be given by

$$\phi_y(y) = K_a^{(2)} y^2 + K^{(3)} y^3 + K_a^{(4)} y^4 \,. \tag{5.8}$$

If the atom is displaced in the z direction, the potential is

$$\phi_z(z) = K_b^{(2)} z^2 + K_c^{(4)} z^4 \,. \tag{5.9}$$

Whereas if the atom is displaced a distance d in a direction such that $x = z = d/\sqrt{2}$, then the potential is

$$\phi_{xz}(d) = \frac{1}{2}\left(K_a^{(2)} + K_b^{(2)}\right) d^2 + \frac{1}{4}\left(K_a^{(4)} + K_a^{(4)} + K_a^{(4)}\right) d^4 \,. \tag{5.10}$$

5.4.1 Supercell size convergence and k points

For a volume of 6.97 Å^3 per atom, and an axial ratio of 1.60, and with an electronic temperature of 6000 K, I evaluate $\phi(\mathbf{R})$ for several supercells of dimension $2\times2\times1$ (eight atoms), $2\times2\times2$ (sixteen atoms) and $3\times3\times2$ (thirty-six atoms). All dimensions are expressed as multiples of the two-atom hcp cell. Because k-point sampling is highly converged for the two-atom cell with a $9 \times 9 \times 5$ grid, it is sufficient to demand that the sampling in the various supercell sizes be at least as good. In fact, I use: for the 8-atom cell, a $9 \times 9 \times 5$ grid; for the 16-atom cell, a $7 \times 7 \times 5$ grid; and for the 36-atom cell, a $3 \times 3 \times 3$ grid. In each case these equal or exceed the sampling used in the 2-atom cell.

The procedure used to test for supercell convergence is convergence of the quantity $\ln \bar{\omega}$ (3.129). It is therefore necessary only to displace the wanderer atom in the positive x and positive z directions, and compute the quantities

$$\phi_x(x) = \phi_x(-x) = \frac{1}{2} M\omega_a^2 x^2 + K_a^{(4)} x^4 \tag{5.11}$$

and

$$\phi_z(z) = \phi_z(-z) = \frac{1}{2} M\omega_b^2 z^2 + K_c^{(4)} z^4 \; . \tag{5.12}$$

Therefore the energy is calculated for ten displacements x and ten displacements z, ranging from 0.03 to 0.3 of the respective lattice parameter, and these are fitted to functions of the form

$$f(x) = a + bx^2 + cx^4 \; . \tag{5.13}$$

No supercell calculation is performed for $x = z = 0$, as the internal symmetry operations employed by VASP to improve the speed of calculations would results in a discontinuity at this point. Fig. 5.8 shows an instance of such a fit. Fig. 5.9 shows $\ln\bar{\omega}$ plotted as a function of $\ln(V/\text{Å}^3)$ for the three sets of cell dimension, along with Dario Alfè's *et al.* [34] calculations for $\ln\bar{\omega}$ of eq. (3.41) using the harmonic approximation, with full atomic correlation.

It is observed that the 16- and 36-atom values of $\ln\bar{\omega}$ differ only by an additive constant, which does not contribute to thermodynamics functions. Therefore, throughout the following, I use 36-atom supercells with $3 \times 3 \times 3$ Monkhorst-Pack sampling of the Brillouin zone.

5.4.2 Harmonic free energy

I have already computed $\ln\bar{\omega}$ for $q = 1.60$ as a function of volume for a 36-atom cell. I now wish to compute the correction $\Delta_{\mathrm{L}}\bar{\omega}(V,q) \equiv \ln\bar{\omega}(V,q) - \ln\bar{\omega}(V,q_0)$. Over the same range of volumes, and for $1.48 \leq q \leq 1.72$, I use the same procedure as above, to compute ω_a and ω_b. I fit to the expression

$$\Delta_{\mathrm{L}}\bar{\omega}(q) = \beta(q - q_0)(q - q_2) \tag{5.14}$$

where $\beta = \sum_{i=0}^{2} \beta^{(i)} V^i$ and similarly for q_2. These have the coefficients $\beta^{(0)} = -2.084$, $\beta^{(2)} = 0.375$, $\beta^{(0)} = -0.0264$, $q_2^{(0)} = 1.990$, $q_2^{(1)} = -0.141$

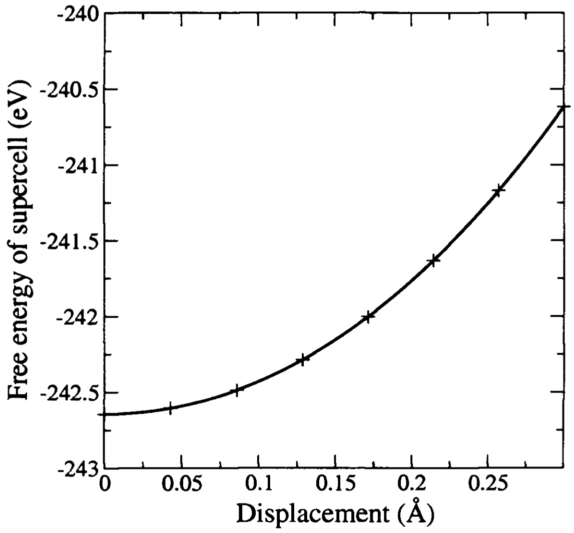

Figure 5.8: Free energy of 36 atom supercell at 6.97 Å^3, as a function of displacement of wanderer atom in the x direction.

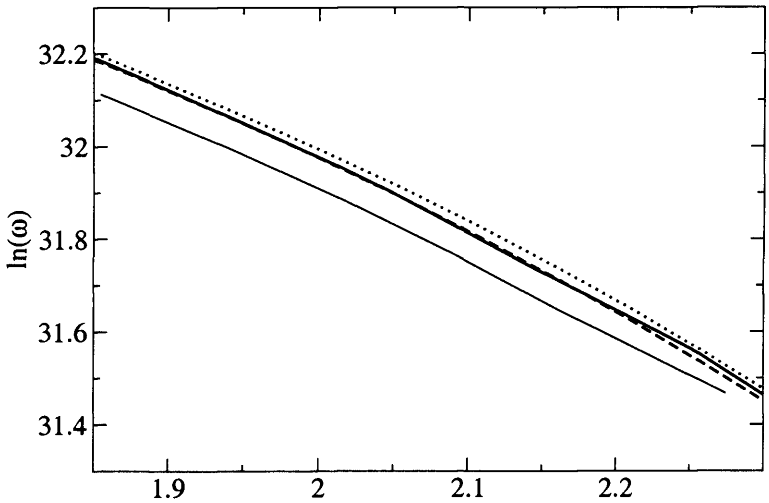

Figure 5.9: $\ln \bar{\omega}$ as a function of $\ln(V/\text{Å}^3)$ for 8-atom (solid curve), 16-atom (dashed curve) and 36-atom (dotted curve) supercells. The results of Alfè *et al.* are shown by the lighter curve.

and $q_2^{(2)} = 8.79 \times 10^{-3}$. Units are such that $\bar{\omega}$ is in rad s^{-1}, and V is in Å^3. This gives a full parameterization of the harmonic free energy within the PIC model as a function of V, q, T, given the approximation that T_{el} is fixed.

5.4.3 Anharmonic free energy

My tactic is as follows: for a fixed electronic temperature $T_{\mathrm{el}} = 6000$ K and c/a ratio $q = 1.60$, and for volumes in the range 5.2 to 11.4 Å^3 per atom, I fit $\phi(\mathbf{R})$, and find its coefficients. For a given temperature, I can then compute the PIC free energy per atom by calculating the partition function

$$\begin{gathered} z^{\mathrm{PIC}} = \int \mathrm{d}^3\mathbf{R} e^{-\beta\phi(\mathbf{R})} \\ 3k_{\mathrm{B}}T \ln \frac{\hbar\bar{\omega}}{k_{\mathrm{B}}T} + dT^2 + O\left(T^3\right) , \end{gathered} \tag{5.15}$$

where d is given by (3.143). z^{PIC} is then calculated by numerical quadrature at a set of temperatures from 2000 to 8000 K, and these results compared with the use of eq. (3.143). The results are shown in fig. 5.10 for a volume of 7.0 Å^3. As we see, for all temperatures below the melting point, there is strong agreement between these two techniques. I therefore compute d in terms of the coefficients of $\phi(\mathbf{R})$, and fit this as a function of volume. This function is shown in fig. 5.11, along with the same quantity computed by Alf'e *et. al* using thermodynamic integration. We immediately note that the PIC model gives the wrong sign, not only for the anharmonic free energy, but also for its first derivative with respect to volume. The coefficients of fit for d are $d^{(0)} = -6.556 \times 10^{-8}$ eV K^{-2}, $d^{(1)} = 3.399 \times 10^{-8}$ eV K^{-2} Å^{-3}, $d^{(2)} = -6.487 \times 10^{-9}$ eV K^{-2} Å^{-6}, $d^{(3)} = 5.400 \times 10^{-10}$ eV K^{-2} Å^{-9} and $d^{(4)} = -1.639 \times 10^{-11}$ eV K^{-2} Å^{-12}, where $d(V) = \sum_{i=0}^{4} d^{(i)} V^i$.

To recap, I have now computed all components of the free energy withing the PIC approximation as a function of temperature and volume for $q = 1.60$, and corrections as a function of axial ratio in the harmonic limit of the PIC.

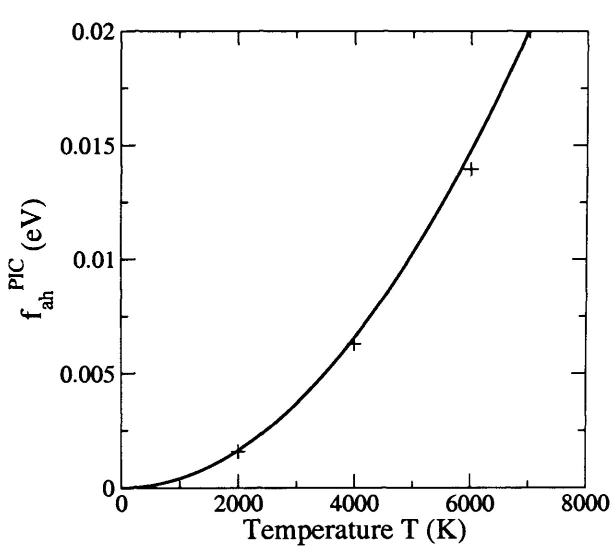

Figure 5.10: Anharmonic free energy per atom obtained using numerical quadrature (plus symbols) and Eq. (3.143) (curve) for an atomic volume of 7.0 Å^3.

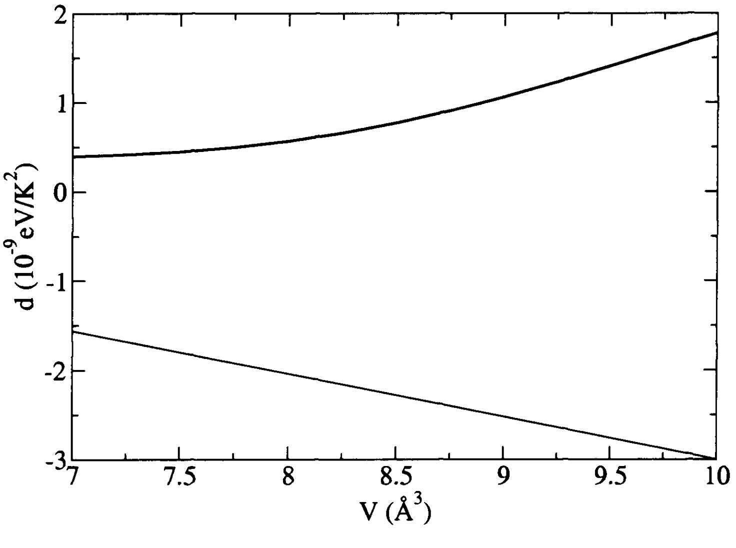

Figure 5.11: Coefficient d (see (3.143) and (5.15)) of the anharmonic free energy as a function of volume for this work (heavy curve) and Alfè *et al.* [34] light curve.

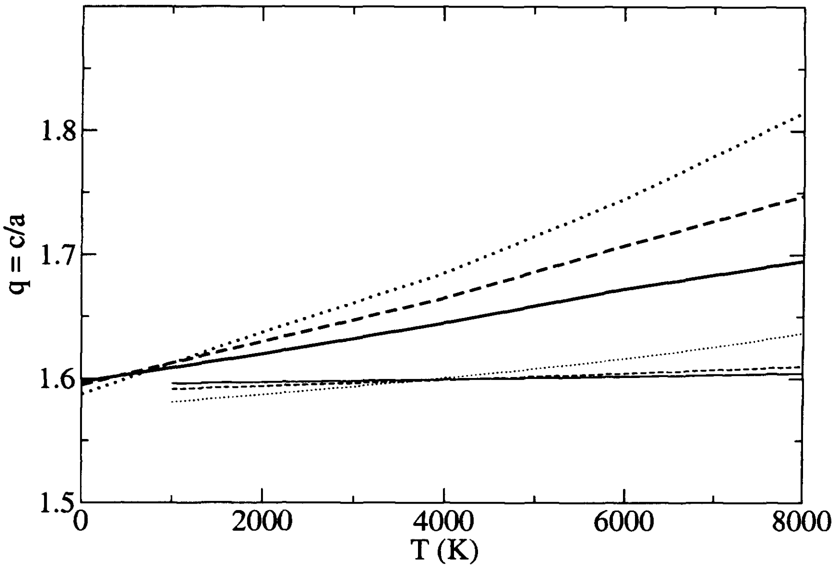

Figure 5.12: Equilibrium axial ratio q, for Steinle-Neumann *et al.* [35] (heavy curves) at atomic volumes of 6.81 Å^3 (solid curve), 7.11 Å^3 (dashed curve) and 7.41 Å^3 (dotted curve), and for the current work (light curves) at 5.5 Å^3 (solid curve), 7.5 Å^3 (dashed curve) and 10.0 Å^3 (dotted curve).

5.5 Aspect ratio in PIC

Before I compute thermodynamic functions in the PIC, I must compute the minimizing value of the axial ratio q. This is done by minimizing the total free energy correction, calculated using equations (5.6) and (5.14). This will yield the quantity $q_{\min}(V, T)$, which will be used when computing the free energy at a given V, T. $q_{\min}$ is shown as a function of V, T in fig. 5.12, along with results from Steinle-Neumann *et. al* [35]. We immediately see that the strong temperature dependence predicted by Steinle-Neumann *et. al* is not observed.

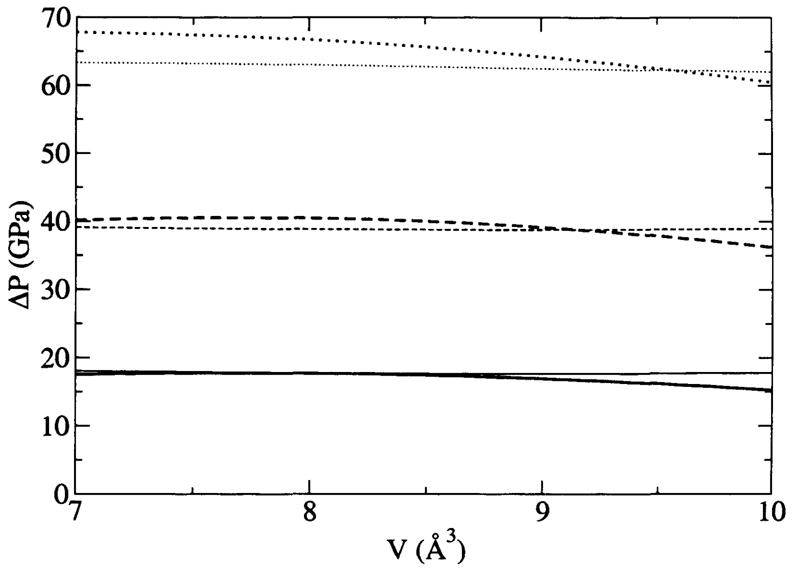

Figure 5.13: The total thermal pressure in this work (light curves) and that of Alfè *et. al* (heavy curves) at 2000 K (solid curve), 4000 K (dashed curve) and 6000 K (dotted curve) as a function of atomic volume.

5.6 Calculating thermodynamic functions

I now proceed to compute several thermodynamic functions of h.c.p. Fe, which may be compared with the results of Alfè *et. al* [34] and Wasserman *et. al* [36]. All the quantities computed here are defined in Sec. 3.1, and are calculated by analytical differentiation of the parameterized forms described above. First I show the thermal pressure $\Delta p(V,T) \equiv p(V,T) - p(V,0)$. This is contrasted with the results of Alfè *et. al* in fig. 5.13 The good agreement of these results reflects the ability of the PIC model to correctly compute the quantity $\ln \bar{\omega}$ to within an additive constant.

I now compute the internal energy $E(V,T)$, and the total energy $p(V,T)$. Using these, I can solve the Rankine-Hugoniot equation

$$\frac{1}{2}(p+p_0)(V_0 - V) = E - E_0 \qquad (5.16)$$

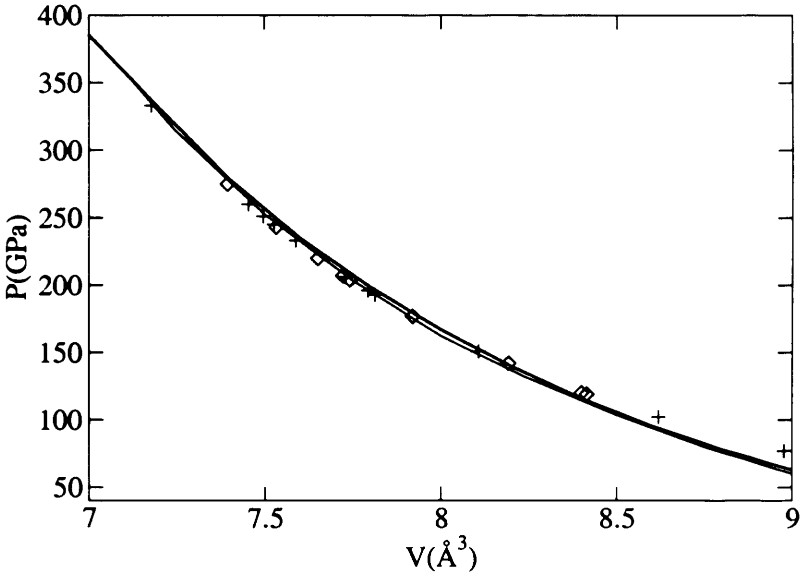

Figure 5.14: The pressure-volume Hugoniot. Heavy and light curves correspond to this work and Alfè *et. al* [34] respectively; symbols show the experimental results of Brown and McQueen [28].

to obtain the pressure-volume and temperature-pressure relations on the Hugoniot. The reference state for these experiments is ambient pressure, so $p_0 \approx 0$. V_0 and E_0 have been computed by Alfè at zero pressure and room temperature [34] using spin-polarized DFT molecular-dynamics calculations, and their values are $V_0 = 11.4342$ Å^3 per atom, and $E_0 = -8.11770$ eV. One therefore self-consistently solves the Rankine-Hugoniot equation with the known expressions for $p(V, T)$ and $E(V, T)$, which I do by using linear interpolation to make the quantity $\frac{1}{2}(p + p_0)(V_0 - V) - E + E_0$ equal zero, through varying either the temperature (for the p-V curve) or the volume (for the T-p curve. The results are shown in figs. 5.14 and 5.15. Also shown are the results of Alfè *et al.* [34], and the experimental results of Yoo *et al.* [77] and Brown and McQueen [28].

Finally I present, in figures 5.16, 5.17 and 5.18 respectively, calculations of the thermal expansivity, the product αK_T and the Grñeisen parameter, in

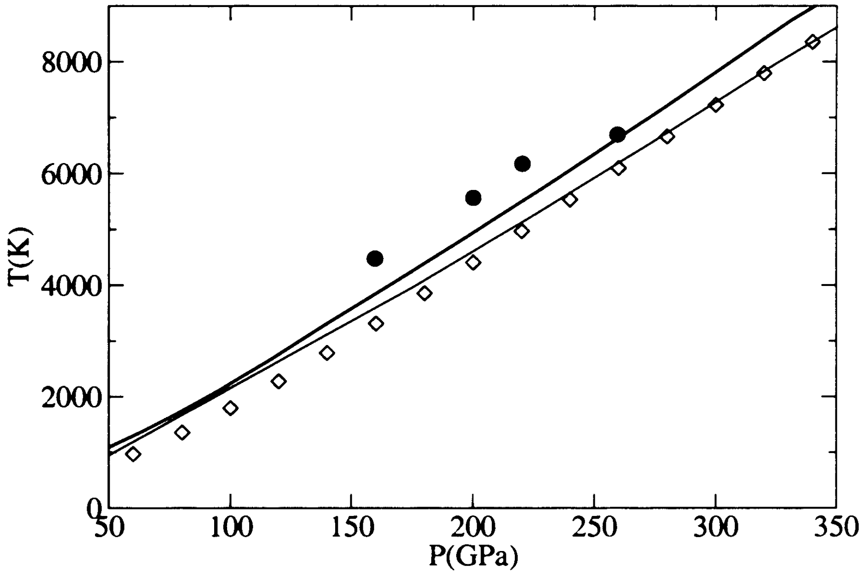

Figure 5.15: The temperature-pressure Hugoniot. Heavy and light curves correspond to this work and Alfè *et. al* [34] respectively; filled circles show the experimental results of Yoo *et al.* [77] and open diamonds are estimates due to Brown and McQueen [28].

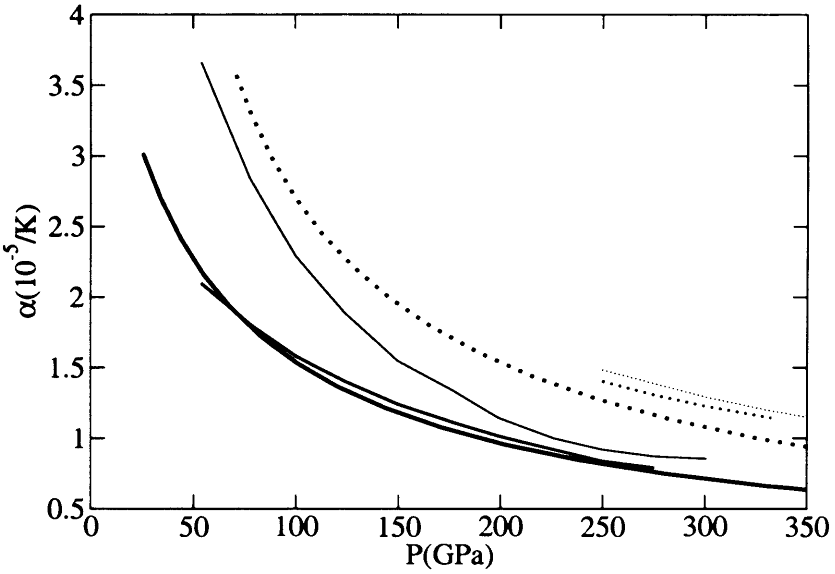

Figure 5.16: Thermal expansivity on isotherms at 2000 K (solid curves) and 6000 K (dotted curves). Heavy, medium and light curves correspond to this work, Alfè *et al.* [34] and Wasserman *et al.* respectively.

this work, that of Alfè *et al.* [34] and in the PIC calculations of Wasserman *et al.* [36].

5.7 Discussion

I have compared new PIC calculations of the thermodynamic properties of hcp Fe with those of Refs. [36] and [37], and with the more exact results of Ref. [34]. I have found that for a range of thermodynamic properties the PIC model gives excellent agreement with experimental results. A noteworthy example of this is that $p(V)$ on the Hugoniot agrees almost perfectly with the more exact results. My analysis of the free energy into different components makes clear why PIC is so good. The perfect-lattice component is exactly the same in the two approaches. for the harmonic component, the sole requirement for good results is that the logarithmic derivative $\mathrm{d}\ln\bar{\omega}/\mathrm{d}V$

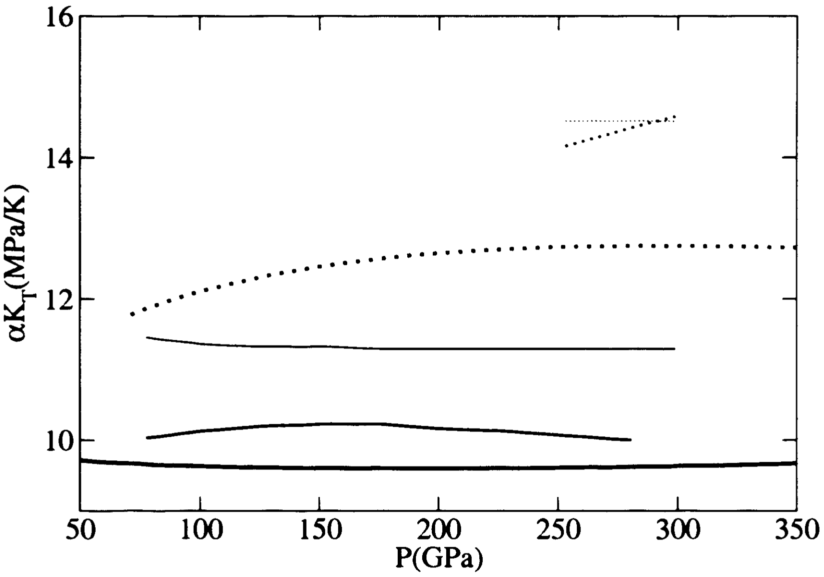

Figure 5.17: The product αK_T isotherms at 2000 K (solid curves) and 6000 K (dotted curves). Heavy, medium and light curves correspond to this work, Alfè *et al.* [34] and Wasserman *et al.* respectively.

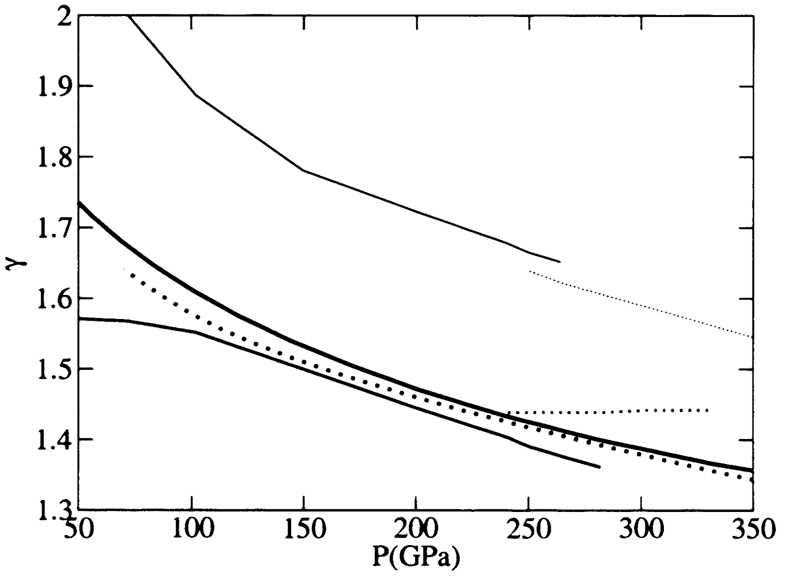

Figure 5.18: The Grüneisen parameter on isotherms at 2000 K (solid curves) and 6000 K (dotted curves). Heavy, medium and light curves correspond to this work, Alfè *et al.* [34] and Wasserman *et al.* respectively.

of the geometric mean frequency $\bar{\omega}$ be correct. But we have seen that for hcp Fe the PIC $\bar{\omega}$ differs from the $\bar{\omega}$ given by calculation of the full phonon spectrum by an almost constant factor over a wide range of volumes, so that this requirement is satisfied. The basic reason for this is that the phonon dispersion relations of hcp Fe scale by a uniform factor with changing volume (see Fig. 3 of [34]). Finally, the anharmonic component of free energy is very small, and has only a very minor effect on most thermodynamic functions. The reliability of PIC actually requires that anharmonic effects be small, since I have shown that the PIC approximation misrepresents these effects in predicting the wrong sign of the anharmonic free energy.

Surprisingly, even though PIC appears to be so good, I find important discrepancies with the earlier PIC results of [37] and [36]. In particular, my calculations of the thermodynamic Grüneisen parameter agree much more closely with the calculations of [34]. These discrepancies are clearly not due to PIC itself, but must come from other technical differences. We note that in the work of [36], the PIC calculations actually employed a tight-binding representation of the total energy function, the parameters in the tight-binding model being fitted to *ab initio* calculations. Conceivably, the tight-binding fit might have led to errors.

Even more surprising is that the strong increase with temperature of the axial c/a ratio predicted by recent PIC calculations is not reproduced at all by the present PIC work. According to [35], at the atomic volume of 7.11 Å^3, c/a increases from 1.63 to 1.75 as T goes from 2000 to 8000 K, whereas in the present PIC calculations at the similar volume of 7.0 Å^3, c/a increases only from 1.594 to 1.610 over the same temperature range. We shall see in Ch. 6 that the weak c/a variation found here is supported by harmonic calculations based on the full phonon spectrum of hcp Fe, and by *ab initio* molecular dynamics. As will be seen in Ch 7, this has direct consequences for the elastic anisotropy of the inner core.

These results shed light on the usefulness of the PIC approximation. Since we have seen that PIC cannot be relied on for anharmonic contributions, it should be regarded as a way of calculating the geometric-mean harmonic frequency $\bar{\omega}$. But PIC requires *ab initio* calculations on a periodic system in which a single atom is displaced from its perfect-lattice site. These are precisely the same calculations that are performed in order to obtain the force-constant matrix used to compute the full phonon spectrum ([34, 78]). For an *ab initio* method that yields forces on all ions – which includes the pseudopotential and PAW implementations of DFT, among others – the net result of the PIC procedure is to discard all the information contained in the ionic forces, retaining only the variation of total energy with displacement. This suggests that it may be better to use the force information to compute the force-constant matrix and hence the full phonon spectrum, rather than adopting the PIC approach.

Noi divenimmo intanto a piè del
monte; quivi trovammo la
roccia sì erta, che 'ndarno vi
sarien le gambe pronte.

Dante Alighieri (1265–1321)

Chapter 6

The aspect ratio of hcp Fe

6.1 Introduction

In the last chapter, I showed that my particle-in-cell calculations did not reproduce the strong temperature dependence in the c/a axial ratio, observed by Steinle-Neumann *et al.* [35]. This quantity is central to our understanding of the elasticity of the inner core, and its elastic anisotropy in particular, and this discrepancy must be addressed. Therefore, in this chapter I apply both harmonic and molecular-dynamics calculations to determining the behaviour of the axial ratio of h.c.p. Fe, free from the approximations of the PIC method.

The remainder of this chapter is organized as follows. In sec. 6.2, I show my calculations of aspect ratio at zero temperature, plotted against the recent diffraction measurements of Ma *et al.* [79], performed at ambient temperature. In sec. 6.3 I describe the technical challenges of performing my harmonic calculations, and present the results of various convergence tests, and my harmonic calculations of axial ratio. In sec. 6.4 I describe harmonic and molecular dynamics calculations in the embedded-atom model, which I use to perform convergence tests for my molecular dynamics calculations. Finally, in sec. 6.5, I present results for my *ab initio* molecular dynamics calculations. My results for the behaviour of the axial ratio will be contrasted with those of Steinle-Neumann *et al.* [35], and with recent diffraction measurements due to Ma *et al.* [79]. Results will be discussed in sec. 6.6. These results appear in Ref. [80].

6.2 Zero-temperature calculations

In ch. 5 I described extensive calculations of the perfect-lattice free energy as a function of volume, electronic temperature, and axial ratio. By extrapolation to zero temperature, and minimization with respect to c/a, I easily obtain the zero-temperature equilibrium axial ratio as a function of atomic volume. This, in conjunction with the perfect-lattice equation of state described in ch. 5 immediately yields the results shown in fig. 6.1. Also shown are the diffraction measurements of Ma *et al.* [79]. I refer the reader to ch. 5 for further details.

6.3 Harmonic calculations

6.3.1 Free energies, minimization, and stresses

The intention of my harmonic calculations will be to make calculations of the logarithmic mean phonon frequency $\bar{\omega}$ as a function of temperature, volume, and axial ratio c/a. Here $\bar{\omega}$ is not that obtained in the PIC model, but the logarithmic average over all branches and reciprocal lattice vectors

$$\ln \bar{\omega} \equiv \frac{1}{N_{\mathbf{k}j}} \sum_{\mathbf{k}j} \ln \omega_{\mathbf{k}j} , \tag{6.1}$$

giving a harmonic vibrational contribution per atom to the free energy of

$$f_{\mathrm{vib}} = 3k_{\mathrm{B}}T \ln \frac{\hbar\bar{\omega}}{k_{\mathrm{B}}T} . \tag{6.2}$$

The total free energy per atom in the harmonic limit $f_{\mathrm{harm}} = f_{\mathrm{perf}} + f_{\mathrm{vib}}$ is now calculated. This can be directly minimised as a function of c/a to

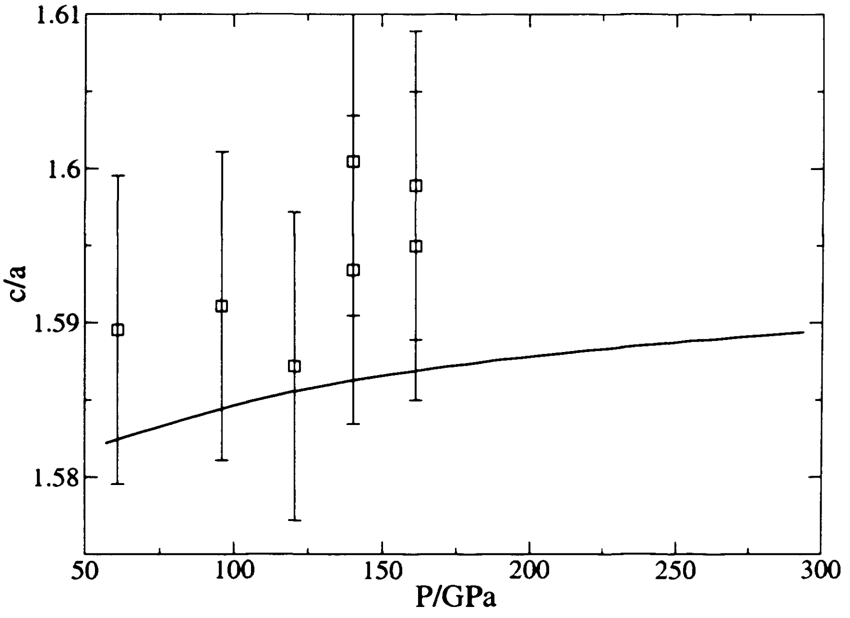

Figure 6.1: Calculated axial ratio c/a as a function of pressure (solid curve), compared with the diffraction measurements of Ma *et al.* [79] (data points).

calculate the equilibrium axial ratio in the harmonic limit, or, by taking the derivative $(\partial f_{\mathrm{harm}}/\partial q)_{V,T}$, I can compare my calculations with fully anharmonic stresses computed using molecular dynamics. To see this, I write down the lattice parameters

$$a = \left(\frac{4V}{q\sqrt{3}}\right)^{\frac{1}{3}}, \qquad c = \left(\frac{4Vq^2}{\sqrt{3}}\right)^{\frac{1}{3}} \tag{6.3}$$

in the basal and hexagonal axes respectively. Then

$$\left(\frac{\partial \varepsilon_{11}}{\partial q}\right)_V = \frac{1}{a}\left(\frac{\partial a}{\partial q}\right)_V = -\frac{1}{3q} \tag{6.4}$$

and

$$\left(\frac{\partial \varepsilon_{33}}{\partial q}\right)_V = \frac{1}{c}\left(\frac{\partial c}{\partial q}\right)_V = \frac{2}{3q}\,. \tag{6.5}$$

Thus we obtain

$$\begin{aligned}
\mathrm{d}F &= \frac{\partial F}{\partial \varepsilon_{11}}\mathrm{d}\varepsilon_{11} + \frac{\partial F}{\partial \varepsilon_{22}}\mathrm{d}\varepsilon_{22} + \frac{\partial F}{\partial \varepsilon_{33}}\mathrm{d}\varepsilon_{33} \\
\Rightarrow \quad \frac{1}{V}\left(\frac{\partial F}{\partial q}\right)_V &= \sigma_{11}\left(\frac{\partial \varepsilon_{11}}{\partial q}\right)_V + \sigma_{22}\left(\frac{\partial \varepsilon_{22}}{\partial q}\right)_V + \sigma_{33}\left(\frac{\partial \varepsilon_{33}}{\partial q}\right)_V \\
&= \frac{2}{3q}\left(\sigma_{33} - \sigma_{11}\right) \\
\Rightarrow \quad \sigma_{33} - \sigma_{11} &= \frac{3q}{2V}\left(\frac{\partial F}{\partial q}\right)_V .
\end{aligned} \tag{6.6}$$

This quantity $\sigma_{33} - \sigma_{11}$ can also be directly computed in the molecular dynamics calculations, and compared with the harmonic results of this section. It will go to zero at the equilibrium axial ratio.

6.3.2 Technical convergences

I now report the results of technical tests of k-point sampling and cell size convergence for my harmonic calculations. k-point convergence tests for the perfect lattice potential were performed in ch. 5, and I use identical sampling here. As in that chapter, I perform size convergence tests by insisting that k-point sampling in supercells be at least as dense as that value chosen for the perfect lattice calculations. Once size convergence tests are completed, I can again perform k-point sampling tests on my chosen supercell. My criterion is that free energies be converged to within 1 meV/atom.

Brillouin zone integration

The quantity that must be made converged is the mean vibrational frequency $\bar{\omega}$. To converge f_{vib} to within 1 meV, given $k_{\mathrm{B}}T \sim 0.1eV$, implies that $\ln\bar{\omega}$ be converged to within an absolute range of ± 0.001, or equivalently that $\bar{\omega}$ be converged to within 0.1%. $\bar{\omega}$ is obtained by solving the secular equation (3.52) for $\omega_{\mathbf{q}j}$ at a set of points $\{(\mathbf{q}, j)\}$ in the Brillouin zone. Note the change in notation for reciprocal space point, to distinguish from electronic k-point sampling: I will use $\mathbf{q}$ to denote points in the reciprocal space of the lattice for computation of $\bar{\omega}$. Calculation of $\bar{\omega}$ then requires only the specification of the full force-constant matrix $\Phi^{\mathbf{L}}_{s\mu,s'\nu}$. As we have seen, all atoms in the h.c.p. crystal are equivalent, and as demonstrated in Sec. 3.4.2, the x and y directions in the lattice are identical to second order in the cell potential; therefore $\Phi^{\mathbf{L}}_{s\mu,s'\nu}$ may be calculated by performing only two atomic displacements — in the x and in the z directions — and calculating the forces on all the remaining atoms of the supercell. The computation of the $\omega_{\mathbf{k}j}$, and the logarithmic average $\bar{\omega}$ are performed using the PHON program [81] by Dario Alfè. It should be noted here that, due to the comparatively inexpensive nature of these calculations, it is an easy matter to achieve convergence of $\bar{\omega}$ with respect to $\mathbf{q}$-point sampling, and we note here that a grid of 12 × 12 × 12 points is used throughout.

Small displacement

In order to calculate the force constants, it is necessary to make small displacements of one of the atoms of the supercell. The obvious question is how great these displacements should be. Large displacements will introduce errors due to anharmonic terms in the potential; however smaller displacements will results in much smaller forces, susceptible to numerical error. In fig. 6.2 I show $\bar{\omega}$ calculated in a 54-atom cell using $T_{\mathrm{el}} = 1000$ K and electronic k-point sampling on a $3 \times 3 \times 2$ Monkhorst-Pack grid. It is clear from these results that the value of $\bar{\omega}$ converges to a zero-displacement ideal, before being dominated by numerical errors. One can see that a displacement of 0.01 Å minimizes anharmonic effects while being outside of this 'noisy' regime. This value of displacement, which was also used in earlier calculations due to Alfè *et al.* [34] is employed throughout the remainder of my harmonic calculations.

k-point sampling and supercell size

The following convergence tests were performed at an electronic temperature of 1000 K; recall the discussion of ch. 5 regarding the effects of electronic

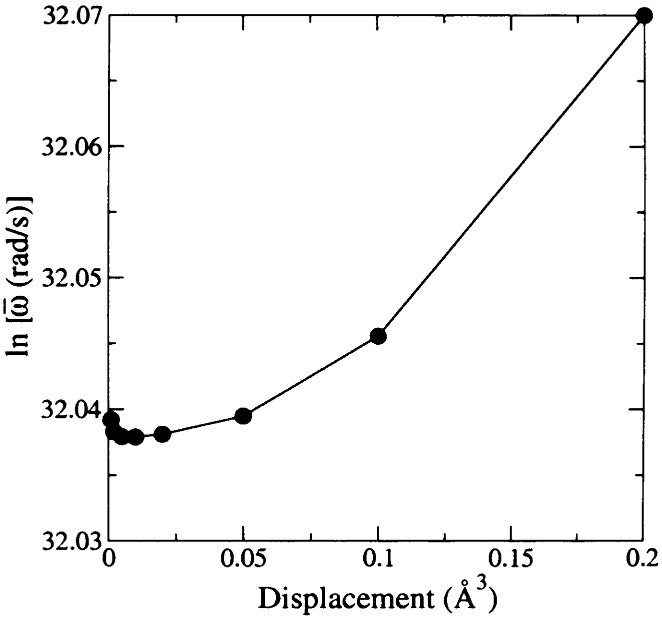

Figure 6.2: $\bar{\omega}$ calculated using different values of displacement

temperature (Fermi-surface smearing) on k-point sampling. The strategy for ensuring convergence simultaneously with respect to k-point sampling and supercell size is as follows.

First, I choose a 16-atom cell (2-atom cell times $2 \times 2 \times 2$). For this cell I obtain convergence of $\bar{\omega}$ to within 0.1% with respect to k-point sampling. Then, using an at least equivalently fine sampling for each cell, I converge $\bar{\omega}$ with respect to cell size. Having chosen a suitable cell size, I then perform again k-point convergence tests for this cell. The results of these calculations are shown in tables 6.1–6.3. For each calculation, volume is 6.97 Å^3, $c/a =$ 1.60.

We can see from table 6.1 that for a Monkhorst-Pack $4 \times 4 \times 3$ grid, $\ln \bar{\omega}$ is converged to within 0.0001, or equivalently, $\bar{\omega}$ is converged to within 0.01%, well within my convergence criteria. Table 6.2 shows the value of $\bar{\omega}$ for each cell size, along with the k-point sampling used for that cell, and the equivalent sampling for the 16-atom cell. As can be seen this equivalent

k-point grid	$\ln\bar{\omega}$	k-point grid	$\ln\bar{\omega}$
$1\times1\times1$	31.88568	$5\times5\times3$	31.96513
$2\times2\times1$	31.97660	$6\times6\times4$	31.96509
$3\times3\times2$	31.96282	$7\times7\times5$	31.96508
$4\times4\times3$	31.96513		

Table 6.1: 16-atom results

Atoms	k-point grid	$\ln\bar{\omega}_N$	16-atom sampling	$\ln\bar{\omega}_{16}^{(N)}$	$\ln(\bar{\omega}_N) - \ln(\bar{\omega}_{16}^{(N)})$
36	$4\times4\times3$	32.02373	$6\times6\times3$	31.98038	0.04335
54	$4\times4\times2$	32.03064	$6\times6\times3$	31.98038	0.05026
96	$2\times2\times2$	32.03080	$4\times4\times3$	31.98093	0.04987
128	$2\times2\times2$	32.03285	$4\times4\times4$	31.98517	0.04768
150	$2\times2\times2$	32.03542	$5\times5\times3$	31.97956	0.05586

Table 6.2: Size convergence

k-point grid	$\ln\bar{\omega}$
$1\times1\times1$	31.82439
$2\times2\times1$	31.98294
$3\times3\times2$	32.03804
$4\times4\times2$	32.03023

Table 6.3: 54-atom results

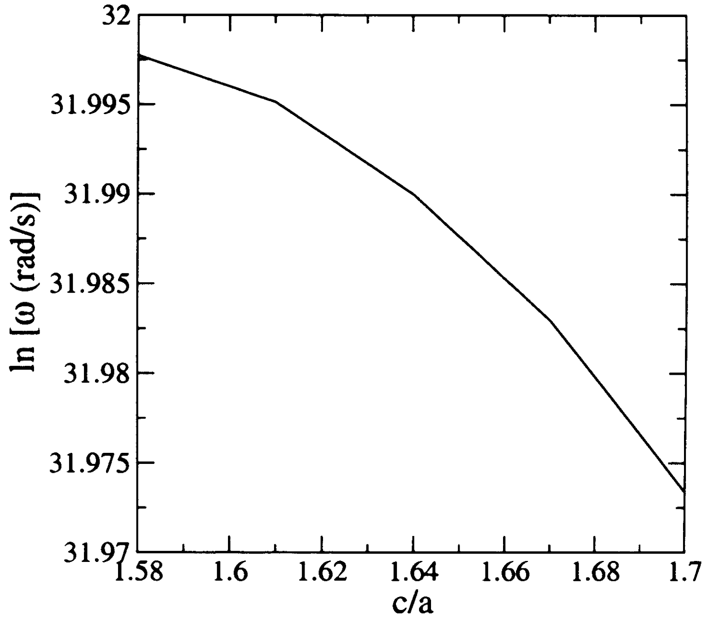

Figure 6.3: $\bar{\omega}$ as a function of c/a for 6.97 Å^3 and 6000 K.

sampling is always at least $4 \times 4 \times 3$. I exceed my convergence criterion for the 54-atom cell (2-atom cell times$3 \times 3 \times 3$). Finally, table 6.3 shows that for the 54-atom cell, a $3 \times 3 \times 2$ Monkhorst-Pack sampling grid satisfies my convergence criterion.

In summary, I employ throughout my harmonic calculations, a 54-atom cell, a 0.01 Å displacement and a $3 \times 3 \times 2$ Monkhorst-Pack grid for electronic k-point sampling.

6.3.3 Harmonic results for equilibrium axial ratio

Using the above parameters I calculated $\bar{\omega}$ at atomic volumes of 6.97, 7.50 and 8.67 Å^3, for c/a from 1.58 to 1.70 in steps of approximately 0.03, and for electronic temperatures of 2000, 4000 and 6000 K. This is shown in fig. 6.3 for 6.97 Å^3 and 6000 K. Adding this to the perfect lattice results I can immediately minimize with respect to c/a to obtain the equilibrium axial ratio as a function of temperature. This is shown in fig 6.4, along with my

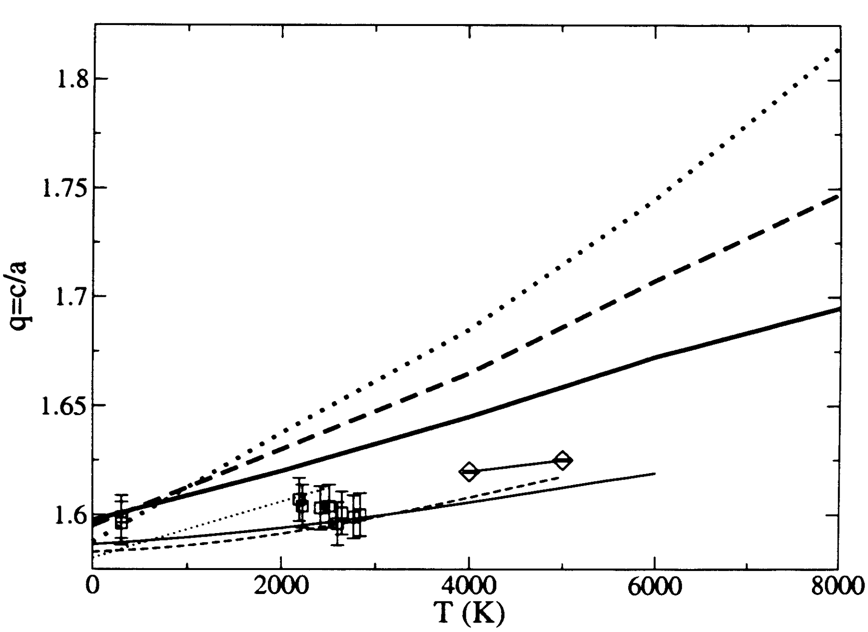

Figure 6.4: Calculated equilibrium axial ratio as a function of temperature for different volumes. For this work (light curves), atomic volumes are 6.97 Å^3 (solid curve), 7.50 Å^3 (dashed curve) and 8.67 Å^3 (dotted curve). For the results of Steinle-Neumann *et al.* [35] (heavy curves), volumes are 6.81 Å^3 (solid curve), 7.11 Å^3 (dashed curve) and 7.41 Å^3 (dotted curve). Also shown are diffraction measurements due to Ma *et al.* [79] at 7.73 Å^3/atom (open squares with error bars) and my own *ab initio* MD calculations at 6.97 Å^3 (diamonds).

molecular dynamics results, which will be discussed shortly.

Finally I discuss constraints on the effect of quantum mechanical corrections to the free energy of lattice vibrations. At zero temperature, the zero-point contribution to the energy per atom is (Sec. 3.2.6)

$$F_{\mathrm{ZP}} = \sum_{\mathbf{k}j} \hbar\omega_{\mathbf{k}j} \,. \tag{6.7}$$

Using my calculated phonon frequencies, this energy has been calculated as a function of q at $V = 6.97$ Å^3. Differentiated, this yields a contribution to the stress difference $\sigma_{33} - \sigma_{11}$, which varies from -230 MPa at $q = 1.58$ to -910 MPa at $q = 1.70$. This shifts the equilibrium axial ratio by no more than 0.001, as will be discussed in Sec. 6.5; and it is expected that this contribution will become even smaller as temperature increases.

6.4 Molecular dynamics and harmonic calculations in the embedded-atom model

6.4.1 The embedded-atom potential

I have described how harmonic and molecular dynamics calculations can be directly compared through the stress component $\sigma_{33} - \sigma_{11}$. Now I introduce a parameterized embedded-atom potential, which has previously been used to perform high-quality calculations of the properties of Earth's core Fe [82]. I will use this model to perform tests on statistical and system-size errors in my molecular dynamics calculations.

In the embedded atom model (EAM), the total energy of a system of N atoms is represented as the sum of two contributions. First, an empirical, repulsive pair potential, and secondly, a sum of embedding energies for each atom, representing the response of the electron density to the introduction of an atom:

$$E_{\text{tot}} = E_{\text{pair}} + E_{\text{embed}}$$

$$E_{\text{tot}} = E_{\text{pair}} + E_{\text{embed}}$$

$$\begin{aligned} E_{\text{pair}} &= \frac{1}{2} \sum_{i \neq j} \phi(|\mathbf{r}_i - \mathbf{r}_j|) \\ E_{\text{embed}} &= \sum_i f(\rho_i) \\ \rho_i &= \sum_{j(\neq i)} \psi(|\mathbf{r}_i - \mathbf{r}_j|) \end{aligned} \tag{6.8}$$

where $\phi(r)$ and $\psi(r)$ have the inverse power forms

$$\phi(r) = \epsilon \left(\frac{a}{r}\right)^n \quad \text{and} \quad \psi(r) = \left(\frac{a}{r}\right)^m , \tag{6.9}$$

and $f(\rho_i) = -\epsilon C(\rho_i)^{\frac{1}{2}}$. Here $f(\rho_i)$ represents the energy of embedding of atom i in an electron density ρ_i, given in turn as a sum of the functions ψ, each centred on an atom j. The inverse-power form of ψ may be simply regarded as an effective approximation to the true behaviour of the electron density due to atom j, while the square-root dependence of the embedding energy $f(\rho_i)$ is shown [83] to arise from the second-moment approximation to tight binding theory. In practice, both ϕ and ψ are cut off smoothly by making the transformation

$$\phi(r) \rightarrow \phi_{\mathrm{SF}}(r) = \begin{cases} \phi(r) + \beta + \gamma r & r < r_0 \\ \alpha(r_1 - r)^3 & r_0 < \ r < r_1 \\ 0 & r_1 < \ r \end{cases} , \tag{6.10}$$

where r_0 and r_1 are cutoff radii, with α, β and γ chosen such that ϕ, ϕ' and ϕ'' are continuous at r_0. The form guarantees that these three functions are also continuous at r_1. In the present calculations, I use $r_1 = 7$ Å, $r_0 = 0.9 r_1$. The parameters have been modified somewhat from those given by [82], in order to reproduce better the *ab initio* molecular dynamics simulations of Dario Alfè on solid and liquid Fe ([34, 78]). The parameters I use are: $n = 5.93$, $m = 4.788$, $\epsilon = 0.1662$ eV, $a = 3.4714$ Å and $C = 16.55$.

I need to calculate forces and stresses. The force, $\mathbf{f}_i$, acting on the i^{th} atom is given by

$$\mathbf{f}_i \equiv -\nabla_i E_{\mathrm{tot}} \ . \tag{6.11}$$

Having made made the smoothing transformation described above, this gives the two contributions

$$\begin{aligned} \mathbf{f}_i^{\mathrm{pair}} &\equiv -\nabla_i E_{\mathrm{pair}} \ . \\ &= -\sum_j \frac{\phi'_{\mathrm{SF}}(|\mathbf{r}_i - \mathbf{r}_j|)}{|\mathbf{r}_i - \mathbf{r}_j|}(\mathbf{r}_i - \mathbf{r}_j) \ . \end{aligned} \tag{6.12}$$

and

$$\begin{aligned}\mathbf{f}_i^{\text{embed}} &\equiv -\nabla_i E_{\text{embed}} \cdot \\ &= -\sum_j \left[f'(\rho_i) + f'(\rho_j)\right] \frac{\psi'_{\text{SF}}(|\mathbf{r}_i - \mathbf{r}_j|)}{|\mathbf{r}_i - \mathbf{r}_j|}(\mathbf{r}_i - \mathbf{r}_j) \,.\end{aligned} \tag{6.13}$$

Here $f'(\rho_i) = -\epsilon C \rho_i^{-1/2}/2$. Similarly, the stresses are given by

$$\begin{aligned}\langle \sigma_{\mu\nu} \rangle &= \frac{1}{V}\frac{\partial F}{\partial \varepsilon_{\mu\nu}} \\ &= \frac{1}{V}\left[-Nk_{\text{B}}T\delta_{\mu\nu} + \left\langle \frac{\partial E_{\text{pair}}}{\partial \varepsilon_{\mu\nu}} \right\rangle + \left\langle \frac{\partial E_{\text{embed}}}{\partial \varepsilon_{\mu\nu}} \right\rangle\right] \,.\end{aligned} \tag{6.14}$$

where

$$\frac{\partial E_{\text{embed}}}{\partial \varepsilon_{\mu\nu}} = \frac{1}{2}\sum_{i\neq j} \frac{\phi'_{\text{SF}}(|\mathbf{r}_i - \mathbf{r}_j|)}{|\mathbf{r}_i - \mathbf{r}_j|}(\mathbf{r}_i - \mathbf{r}_j)_\mu(\mathbf{r}_i - \mathbf{r}_j)_\nu \tag{6.15}$$

and

$$\frac{\partial E_{\text{embed}}}{\partial \varepsilon_{\mu\nu}} = \sum_{i\neq j} f'(\rho_i)\frac{\psi'_{\text{SF}}(|\mathbf{r}_i - \mathbf{r}_j|)}{|\mathbf{r}_i - \mathbf{r}_j|}(\mathbf{r}_i - \mathbf{r}_j)_\mu(\mathbf{r}_i - \mathbf{r}_j)_\nu \,. \tag{6.16}$$

We now have the tools necessary to perform harmonic and molecular dynamics calculations in the smoothed EAM. We note that the form of smoothing chosen ensures that the energy is continuous to third order — that is, the forces are continuous to second order. This is necessary, in order to prevent discontinuities in the plots of $\bar{\omega}$ vs c/a, which caused significant difficulties in the early stages of this work, when I tried to fit and differentiate these plots.

6.4.2 Embedded-atom calculations

Length of run

Fig. 6.5 shows the quantity $\sigma_0 \equiv \sigma_{33} - \sigma_{11}$ computed along a molecular dynamics trajectory $\Gamma(t)$. The simulation cell contains 96 atoms, the atomic volume is 6.97 Å^3, the temperature is 4000 K and $c/a = 1.65$. Shown are the

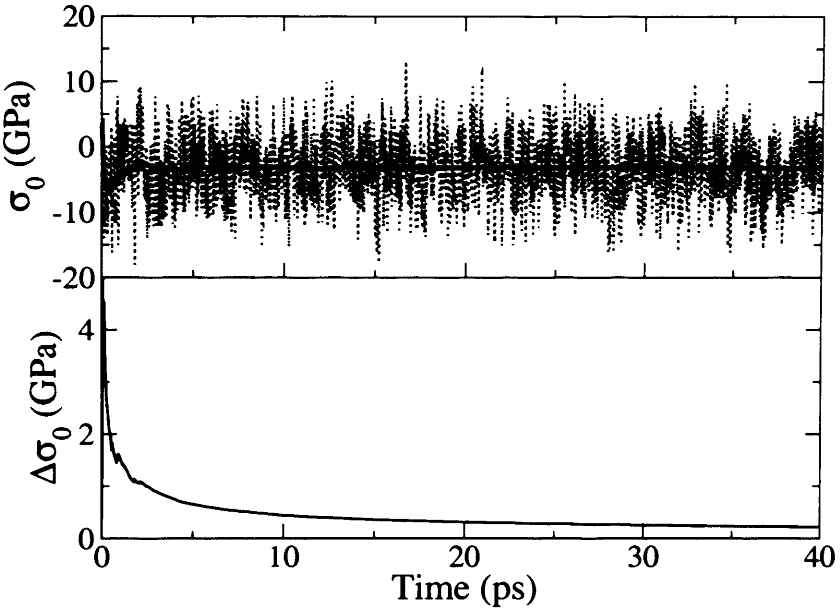

Figure 6.5: Instantaneous (dotted curve) and average (solid) value of $\sigma_0 = \sigma_{33} - \sigma_{11}$ (upper plot) and standard error (lower plot) computed on a 40 ps, 96-atom MD trajectory in the EAM, using $V = 6.97$ Å^3, $T = 4000$ K and $c/a = 1.65$.

instantaneous value $\sigma_0(\Gamma(t))$, the running average $\langle\sigma_0\rangle_t$, and the statistical error $\Delta\sigma_0(t)$, where

$$\langle\sigma_o\rangle_t = \frac{1}{t}\int_0^t \mathrm{d}s\sigma_0(\Gamma(s)) \tag{6.17}$$

and

$$(\Delta\sigma_0(t))^2 = \frac{\tau}{t}\left[\langle\sigma_o^2\rangle_t - \langle\sigma_o\rangle_t^2\right] . \tag{6.18}$$

Here τ is a characteristic correlation time for the system; however in practice, $\Delta\sigma_0(t)$ is calculated by taking block averages of the form

$$\frac{1}{\Delta t}\int_t^{t+\Delta t} \mathrm{d}s\sigma_0(\Gamma(s)) \tag{6.19}$$

and computing the standard error among such block averages in the limit $\Delta t \to \infty$. It should be further noted, that prior to the time 0, the system has been allowed to equilibrate for 1 ps.

This run demonstrates that to reduce r.m.s. statistical errors to within 1 GPa, for example, requires a run of length 3–4 ps. The r.m.s. error on any run may be inferred since this depends on the length of run as $T^{-1/2}$.

Size effects

To test the effect of supercell size, I performed further 15 ps runs for 54, 96, 128 and 150-atom supercells, again at 4000 K. The time-averaged values of σ_0 are shown, with statistical error bars, in fig. 6.6. It can be seen that for a system of 96 atoms, the error due to size effects is within approximately 0.6 GPa. The r.m.s. bear out the statistical mechanical result that $\Delta\sigma$ should depend on the number of atoms as $N^{-1/2}$. It can be inferred from these results that for a 1.5 ps average, for example, $\Delta\sigma_0$ falls from 2 GPa for a 54-atom cell, to 1 GPa for a 150-atom cell.

It follows that in order to calculate $\sigma_{33} - \sigma_{11}$ to a tolerance needed to determine the equilibrium axial ratio to within ±0.005, it suffices to perform *ab initio* molecular dynamics simulations of 1 ps on 96 atoms.

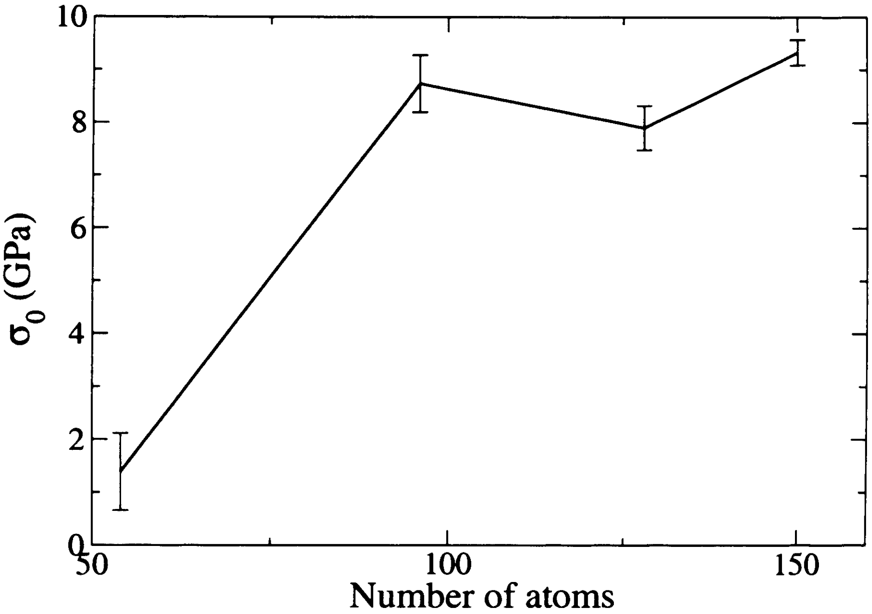

Figure 6.6: 15 ps time-averaged calculations of $\sigma_0 = \sigma_{33} - \sigma_{11}$ for a variety of cell sizes within the embedded-atom model.

Anharmonicity

As a test of my proposed method for comparing harmonic and molecular dynamics calculations, I calculate σ_0 for a range of temperatures for $V = 6.97$ Å^3, $c/a = 1.70$. The deliberately large value of c/a is chosen to to provide a large value of σ_0. The observed variation of σ_0 with temperature is very gradual in the embedded-atom model, so longer runs of 5 ps are used. Cell sizes are converged within the limits described above.

Results of these calculations are shown in fig. 6.7. The computed values of σ_0 clearly differ due to anharmonicity; the very important observation is that, in accordance with thermodynamic predictions, the harmonic results are tangential to the fully anharmonic md calculations at 0 K.

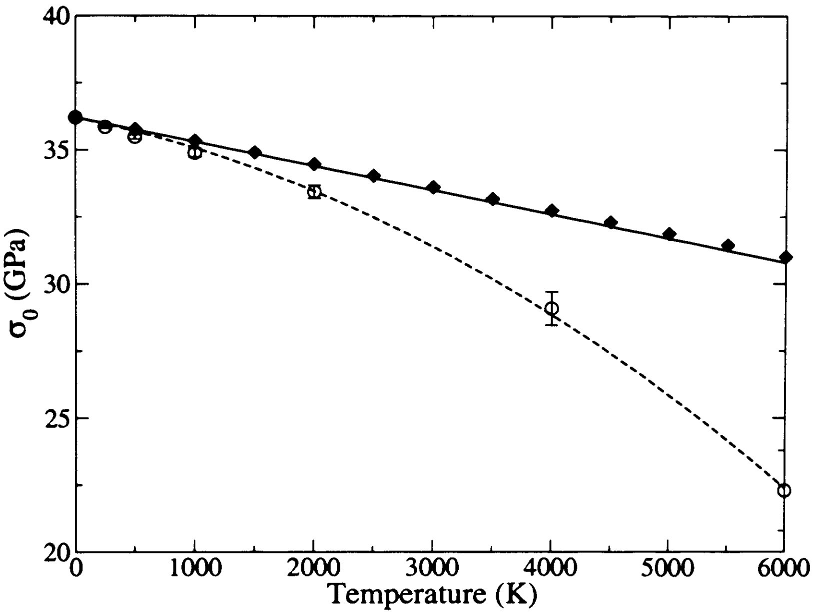

Figure 6.7: Molecular dynamics (open circles) and harmonic (diamonds) calculations of $\sigma_0 = \sigma_{33} - \sigma_{11}$ for a 6.97 Å^3 cell in the embedded atom model, with $c/a = 1.70$. The dashed curve represents a second-order fit to the MD data, while the solid line is its tangent at 0 K. In agreement with thermodynamic theory, this coincides the harmonic calculations of the stress.

6.5 *Ab initio* molecular dynamics

k-point sampling

Convergence tests for supercell size and length of run are taken wholly from the preceding embedded atom tests. The remaining consideration before performing my *ab initio* molecular dynamics simulations is that of k-point convergence. Since k-point sampling has a very profound effect on the computer time required to perform electronic structure calculations, and given the relationship between k-point sampling and size of simulation cell, I note that it may prove prudent to choose a cell containing more than 96 atoms, if I can then perform simulations with only one k point. If so, there is an additional speed-up, as the number of independent coefficients of the plane wave expansion is then halved.

To test k-sampling, I calculate $\sigma_{33} - \sigma_{11}$ for several disordered configurations, selected at random from embedded-atom MD trajectories, both with Γ-point sampling, and with larger numbers of k-points. The tests are performed for a 96-atom system, with an atomic volume of 6.97 Å^3 and an axial ratio of 1.65. The molecular dynamics simulation from which the configurations were drawn was performed at 5000 K. I took 4 snapshots at intervals of 0.2 ps. For this state point, $\sigma_{33} - \sigma_{11}$, with Γ-point sampling is equal to 7.0 ± 2.0 GPa. For a $2 \times 2 \times 2$ k-point grid, it is equal to 7.1 ± 2.6 GPa.

Results for σ_0

Fig. 6.8 shows a large number of calculations of σ_0 as a function of $q = c/a$, always at $V = 6.97$ Å^3, and these will be considered in turn. Firstly, the light curves show the harmonic computations of sec. 6.3.3, both at 4000 K (solid curve) and 5000 K (dashed curve) respectively. These are computed, as described in sec. 6.3.1, from the derivative $(\partial F/\partial q)_V$, and the equilibrium axial ratio occurs for $\sigma_0 = 0$.

The heavy curves represent molecular dynamics results. These are com-

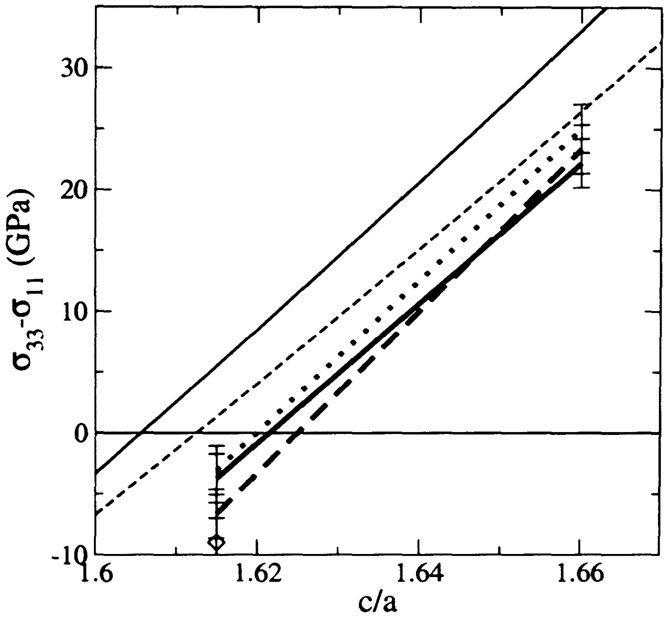

Figure 6.8: Comparison of *ab initio* M.D. (heavy curves) and harmonic (light) results for the stress $\sigma_{33} - \sigma_{11}$. Solid lines are at 4000 K, dashed lines at 5000 K. The dotted line shows results for 150-atom molecular dynamics at 4000 K. The diamond represents a 96-atom run including $3p$ states explicitly in the valence set. All calculations were performed for an atomic volume of 6.97 Å^3.

puted using Γ-point sampling. The solid and dashed lines again represent calculations at 4000 and 5000 K, and were performed using 96-atom cells. The error bars represent statistical error. Further computations at 4000 K using a 150-atom simulation cell are represented by the dotted line. The diamond shows a 96-atom run at 4000 K, in which the $3p$ electrons are treated explicitly within the valance set (see sec. 5.3). One can see immediately that the < 1 GPa shift in σ_0 due to the zero-point energy of the lattice, as discussed in Sec. 6.3.3 will have a negligible effect on the equilibrium axial ratio.

The predicted values of c/a arising from these computations are shown in fig. 6.4, along with my harmonic results, and the PIC calculations of Steinle-Neumann *et al.* [35].

6.6 Discussion

The many results of this chapter require careful analysis. Firstly, I have demonstrated that in the embedded atom model, the derivative $(\partial F_{\mathrm{harm}}/\partial q)_V$ can be used to compute the harmonic component of the quantity $\sigma_{33} - \sigma_{11}$, which agrees fully with molecular-dynamics simulations to first order in temperature, and that the anharmonic component of this stress can rise to around 2.5–6.0 GPa in the range 4000–5000 K.

If I assume that a similar behaviour for the anharmonic stress should be observed in my *ab initio* calculations, fig. 6.8 contains some surprises. Examining 96-atom MD calculations, represented by the solid and dashed heavy curves, at $ca = 1.66$, I see that the apparent anharmonicity at 4000 K is greater than that at 5000 K. That this anharmonicity is also much greater than that observed in the EAM, is not in itself a matter for concern. Concern about the apparently anomalous behaviour of the anharmonicity with temperature, motivated the further (dotted line) 150-atom simulations. Taken together with the statistical errors bars on my MD results, I see that size effects successfully account for the observed discrepancy. On the basis of these results, it follows that anharmonicity cannot shift the equilibrium value of c/a by more than ~ 0.01.

Our main results, then, are those of fig. 6.4, from which I draw the principle conclusion, that the strong temperature dependence of c/a predicted by Steinle-Neumann *et al.* [35] is not supported by rigorous MD and harmonic calculations. These results are in turn strongly supported by the recent diffraction experiments of Ma *et al.* Even allowing for the significant error bars on their c/a results, it seems clear that at 161 GPa, 2000 K, c/a is no bigger than around 1.61 at most. Our results would indicate a value of around 1.60 under these conditions.

ma già volgeva il mio disio e 'l
velle, sì come rota ch'igualmente
è mossa,
l'amor che move il sole e l'altre
stelle.

Dante Alighieri (1265–1321)

Chapter 7

Elasticity of hcp Fe

7.1 Introduction

In the last chapter I described calculations of the axial ratio of hcp Fe as a function of volume and temperature at the conditions of the Earth's inner core. Given this information, I may now proceed to compute the full elastic constant tensor c_{ijkl}, as a function of volume and temperature at the appropriate equilibrium axial ratio for that volume and temperature.

The methods I employ in this work are identical to those employed in the previous chapter, and only a brief description will be necessary. As before, the majority of my calculations are performed in the harmonic approximation, with fully anharmonic *ab initio* molecular dynamics (AIMD) used to check my results for certain values of volume and temperature.

The remaining, and significant decision in implementing these calculations, is the choice of axial ratio at which to evaluate c_{ijkl}. As seen in the previous chapter, anharmonicity may have some effect on the axial ratio; however this effect is not easily separable from system size effects and statistical error bars. Additionally I have found that this shift cannot be more than ~ 0.01. I therefore perform all calculations of elastic constants at those values of c/a determined by harmonic theory.

7.2 Calculating elastic properties

7.2.1 From free energy

In chapter 4 I set out the following equation for the variation of energy with strain about a starting configuration under (generally non-isotropic) stress $\sigma^0_{\alpha\beta}$, for symmetric strains:

$$\frac{W - W^0}{V^0} = \sigma^0_{\alpha\beta}\varepsilon_{\alpha\beta} + \frac{1}{2}c^0_{\alpha\beta\sigma\tau}\varepsilon_{\alpha\beta}\varepsilon_{\sigma\tau} + \frac{1}{2}\sigma^0_{\alpha\beta}\left(\varepsilon_{\alpha\beta}\varepsilon_{\sigma\sigma} - \varepsilon_{\alpha\sigma}\varepsilon_{\beta\sigma}\right) , \quad (7.1)$$

where $c^0_{\alpha\beta\sigma\tau}$ is the elastic constant tensor in the starting configuration. My harmonic calculations are capable of giving us directly the free energy, but not the stress in a solid, so I must use the above equation to decide how to calculate the elastic constants.

As set out in chapter 4, hcp Fe has five independent elastic constants c_{11}, c_{12}, c_{13}, c_{33} and c_{44}, with a sixth given by $c_{66} = (c_{11} - c_{12})/2$. To compute the elastic constants on the basis of energy, it is necessary to make five linearly independent deformations. I choose

$$\underline{\underline{\varepsilon}}^A = \begin{pmatrix} \delta & 0 & 0 \\ 0 & 0 & 0 \\ 0 & 0 & 0 \end{pmatrix} , \quad \underline{\underline{\varepsilon}}^B = \begin{pmatrix} \delta & 0 & 0 \\ 0 & \delta & 0 \\ 0 & 0 & 0 \end{pmatrix} , \quad (7.2)$$

$$\underline{\underline{\varepsilon}}^C = \begin{pmatrix} 0 & 0 & 0 \\ 0 & 0 & 0 \\ 0 & 0 & \delta \end{pmatrix} , \quad \underline{\underline{\varepsilon}}^D = \begin{pmatrix} \delta & 0 & 0 \\ 0 & 0 & 0 \\ 0 & 0 & \delta \end{pmatrix} \quad (7.3)$$

and

$$\underline{\underline{\varepsilon}}^E = \begin{pmatrix} 0 & 0 & 0 \\ 0 & 0 & \delta \\ 0 & \delta & 0 \end{pmatrix} . \quad (7.4)$$

With these choices, I can compute the energy density as a function of δ for each strain. Here I assume that $\sigma^0_{11} = \sigma^0_{22} \neq \sigma^0_{33}$, to allow for non-optimal choice of c/a ratio; all other initial stress elements are zero. We obtain

$$\begin{array}{lll}
 & \underline{\underline{\epsilon}}^{A}: & \dfrac{W^{A}(\delta)-W^{0}}{V^{0}}=\sigma_{11}^{0}\delta+\dfrac{1}{2}c_{11}\delta^{2}\,, \\
 & \underline{\underline{\epsilon}}^{B}: & \dfrac{W^{B}(\delta)-W^{0}}{V^{0}}=2\sigma_{11}^{0}\delta+(c_{11}+c_{12}+\sigma_{11}^{0})\delta^{2}\,, \\
 & \underline{\underline{\epsilon}}^{C}: & \dfrac{W^{C}(\delta)-W^{0}}{V^{0}}=\sigma_{33}^{0}\delta+\dfrac{1}{2}c_{33}\delta^{2}\,, \\
 & \underline{\underline{\epsilon}}^{D}: & \dfrac{W^{D}(\delta)-W^{0}}{V^{0}}=(\sigma_{11}^{0}+\sigma_{33}^{0})\delta+\dfrac{1}{2}[c_{11}+2c_{13}+c_{33}+\sigma_{11}^{0}+\sigma_{33}^{0}]\delta^{2} \\
\text{and} & \underline{\underline{\epsilon}}^{E}: & \dfrac{W^{E}(\delta)-W^{0}}{V^{0}}=\dfrac{1}{2}(4c_{44}-\sigma_{11}^{0}-\sigma_{33}^{0})\delta^{2}\,.
\end{array} \tag{7.5}$$

Clearly then, one computes, and fits as a polynomial function of δ, $(W(\delta)-W^{0})/V^{0}$. From strain A, one computes σ_{11}^{0} and c_{11}. Using these, one can compute from strain B c_{12}. Strain C gives c_{33} and σ_{33}^{0}, and using all these results, strain D gives c_{13}. Finally, strain E gives c_{44}.

7.2.2 From the stress tensor

The stress tensor produces the elastic constants much more directly, requiring only two linearly independent strains of the crystal. These are given by

$$\begin{array}{rl}
 & \underline{\underline{\epsilon}}^{X}=\begin{pmatrix}\epsilon & 0 & 0\\ 0 & 0 & \epsilon/2\\ 0 & \epsilon/2 & 0\end{pmatrix} \\
\text{and} & \underline{\underline{\epsilon}}^{Z}=\begin{pmatrix}0 & 0 & 0\\ 0 & 0 & 0\\ 0 & 0 & \epsilon\end{pmatrix}.
\end{array} \tag{7.6}$$

These strains are performed for $\epsilon = \pm\delta$ for some small δ, with the result

$$\begin{aligned} & \sigma_{11}(\delta) - \sigma_{11}(-\delta) = 2c^0_{11}\delta \ , \\ & \sigma_{22}(\delta) - \sigma_{22}(-\delta) = 2c^0_{12}\delta \ , \\ & \sigma_{33}(\delta) - \sigma_{33}(-\delta) = 2c^0_{13}\delta \ , \\ \text{and} \qquad & \sigma_{23}(\delta) - \sigma_{23}(-\delta) = 2c^0_{44}\delta \end{aligned} \tag{7.7}$$

for $\underline{\underline{\varepsilon}}^X$, and

$$\sigma_{33}(\delta) - \sigma_{33}(-\delta) = 2c^0_{13}\delta \tag{7.8}$$

for $\underline{\underline{\varepsilon}}^Z$.

7.2.3 Atomic relaxation

A consideration which arises in my perfect-lattice and harmonic calculations, but not in my AIMD calculations, is that of the relaxation of atomic degrees of freedom within a cell. As the strains $\underline{\underline{\varepsilon}}^A$, $\underline{\underline{\varepsilon}}^B$, $\underline{\underline{\varepsilon}}^D$ and $\underline{\underline{\varepsilon}}^E$ are applied, the symmetry of the primitive cell is broken, meaning that the positions of certain atoms cannot be known, except by direct atomistic minimization.

In order to compute the force constant matrix in harmonic systems, we require that displacements be made about some equilibrium atomic position, where no net forces act on the atoms. Therefore I shall use the following method to compute energies for elastic constants:

1. For a given V, T, choose the correct value of c/a on the basis of the harmonic calculations of Ch. 6.
2. For each of the matrices $\underline{\underline{\varepsilon}}$
    (a) for $-0.02 \leq \delta \leq 0.02$ in steps of 0.008
    (b) for ε^A, ε^D or ε^E, relax the atomic positions by minimizing the free energy of the static, strained lattice, then
    (c) compute free energy of the static lattice ,

(d) construct supercell, and compute $\bar{\omega}$ as before by means of small displacements.

Because perfect-lattice calculations on a two-atom cell are relatively inexpensive when contrasted with harmonic calculations, there is no significant difficulty in bringing these atomistic relaxations to a high degree of convergence, and I choose the extremely precise convergence criterion of 10^{-6} eV/cell.

7.3 Embedded-atom constants

Using the smoothed embedded-atom potential of the previous chapter, it is relatively inexpensive to perform tests of size convergence, and to examine the effects of anharmonicity, on elastic constants, both in the harmonic limit, and using molecular dynamics. For this reason, my first calculations of elastic constants were performed using the embedded-atom potential, and these I describe first. These calculations were performed for the single atomic volume of 6.97 Å^3.

7.3.1 Harmonic constants

Firstly, for a two atom cell, the various strains ε^A to ε^E are applied for values of δ from -0.021 to 0.021 in steps of 0.003. For the strains ε^A, ε^D and ε^E, the positions of the atoms are relaxed, and their final positions retained. By computing the total energy, I am able to calculate elastic constants at zero temperature using the expressions (7.5). Using a fourth-order polynomial fit to the energy gives the values $c_{11} = 1859.8$ GPa, $c_{12} = 1473.8$ GPa, $c_{33} = 2066.0$ GPa, $c_{13} = 1278.8$ GPa, $c_{44} = 196.46$ GPa and $c_{66} = 192.99$ GPa.

Next, supercells are built to perform harmonic calculations. For each strain and value of delta, the final positions of the atoms are taken to build the supercell. Supercells were constructed containing 36, 54, 96, 128 and 150 atoms. For each of these supercells, $\bar{\omega}$ was computed as previously

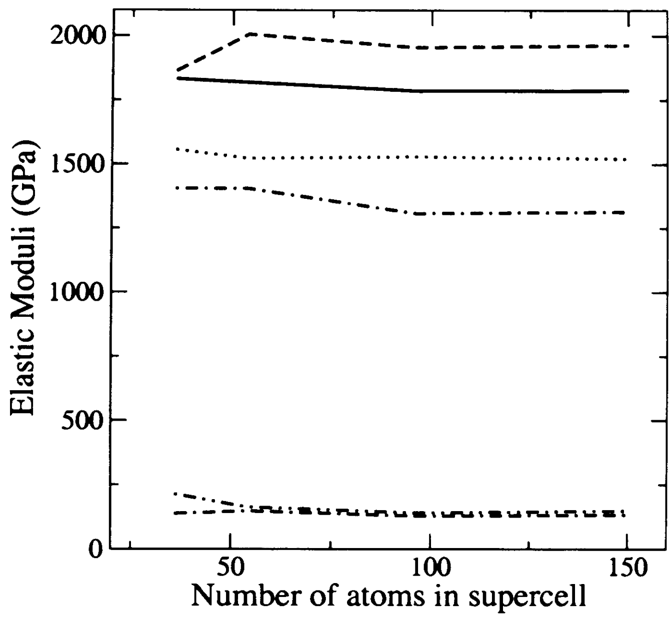

Figure 7.1: Elastic constants as a function of cell size in the harmonic approximation. Solid line c_{11}, dotted line c_{12}, dashed line c_{33}, dot-dashed line c_{33}, dot-dot-dashed line c_{44}, dash-dash-dotted line c_{44}.

described, by performing small displacements on one of the atoms and computing the force-constant matrix $\Phi^{\mathbf{L}}_{s\mu,s'\nu}$. Since strains ε^A, ε^D and ε^E break the symmetry of the h.c.p. lattice, it is necessary in these cases to make three, rather than two separate atomic displacements.

Shown in Fig. 7.1 are the harmonic elastic constants at 6000 K for different sizes of cell. It is clear that the 54-atom cell shows the convergence I require.

7.3.2 Molecular dynamics constants

I now turn to molecular dynamics calculations of the elastic constants, and zero-temperature calculations based on the stress. For the zero temperature calculations, I perform the strains ε^X and ε^Z, in the first case relaxing the atomic positions. This is done for the same values of δ as for the harmonic constants. I perform a third-order polynomial fit of the stress components, and extract the elastic constants. This gives the values $c_{11} = 1859.9$ GPa, $c_{12} = 1473.9$ GPa, $c_{33} = 2066.0$ GPa, $c_{13} = 1278.8$ GPa, $c_{44} = 196.42$ GPa and $c_{66} = 193.00$ GPa. These values are essentially identical to those computed from the energy. The minuscule difference is due simply to the tolerance of the fitting algorithm.

Molecular dynamics calculations are a simpler matter to perform than my harmonic calculations, if substantially more expensive. For each matrix ε^X and ε^Z, and for $\epsilon = \pm 0.02$, I perform 2.5 ps simulation runs at temperatures of 1000, 2000, 3000, 4000 and 5000 K. The first ps of each run is discarded to allow for equilibration, and then the remaining 1.5 ps are averaged to compute the stresses. With this value of ϵ and length of run, Fig. 6.5 tells us that for a 4000 K, 96-atom simulation cell c_{11} and c_{33} will be accurate to within around 25 GPa. On this basis, the anisotropy $c_{33} - c_{11}$ would be correct to within 35 GPa.

Fig. 7.2 shows molecular-dynamics calculations of elastic constants for 54, 96, 128 and 150-atom simulation cells. It is clear that convergence well within the statistical error is obtained for a 96-atom cell. Here I have used particularly long (5 ps) runs, to separate statistical errors from the relatively small size effects. Statistical errors in this instance are well under 10 GPa. Fig. 7.3 shows, for a 150-atom simulation cell, molecular dynamics constants as a function of temperature, along with harmonic elastic constants. I observe, that the linear temperature dependence of the harmonic elastic constants constants agrees very well with the molecular dynamics constants. Anharmonicity is too small to be observed in this system.

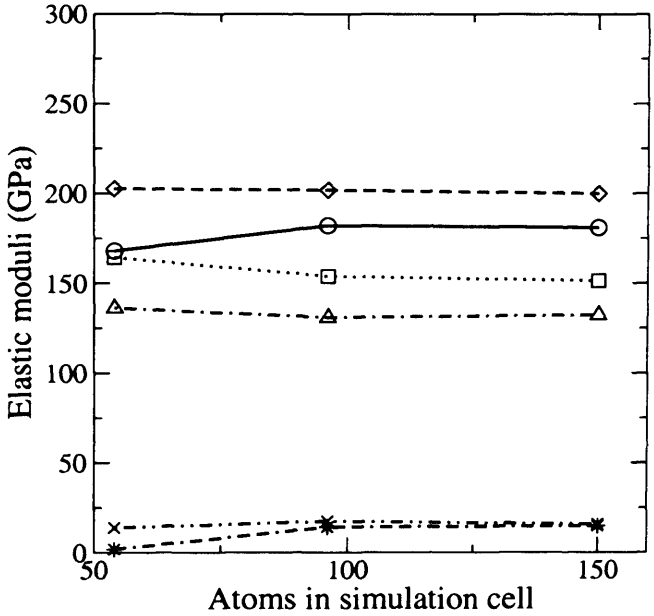

Figure 7.2: Elastic constants from embedded-atom molecular dynamics simulation as a function of supercell size. Elastic constants are represented as follows. c_{11}: solid line and circle; c_{12}: dotted line and square; c_{33}: dashed line and diamond; c_{13}: dash-dot line and diamond; c_{44}: dot-dot-dash line and cross; c_{66}: dot-dash-dash line and star.

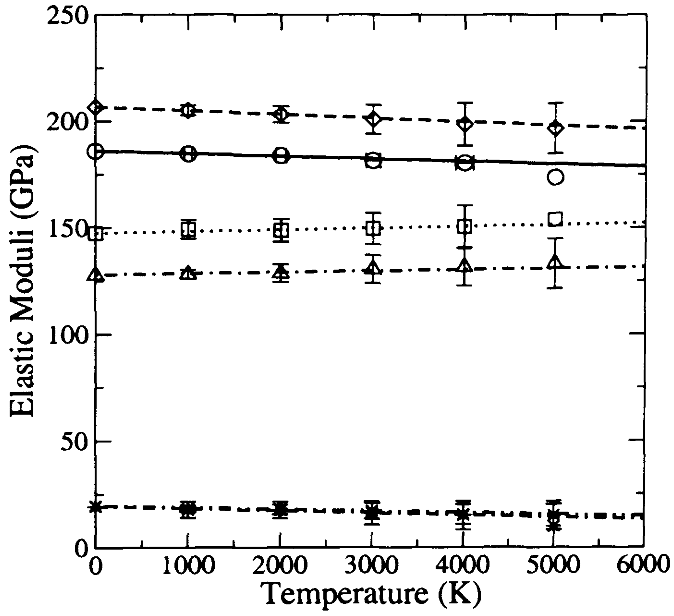

Figure 7.3: Harmonic and molecular-dynamics elastic constants as a function of temperature in the embedded-atom model. Elastic constants are represented as per Fig. 7.2

7.4 *Ab initio* elastic constants of the perfect lattice.

As discussed above, I wish in this work to calculate elastic constants to within around 1%, which I hope will give us the anisotropy measure $c_{33} - c_{11}$ to within around 15%, based on the zero-temperature calculations of [84]. This requires convergence of non-cancelling errors in the stress with respect to both k-point sampling and plane-wave cutoff to around 1–2 GPa. This places similar constraints on the errors to those encountered in the previous chapter, so I adopt the same k-point sampling in the perfect lattice as for these previous calculations.

Perfect lattice calculations of free energy were performed at atomic volumes of 6.97, 7.50 and 8.67 Å^3; for electronic temperatures of 2000, 4000 and 6000 K; and for $\delta = -0.020$, -0.012, -0.004, 0.004, 0.012 and 0.020 for each of the deformation matrices $\underline{\underline{\varepsilon}}^A$, $\underline{\underline{\varepsilon}}^B$, $\underline{\underline{\varepsilon}}^C$, $\underline{\underline{\varepsilon}}^D$ and $\underline{\underline{\varepsilon}}^E$. Additionally, perfect lattice calculations of strain were performed at the same volumes and temperatures, and additionally at 1000, 3000 and 5000 K, for $\delta = -0.020$, -0.010, 0.010 and 0.020. The calculations of stress will be used to find the elastic constants in the limit of zero temperature. The calculations of energy can be used to test the relations of the previous section.

I will compare perfect-lattice elastic constants derived from free energy and from stress at 6.97 Å^3 and 6000 K. Fig. 7.4 shows the energy density $\Delta W(\delta)/V^0$ in GPa. The axial ratio is relaxed within the harmonic limit at that temperature, and internal degrees of freedom have been relaxed to within 10^{-6} eV Å^{-3} for each δ. Fitting polynomials through these data

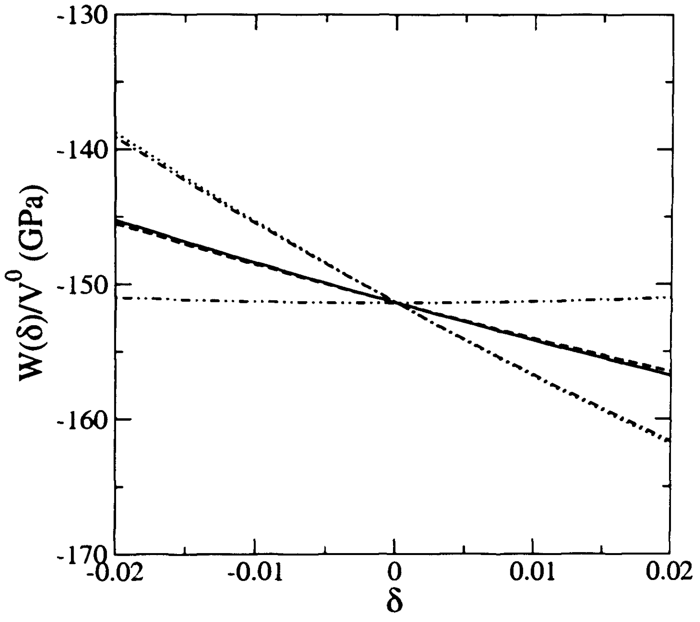

Figure 7.4: Energy density $W(\delta)/V^0$ in GPa as a function of δ for each of the strain matrices ε^A (solid line, yields c_{11}), ε^B (dotted line, yields c_{12}), ε^C (dashed line, yields c_{33}), ε^D (dot-dashed line, yields c_{13}) and ε^E (double-dot-dashed line, yields c_{44}).

gives

$$
\begin{aligned}
\sigma_{11}^{0} &= \frac{1}{V^0}\frac{\partial W^{(A)}}{\partial \delta} = 287.1 \text{ GPa} , \\
\sigma_{33}^{0} &= \frac{1}{V^0}\frac{\partial W^{(C)}}{\partial \delta} = 273.8 \text{ GPa} , \\
c_{11} &= \frac{1}{V^0}\frac{\partial^2 W^{A}}{\partial \delta^2} = 2020 \text{ GPa} , \\
c_{12} &= \frac{1}{2V^0}\frac{\partial^2 W^{B}}{\partial \delta^2} - c_{11} + \sigma_{11}^{0} = 1053 \text{ GPa} , \qquad (7.9) \\
c_{33} &= \frac{1}{V^0}\frac{\partial^2 W^{C}}{\partial \delta^2} = 2095 \text{ GPa} , \\
c_{13} &= \frac{1}{2}\left[\frac{1}{V^0}\frac{\partial^2 W^{D}}{\partial \delta^2} - c_{11} - c_{33} - \sigma_{11}^{0} - \sigma_{33}^{0}\right] = 783.1 \text{ GPa} \\
\text{and} \quad c_{44} &= \frac{1}{4}\left[\frac{1}{V^0}\frac{\partial^2 W^{E}}{\partial \delta^2} - \frac{p}{2}\right] = 370.0 \text{ GPa}
\end{aligned}
$$

If, by comparison, I compute the stress components in the same (atomistically relaxed) configurations (fig. 7.5) I find

$$
\begin{aligned}
c_{11} &= \frac{\partial \sigma_{11}^{X}}{\partial \delta} = 1912 , \\
c_{12} &= \frac{\partial \sigma_{22}^{X}}{\partial \delta} = 1071 , \\
c_{33} &= \frac{\partial \sigma_{33}^{Z}}{\partial \delta} = 2067 , \qquad (7.10) \\
c_{13} &= \frac{\partial \sigma_{33}^{X}}{\partial \delta} = 897 , \\
c_{44} &= \frac{\partial \sigma_{23}^{X}}{\partial \delta} = 380 .
\end{aligned}
$$

Finally, 7.6 compares these calculations as a function of electronic temperature at 6.97 Å^3.

7.5 Harmonic calculations

My chosen constraints on errors, are, as already stated, similar to those in the preceding chapter. Additionally, my calculations with the embedded-atom potential demonstrate that a 54-atom supercell geometry provides convergence of the elastic constants to well within my target error. I adopt

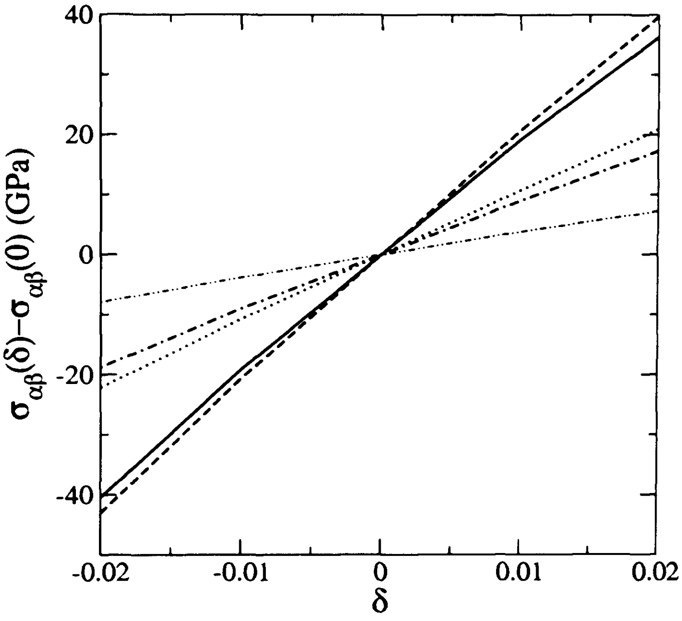

Figure 7.5: Stress components $\sigma_{\alpha\beta}(\delta) - \sigma_{\alpha\beta}(0)$. The solid, dotted, dot-dashed and double-dot-dashed lines represent, for the deformation ε^X, stress components σ_{11}, σ_{12}, σ_{33} and σ_{44} respectively. The dot-dashed line represents σ_{33} under the deformation ε^Z.

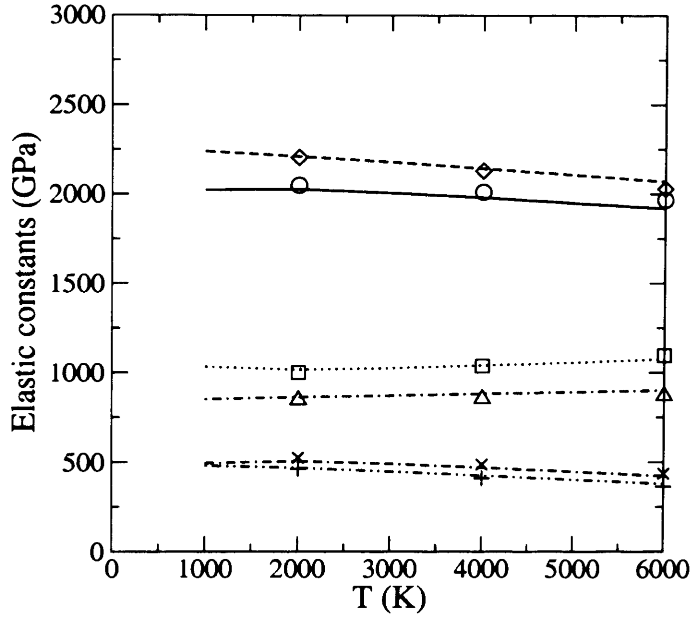

Figure 7.6: Perfect-lattice elastic constants as a function of electronic temperature. Symbols represent free-energy calculations, while lines show calculations based on the stress. Constants are represented as in Fig. 7.2.

therefore, for these harmonic calculations, a 54-atom supercell with a 3×3×2 Monkhorst-Pack k-point grid, as used in the previous chapter.

For $V^0 = 6.97$ and 8.69 Å^3, and for $T_{\rm el} = 2000$, 4000 and 6000 K, and for $\delta = -0.021$, -0.015 -0.009 -0.003 0.003 0.009 0.015 and 0.021, I computed $\bar{\omega}$ for each of the strain matrices, just as I did with the embedded-atom potential. Equations (7.5) and (3.40) then give a harmonic contribution for $\underline{\underline{\varepsilon}}^A$, for example, of

$$c_{11}^{\rm harm} = 3k_{\rm B}T\frac{\partial}{\partial\delta}\ln\bar{\omega}\,, \tag{7.11}$$

and similarly for the other elastic constants, which can be added to the perfect lattice values to give elastic constants in the harmonic limit.

My harmonic values of elastic constants will be plotted, along with my molecular dynamics results in the next section.

7.6 *Ab initio* molecular dynamics

7.6.1 Technical considerations

Calculations using the embedded atom potential discussed in Sec. 7.3.2, demonstrate that a 96-atom MD simulation cell is large enough to reduce supercell-size errors to within my target convergence. However, following the results for k-point sampling as discussed in Ch. 6, and on the effect of using a 150-atom cell as shown in Fig. 6.8, I employ here a 150-atom cell with Γ-point sampling for my *ab initio* molecular dynamics simulations.

As for the corresponding embedded-atom results, calculations are performed under the strains $\underline{\underline{\varepsilon}}^X$ and $\underline{\underline{\varepsilon}}^Z$, for $\delta = -0.02$, -0.01, 0.01 and 0.02. As described in Ch. 6, this is done by pre-equilibrating for 1 ps using the embedded atom potential. Average values and variances of the elastic constants are computed over the runs; errors are then computed using the method of block averages (see Ch. 6).

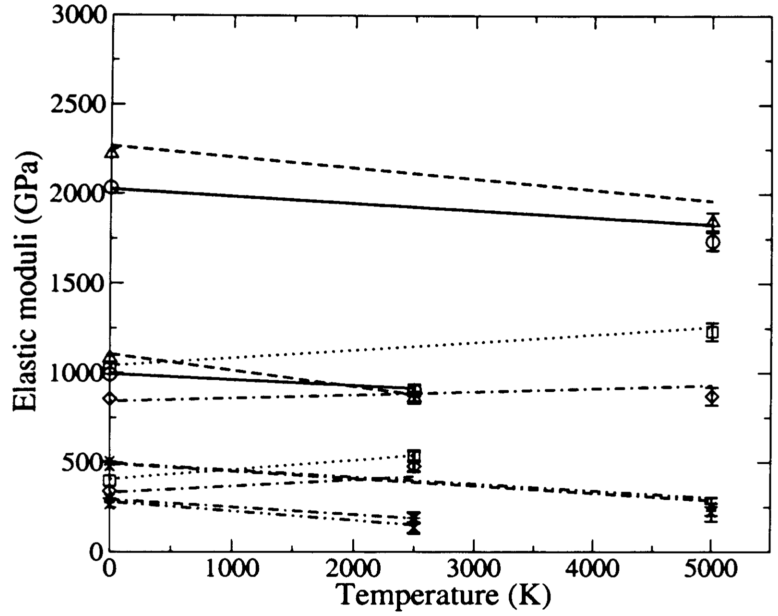

Figure 7.7: Elastic constants of hcp Fe from harmonic (lines) and AIMD (symbols with error bars) calculations. Lines extending to 5000 K are at 6.97 Å^3. Lines extending to 2500 K are at 8.67 Å^3. Corresponding MD simulations are at the save volumes. The constants are represented as follows at both volumes as in Fig. 7.2.

7.6.2 Results

Computed elastic constants based on 1 ps molecular dynamics trajectories are shown in Fig. 7.7, along with harmonic calculations. The most immediate observation is that at inner core conditions of 6.97 Å^3, there is no intersection of c_{11} and c_{33} up to temperatures close to the melting point. Using the Christoffel equation for h.c.p. symmetry, (4.32), I find that for compressional waves travelling parallel to the hexagonal axis, $\rho v_3^2 = c_{33}$, whereas for those travelling perpendicular to the hexagonal axis, $\rho v_1^2 = c_{11}$. Therefore the seismic anisotropy resulting from a complete alignment of hexagonal crystalline axes with the Earths rotational axis would be

$$\Delta = \frac{v_3 - v_1}{v_1} = \sqrt{\frac{c_{33}}{c_{11}}} - 1 = 3.1\% \tag{7.12}$$

in agreement with seismic observations.

The Voigt scheme for polycrystalline averages (Ch. 4) gives us for the isothermal bulk modulus $K_T = 1250$ GPa, and for the shear modulus $\mu = 295 \pm 33$ GPa. Using the results of [34], I have from (3.27)

$$\begin{aligned} K_S &= K_T(1 + \alpha\gamma T) \\ &= (1250 \text{ GPa})(1 + 1.1 \times 10^{-5} \times 1.43 \times 5000) \\ &= 1350 \pm 38 \text{ GPa} . \end{aligned} \tag{7.13}$$

This yields for Poisson's ratio

$$\nu = \frac{3K - 2\mu}{2(3K + \mu)}. = 0.40 \pm 0.01 \tag{7.14}$$

7.7 Discussion

These results support the hypothesis that the softening of c_{33} and corresponding hardening of c_{11} observed by Steinle-Neumann *et al.* [35] arises directly from their observation of a c/a ratio which increases rapidly with temperature. Indeed, at high atomic volumes ($V = 8.67$ Å^3), where c/a does indeed rise rapidly with temperature, I do observe the high-temperature intersection of c_{11} and c_{33}. However this does not occur at the atomic volumes associated with the inner core, where I find consistently that $c_{33} > c_{11}$.

Instead, I observe that the velocity v_3 along the hexagonal axis of the hcp lattice is about 3.1 % greater than v_1 at 6.97 Å^3, irrespective of temperature, and hence that the zero-temperature interpretation of [84], that hcp must be ordered in the inner core with its hexagonal axes along the Earth's polar axis, is found to hold at all temperatures

I have also found that the value of Poisson's ratio for hcp Fe at inner-core conditions is somewhat smaller than that of the inner core. This could arise from the presence of light impurities in the core, or if the phase of Fe in the inner core were b.c.c., which recent studies [85] indicate to be a very possible candidate. This remains an open question.

Chapter 8

Discussion and Conclusions

8.1 Principal results

The Earth's inner core consists of solid iron alloyed with a number of lighter elements. This solid is in an uncertain crystalline phase — likely h.c.p. — which exhibits elastic anisotropy such that compressional body waves traversing the inner core travel some 3–4 % more quickly along the polar axis than in the equitorial plane. I have used *ab initio* molecular dynamics and harmonic theory, to investigate the elastic properties of hcp iron at core conditions, and examine the implications of the properties for our understanding of inner-core anisotropy.

First, I have examined the particle-in-cell (PIC) approximation, which has been used in all previous determinations of the high-temperature elasticity of hcp iron. Here I discovered that the PIC model did an excellent job of describing those properties of iron which were well-described in harmonic theory, and I discovered that this was due to the uniform scaling of the phonon modes of hcp iron with atomic volume (see Fig. 3 of Ref. [34]), such that those particular modes which are calculated in the harmonic approximation to PIC, give the same thermodynamics as full-spectrum harmonic calculations. By contrast, however I discovered that PIC had no capability to calculate anharmonic free energies, and therefore offered no real advantage over full-spectrum harmonic calculations.

During my analysis of the PIC model, I discovered that the observation of Steinle-Neumann *et al.* [35] of a strong temperature dependence of the hcp axial ratio c/a was not observed in my PIC calculations. The cause of this discrepancy, however, remained unclear, and so I undertook to perform rigorous *ab initio* molecular dynamics and harmonic calculations of c/a. I discovered that at an atomic volume of 6.97 Å^3, similar to that in the inner core, c/a never exceeds approximately 1.62 at the melting point, in stark contrast with the predictions of [35]. I also found that my results were in excellent agreement with new experimental data [79].

Using these new values for c/a, I were able at last to perform accurate *ab initio* molecular dynamics and harmonic calculations of the elastic constants of hcp Fe at inner-core conditions. I found, as suggested by [35], a strong correspondence between an increasing c/a, and a softening of the c_{33} elastic constant, and corresponding hardening of c_{11}. Most significantly, however, I discovered that the c_{33} is greater than c_{11} for all temperatures up to the melting point at inner-core density, and the resultant conclusion that the compressional wave velocity is always greater along the hexagonal axis of the hcp lattice.

8.2 Geophysical implications

The principal geophysical implications of this work are twofold. Firstly, that an inner core composed of hcp iron must consist entirely of crystallites whose hexagonal axes are completely aligned along the Earth's polar axis. This is exactly the zero-temperature interpretation of elastic anisotropy reached by [84]; however I have demonstrated it for all temperatures up to the melting point of Fe.

The second implication of this work arises from the observation that

Poisson's ratio for hcp Fe at inner-core temperature and pressure is lower than that of the inner core. I compute this value to be 0.40 ± 0.01, compared with a known value of 0.44 for the inner-core. This implies only, however, that the inner core cannot consist of pure hcp Fe, as is already known from the Earth's density profile.

8.3 Directions for further research

There are an immeasurable host of directions for *ab initio* simulation work in the Earth's core, and this will only increase as more techniques become available. It is believed by some that oxygen in the Earth's core will react to form FeO, but this question will only be answered when *ab initio* calculations can be performed on FeO. This is challenging, as it is a strongly correlated system, and not susceptible to treatment with DFT. It may be hoped that ongoing developments in diffusion Monte Carlo will allow further development of this field.

In respect of the seismic anisotropy of the inner core, however, the most important next directions will be twofold. Firstly, an understanding of the elasticity of bcc Fe is vitally needed. If the Poisson's ratio of bcc Fe turns out to match that of the inner core better than does hcp it is possible that the matter of the crystal structure of the inner core may be settled. The elasticity of bcc Fe is the subject of ongoing research by Lidunka Vočadlo, and these results will be of great importance to the field.

Finally, the effects of light-element alloying on the elasticity of Fe must be studied as the presence of such light impurities in known to reduce the melting point of Fe, and could very easily affect the value of Poisson's ratio.

Bibliography

[1] K. C. Creager. Anisotropy of the inner core from differential traveltimes of the phases pkp and pkikp. *Nature*, 356:309, 1992.

[2] Max Born and Huang Kun. *Dynamical Theory of Crystal Lattices (International Series of Monographs on Physics.* Oxford University Press, 1954.

[3] J. O. Hirshfelder, C. F. Curtiss, and R. B. Bird. *Molecular Theory of Gases and Liquids.* John Wiley and Sons, Inc, New York, 1954.

[4] M. P. Allen and D. J. Tildesley. *Computer Simulation of Liquids.* Clarendon Press, Oxford, 1989.

[5] R. G. Parr and W. Yang. *Density-functional theory of atoms and molecules.* Oxford University Press, New York, 1989.

[6] W. M. C. Foulkes, L. Mitas, R. J. Needs, and G. Rajagopal. Quantum monte carlo simulations of solids. *Rev. Mod. Phys.*, 73:33, 2001.

[7] P. Hohenberg and W. Kohn. Inhomogeneous electron gas. *Phys. Rev.*, 136:B864, 1964.

[8] W. Kohn and L. Sham. Self-consistent equations including exchange and correlation effects. *Phys. Rev.*, 140:A1133, 1965.

[9] R. O. Jones and O. Gunnarsson. The density functional formalism, its applications and prospects. *Rev. Mod. Phys.*, 61:689, 1989.

[10] N. D. Mermin. Thermal properties of the inhomogeneous electron gas. *Phys. Rev.*, 137:A1441, 1965.

[11] J. P. Perdew and A. Zunger. Self-interaction correction to density-functional approximations for many-electron systems. *Phys. Rev. B*, 23:5048, 1981.

[12] Y. Wang and J. P. Perdew. Correlation hole of the spin-polarized electron gas, with exact small-wave-vector and high-density scaling. *Phys. Rev. B*, 44:13298, 1991.

[13] J. P. Perdew, J. A. Chevary, S. H. Vosko, K. A. Jackson, M. R. Pederson, D. J. Singh, and C. Fiolhais. Atoms, molecules, solids and surfaces - applications of the generalized gradient approximation for exchange and correlation. *Phys. Rev. B*, 46:6671, 1992.

[14] P. E. Blöchl. Projector augmented-wave method. *Phys. Rev. B*, 50:953, 1994.

[15] R. Car and M. Parrinello. Unified approach of molecular dynamics and density-functional theory. *Phys. Rev. Lett.*, 55:2471, 1985.

[16] Data published by IUGG.

[17] G. C. Brown and A. E. Mussett. *The Inaccesssible Earth.* Unwin Hyman Ltd, 1981.

[18] G. M. Garland. *Introduction to geophysics: mantle, crust and core.* W. B. Saunders, Philidelphia, 1971.

[19] F. Press. Earth models obtained by monte carlo inversion. *J. Geophys. Res.*, 73:5223, 1968.

[20] F. Press. Regionalized Earth models. *J. Geophys. Res.*, 75:6575, 1970.

[21] A. M. Dziewonski and D. L. Anderson. Preliminary reference Earth model. *Phys. Earth Planet. Inter*, 25:297, 1981.

[22] D. Alfè, G. D. Price, and M. J. Gillan. *Ab initio* chemical potentials of solid and liquid solutions and the chemistry of the Earth's core. *J. Chem. Phys*, 116:7127, 2002.

[23] D. Alfè, M. J. Gillan, and G. D. Price. Constraints on the composition of the Earth's core from *ab initio* calculations. *Nature*, 405:172, 2000.

[24] W. A. Basset. The diamond cell and the Earth's interior. *Ann. Rev. Earth Planet. Sci.*, 7:357, 1977.

[25] S. Akimoto, T. Suzuki, and O. Shumomura. Phase diagram of iron determined by high pressure/temperature x-ray diffraction using synchrotron radiation. In M. H. Manghnani and Y. Syono, editors, *High Pressure Research in Mineral Physics*, page 149. American Geophysical Union, Washington D.C., 1987.

[26] R. Boehler. Temperatures in the Earth's core from melting-point measurements of iron at high static pressures. *Nature*, 363:534, 1993.

[27] T. J. Ahrens. Dynamic compression of Earth materials. *Science*, 207:1035, 1980.

[28] J. M. Brown and R. G. McQueen. Phase-transitions, Grüneisen-parameter and elasticity for shocked iron between 77-GPa and 400-GPa. *J. Geophys. Res., [Space Phys]*, 91:7485, 1986.

[29] L. Stixrude, R. E. Cohen, and D. J. Singh. Iron at high pressure: Linearized-augmented-plane-wave computations in the generalized-gradient approximation. *Phys. Rev. B*, 50:6442, 1994.

[30] Lidunka Vočadlo, Gilles A. de Wijs, Georg Kresse, Mike Gillan, and Geoffrey D. Price. First principle calculations on crystalline and liquid iron at Earth's core conditions. *Faraday Discuss.*, 106:205, 1997.

[31] D. Alfè, M. J. Gillan, and G. D. Price. The melting curve of iron at the pressures of the Earth's core from *ab initio* calculations. *Nature*, 401:462, 1999.

[32] D. Alfè, G. Kresse, and M. J. Gillan. Structure and dynamics of liquid iron under Earth's core conditions. *Phys. Rev. B*, 61:132, 2000.

[33] Lidunka Vočadlo, Dario Alfè, Geoffrey D. Price, and Michael J. Gillan. First principles calculations on the diffusivity and viscosity of liquid fe-s at experimentally accessible conditions. *Phys. Earth Planet. Inter*, 120:145, 2000.

[34] D. Alfè, G. D. Price, and M. J. Gillan. Thermodynamics of hexagonal-close-packed iron under Earth's core conditions. *Phys. Rev. B*, 64:045123, 2001.

[35] G. Steinle-Neumann, L. Stixrude, R. E. Cohen, and O. Gülseren. Elasticity of iron at the temperature of the Earth's inner core. *Nature*, 413(6851), 2001.

[36] E. Wasserman, L. Stixrude, and R. E. Cohen. Thermal properties of iron at high pressures and temperatures. *Phys. Rev. B*, 53:8296, 1996.

[37] L. Stixrude, E. Wasserman, and R. E. Cohen. Composition and temperature of Earth's inner core. *J. Geophys. Res., [Space Phys]*, 102:24729, 1997.

[38] D. Marx and M. Parrinello. *Ab initio* path integral molecular dynamics: Basic ideas. *J. Chem. Phys*, 104:4077, 1996.

[39] L. H. Thomas. The calculation of atomic fields. *Proc. Camb. Phil. Soc*, 23:542, 1927.

[40] E. Fermi. Un metodo statistico per la determinazione di alcune proprietà dell'atomo. *Rend. Accad., Lincei*, 6:602, 1927.

[41] E. Fermi. A statistical method for the determinaltion of some atomic properties and the application of this method to the theory of the periodic system of elements. *Z. Phys*, 48:73, 1928. Translated in [43].

[42] E. Fermi. Sulla deduzione statistica di alcune proprieta dell'atomo. applicazione alla teoria del systema periodico degli elementi. *Rend. Accad., Lincei*, 7:342, 1928.

[43] N. H. March. *Self Consistent fields in atoms.* Oxford: Pergamon, 1975.

[44] U. von Barth and L. Hedin. A local exchange-correlation potential for the spin polarized case. *J. Phys. C*, 5:1629, 1972.

[45] O. Gunnarsson and B. I. Lundqvist. Exchange and correlation in atoms, molecules, and solids by the spin-density-functional formalism. *Phys. Rev. B*, 13:4274, 1976.

[46] S. H. Vosko, L. Wilk, and M. Nusair. Accurate spin-dependent electron liquid correlation energies for spin density calculation: a critical analysis. *Can. J. Phys.*, 58:1200, 1980.

[47] J. P. Perdew. Accurate density functional for the energy: Real-space cutoff of the gradient expansion for the exchange hole. *Phys. Rev. Lett.*, 55:1665, 1985.

[48] J. P. Perdew. Unified theory of exchange and correlation beyond the local density approximation. In P. Ziesche and H. Eschrig, editors, *Electronic Structure of Solids.* Akedemie Verlag, Berlin, 1991.

[49] M. C. Payne, M. P. Teter, D. C. Allan, T. A. Arias, and J. D. Joannopoulos. Iterative minimization techniques for *ab initio* total-energy calculations: molecular dynamics and conjugate gradients. *Rev. Mod. Phys.*, 64:1045, 1992.

[50] H. J. Monkhorst and J. D. Pack. Special points for Brillouin-zone integrations. *Phys. Rev. B*, 13:5188, 1976.

[51] D. R. Hamann, M. Schlüter, and C. Chiang. Norm-conserving pseudopotentials. *Phys. Rev. Lett.*, 43:1494, 1979.

[52] G. Kerker. Non-singular atomic pseudopotentials for solid state applications. *J. Phys. C*, 13:L189, 1980.

[53] A. Zunger and M. L. Cohen. First-principles nonlocal-pseudopotential approach in the density-functional formalism: Development and application to atoms. *Phys. Rev. B*, 18:5449, 1978.

[54] A. Zunger and M. L. Cohen. First-principles nonlocal-pseudopotential approach in the density-functional formalism. ii. application to electronic and structural properties of solids. *Phys. Rev. B*, 20:4082, 1979.

[55] David Vanderbilt. Soft self-consistent pseudopotentials in a generalized eigenvalue formalism. *Phys. Rev. B*, 41:7892, 1990.

[56] J. K. Roberts and A. R. Miller. *Heat and Thermodynamics.* Blackie & Son Limited, London, fifth edition, 1960.

[57] Jean-Paul Poirier. *Introduction to the Physics of the Earth's Interior.* Cambridge University Press, Cambridge, 2 edition, 2000.

[58] D. Frenkel and B. Smit. *Understanding Molecular Simulation.* Academic, San Diego, 1996.

[59] H. C. Andersen. Molecular dynamics simulations at constant pressure and/or temperature. *J. Chem. Phys*, 72:2384, 1980.

[60] A. C. Holt and M. Ross. Calculations of the Grüneisen parameter of some models of the solid. *Phys. Rev. B*, 1:2700, 1970.

[61] A. C. Holt, W. G. Hoover, S. G. Gray, and D. R. Shortle. Comparison of the lattice-dynamics and cell-model approximations with Monte-Carlo thermodynamic properties. *Physica*, 49:61, 1970.

[62] F. H. Ree and A. C. Holt. Thermodynamic properties of the alkali-halide crystals. *Phys. Rev. B*, 8:826, 1973.

[63] K. Westra and E. R. Cowley. Cell-cluster expansion for an anharmonic solid. *Phys. Rev. B*, 11:4008, 1975.

[64] E. R. Cowley, J. Gross, Z. X. Gong, and G. K. Horton. Cell-cluster and self-consistent calculations for a model sodium-chloride crystal. *Phys. Rev. B*, 42:3135, 1990.

[65] T. H. K. Barron and M. L. Klein. Second-order elastic constants of a solid under stress. *Proc. Phys. Soc.*, 85:523, 1965.

[66] Ken Huang. On the atomic theory of elasticity. *Proc. Roy. Soc. A*, 203:178, 1950.

[67] J. F. Nye. *Physical properties of crystals.* Oxford University Press, San Diego, 1957.

[68] W. Voigt. *Lehrbuch der Kristallphysik.* Teubner, Leipzig, 1928.

[69] A. Reuss. Berechung der fliessgrenze von mischkristallen. *Z. angew. Math. Mech.*, 9:55, 1929.

[70] R. Hill. The elastic behaviour of a crystalline aggregate. *Proc. Phys. Soc. A*, 65:349, 1951.

[71] C. M. S. Gannarelli, D. Alfè, and M. J. Gillan. The particle-in-cell model for ab iniio thermodynamics: implications for the elastic

anisotropy of the Earth's inner core. *Phys. Earth Planet. Inter*, 139:243, 2003.

[72] David J. Singh. *Planewaves, Pseudopotential and the LAPW Method.* Kluwer Academic, Boston, 1994.

[73] A. Laio, S. Bernard, G. L. Chiarotti, S. Scandolo, and E. Tosatti. Physics of iron at Earth's core conditions. *Science*, 287:1027, 2000.

[74] G. Kresse and J. Furthmüller. Efficient iterative schemes for *ab initio* total-energy calculations using a plane-wave basis set. *Phys. Rev. B*, 54:11169, 1996.

[75] G. Kresse and J. Furthmüller. Efficiency of *ab initio* total energy calculations for metals and semiconductors using a plane-wave basis set. *Comput. Mater. Sci.*, 6:15, 1996.

[76] G. Kresse and D. Joubert. From ultrasoft pseudopotentials to the projector augmented-wave method. *Phys. Rev. B*, 59:1758, 1999.

[77] C. S. Yoo, N. C. Holmes, M. Ross, D. J. Webb, and C. Pike. Shock temperatures and melting of iron at Earth core conditions. *Phys. Rev. Lett.*, 70:3931, 1993.

[78] D. Alfè, G. D. Price, and M. J. Gillan. Iron under Earth's core conditions: Liquid-state thermodynamics and high-pressure melting curve from ab initio calculations. *Phys. Rev. B*, 65:165118, 2002.

[79] Y. Ma, M. Somayazulu, G. Shen, H. K. Mao, J. Shu, and R. Hemley. In situ x-ray diffraction studies of iron to Earth-core conditions. *Phys. Earth Planet. Inter*, 143-144:455, 2004.

[80] C. M. S. Gannarelli, D. Alfè, and M. J. Gillan. The axial ratio of hcp iron at the conditions of the Earth's inner core. *Phys. Earth Planet. Inter*, 152:67, 2005.

[81] D. Alfé, 1998. Program available at http://chianti.geol.ucl.ac.uk/~dario.

[82] A. B. Belonoshko, R. Ahuja, and B. Johansson. Quasi-*ab initio* molecular dynamic study of Fe melting. *Phys. Rev. Lett.*, 84:3638, 2000.

[83] M.W. Finnis and J.E. Sinclair. A simple empirical N-body potential for transition metals. *Philisophical magazine*, A50:45, 1984.

[84] L. Stixrude and R. E. Cohen. High-pressure elasticity of iron and anisotropy of Earth's inner-core. *Science*, 267:1972, 1995.

[85] Lidunka Vočadlo, Dario Alfè, Michael J. Gillan, Ian G. Wood, John P. Brodholt, and G. David Price. Possible thermal and chemical stabilization of body-centered-cubic iron in the Earth's core. *Nature*, 424:536, 2003.